Characterization of Advanced Materials by Asynchronous Optical Sampling

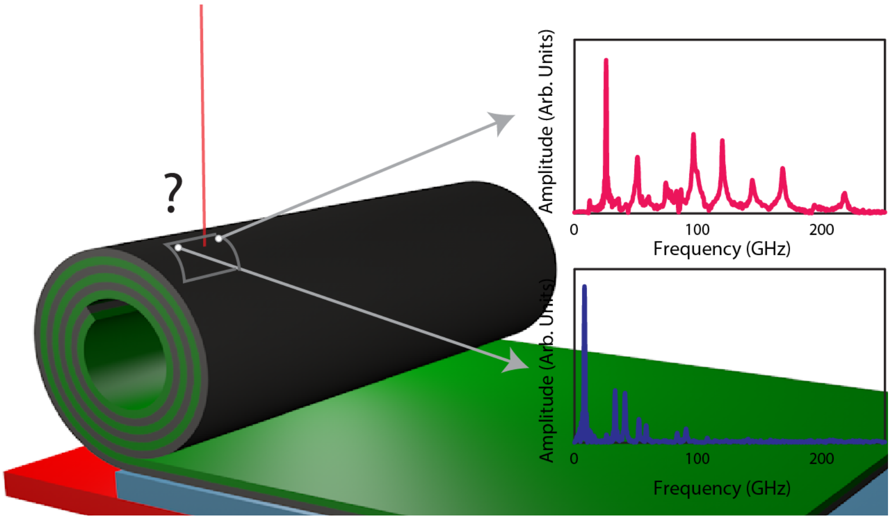

Delia Johanna Brick

University of Konstanz
Department of Physics

Characterization of Advanced Materials by Asynchronous Optical Sampling

DISSERTATION

submitted for the academic degree of
Doctor of Natural Sciences
(Doctor rerum naturalium)

presented by
Delia Johanna Brick

submitted to

Universität Konstanz

Universität Konstanz
Mathematisch-Naturwissenschaftliche Sektion
Fachbereich Physik

Konstanz, 2018

Date of the oral examination: January 19, 2018

1. Reviewer: Prof. Dr. Thomas Dekorsy
2. Reviewer: Prof. Dr. Eva Weig

Contents

CHAPTER 1

Introduction

Acoustic phenomena are well-known in the everyday life, as acoustic waves permanently encounter every human being in many different ways. Acoustics ranges from earthquakes to sound, for example of music or spoken words, to ultrasound, known from medical ultrasound imaging devices, and to heat. All these forms of acoustics have in common, that they can be described by mechanical vibrations at various frequencies. Phonons are the energy quanta of these lattice vibrations, analogous to photons, which are the energy quanta of electromagnetic waves. The properties of photons and electrons are indispensable in a high-tech society and are already exploited in many technological applications of the last two centuries. In contrast, the control over phonons is much less investigated or applied. In the course of the miniaturization of electric devices, phonons play a decisive role as they are able to influence the efficiency of nanoelectric and thermoelectric processes. This manipulation can be achieved by making use of elaborated design of bandstructure and transport properties of phonons at the nanoscale, in combination with the interactions with electrons and photons [Vol16]. Thus, the generation and control of phonons to test and investigate samples with confined geometries on the nanometer scale are particularly intriguing from a fundamental point of view, as well as with respect to a broad range of interdisciplinary applications in industry. An extensive variety of examples for the application of phonons can be found in nanoelectronic devices, such as frequency filters [Sav10] and thermoelectric devices [Bis12], or in the non-destructive investigation in several industrial applications, where the non-invasive characterization of e.g. thin films is of interest [Ros99]. Likewise, in biology the control of acoustic phonons is used, e.g. when studying cell dynamics and during medical diagnostics [Deh15, Ros08].

A possibility to non-destructively test the dynamics of acoustic phonons is offered by femtosecond pump-probe time-domain spectroscopy, also known as picosecond ultrasonics. Picosecond ultrasonics is an optoacoustic technique at the interface of optics and acoustics, which, in general, uses electromagnetic radiation for the excitation and detection of sound waves in a material [Gus93]. Thereby a femtosecond laser pulse excites coherent acoustic phonons inside the investigated sample, while a second time-delayed probe pulse detects the induced reflectivity changes. The probing part of the measurement can be seen as an ultrafast stroboscopic effect. The stroboscopic probe pulse splits the fast acoustic dynamics in single successive frames, which are recomposed later on. This measurement technique enables the characterization of the mechanical properties of the materials under study, such as an analysis of the appearing frequency modes. In this thesis, ultrafast time-resolved pump-probe spectroscopy measurements are conducted in various advanced material systems consisting of metals, semiconductors and polymers. The adhesion at interfaces, thin film thicknesses, and sound velocities in various material systems can be determined very precisely and non-destructively.

This thesis is structured as follows. Following the introduction, the basic concepts that are important for the understanding of coherent acoustic phonons in various material systems are established in Chapter 2. Elastic properties in solids are presented and the propagation of acoustic waves inside and at the interfaces of layered media is discussed. In addition, the eigenmode spectra of acoustic phonons are calculated and discussed for single layers, bilayers and superlattices. Finally, the main mechanisms of the generation and detection processes of coherent acoustic phonons in different materials and more complex material systems are introduced.

In Chapter 3, the basic principles of ultrafast time-resolved pump-probe spectroscopy are explained. Particularly, the method of asynchronous optical sampling is discussed, which is also utilized for the conducted measurements. Details about the experimental setup in order to accomplish the high-speed asynchronous optical sampling used in this thesis are given.

Subsequently, the discussion of the experimental results begins in Chapter 4. The first part deals with the investigation of planar multilayers and rolled-up multilayer tubes. Bilayers, inherently strained through a lattice mismatch, can be rolled up to form radial superlattices. Homogeneous and defect free tubes are highly desirable in applications, as an imperfect mechanical contact can lead to problems such as heat accumulation and thermal stress. Therefore, it is particularly interesting to characterize these multilayer tubes non-invasively. A detailed experimental and theoretical study of the coherent acoustic phonon modes in these rolled-up InGaAs/GaAs multilayer tubes is presented, with thicknesses of the layers in the nanometer and diameters in the micrometer range. The rolled-up superlattice tubes show intriguing differences compared to the planar structures that can be attributed to imperfect adhesion between individual tube windings. A transfer matrix method, including a massless spring model accounting for the imperfect adhesion between the layers, is utilized and yields good agreement with the experiment. This allows the spatially resolved characterization of individual tubes with micrometer spatial resolution, where areas with varying interface adhesion can be identified.

In the following Chapter 5, two different systems, one based on silicon dioxide on a silicon substrate and the other one based on silicon dioxide on the ferroelectric lithium niobate substrate, are investigated. The sound velocities of the respective layers and the film thickness of silicon dioxide, which pose crucial properties for the fabrication of surface-acoustic-wave filters for the communication technology, can be obtained simultaneously in a single measurement. Furthermore, information about the lithium niobate crystal orientation and the quality of the layer interface can be extracted due to the birefringence in the lithium niobate layer.

In Chapter 6, the polymer polymethyl methacrylate (PMMA) is investigated. A variety of polymer thicknesses is studied at room temperature. The extracted frequency modes can be assigned to the respective mode number and, hence, the thicknesses of the samples are extracted. Temperature measurements are performed, revealing a shift of the frequencies with a discontinuity, which is a direct indication of the undergoing glass transition in the sample. The temperature dependent change of the sound velocity can be disentangled from the contribution of the thickness change below the glass transition temperature. The glass transition temperature is obtained from the frequency spectra through the intersection of two linear fits on the frequency shift below and above the glass transition.

The thesis concludes with a summary and an outlook, given in Chapter 7. Further information on the sample fabrication and the material parameters used can be found in the Appendix.

CHAPTER 2

Theoretical Framework for Coherent Acoustic Phonons

Acoustic waves influence the dielectric function of matter. Hence, they can affect the interaction between matter and light. The optical generation and control of coherent acoustic phonons with ultrashort light pulses in various material systems has become an ever-growing field for both fundamental research and for technological applications [Vol16].

For the detailed understanding of these acousto-optic effects, which are important in the experiments presented in this thesis, the basic principles of ultrafast acoustics will be introduced. Starting with the elastic properties of solids in general, the propagation of acoustic phonons and the different boundary conditions in stratified media will be discussed. The acoustic eigenmodes in several multilayer systems will be derived. Light-matter interactions based on optical-to-mechanical energy transfer will be explained by the involved generation and detection mechanisms of coherent acoustic phonons. Frequencies of the resulting acoustic phonons are in a range of about 1 GHz up to some hundreds GHz. An explanation of the influence of the absorption profile and hence the generated stress will be given. The focus will be on the main mechanisms involved in the interaction of light with metals and semiconductors.

2.1. Elastic Properties – Stress and Strain

For the description of acoustic phonons it is important to first introduce stress and strain, on which the presented phenomena are based on. In solid matter, an ordered structure of atoms is based on attractive forces. These bonds can be described in a first approximation as elastic springs. When an atom in a solid is disturbed and displaced from its equilibrium position, it will result in a change in the position of the neighboring atoms. This process will launch an elastic wave that travels through the solid. Phonons are the quasi particles of these lattice vibrations. They are comparable to photons, which are the quanta of electromagnetic waves.

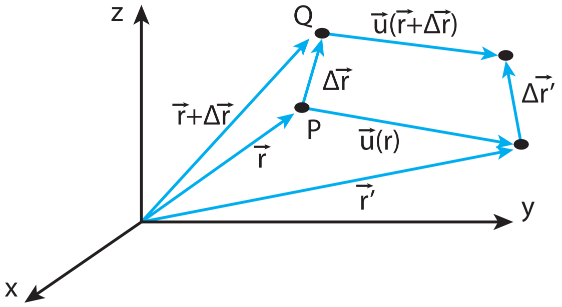

Figure 2.1.: Displacement of the two points P and Q under the influence of strain.

When a force is applied to a solid, where the stress inside a solid is defined as a force acting on a unit area per volume, it undergoes a deformation inducing strain [Aul73, Cle03]. Strain causes a shift of the position of an atom, described by the vector $\vec{u}$, depicted in Figure 2.1. The displacement vector $\vec{u}$ describes how the atom is displaced from its original position $\vec{r}$ to another position $\vec{r'}$ with

$$\vec{u}(\vec{r},t) = \vec{r'} - \vec{r} \tag{2.1}$$

The relative displacement of two positions, separated by Δr_j, can be written as

$$\Delta u_i = \sum_{j=1}^{3} \frac{\partial u_i}{\partial x_j} \Delta r_j \tag{2.2}$$

The derivations can be used to write the tensor $\mathrm{D} = \nabla \vec{u}$, which is the basic for the strain tensor. D can be divided into a symmetric and an asymmetric part to $\mathrm{D} = \eta + \Omega$. The symmetric part η is the linearized strain-displacement tensor for longitudinal and transverse deformations

$$\eta_{ij}(r,t) = \frac{1}{2}\left(\frac{\partial u_i}{\partial x_j} + \frac{\partial u_j}{\partial x_i}\right) \qquad \text{with} \quad i,j = x,y,z \tag{2.3}$$

and $\Omega = \frac{1}{2}\left(\frac{\partial u_i}{\partial x_j} - \frac{\partial u_j}{\partial x_i}\right)$ is the rotation tensor [Cle03]. In the presented work, only the linearized strain-displacement tensor is relevant for the theoretical description of the conducted experiments. The stress tensor σ_{ik} results from Hooke's law with $F_i = \frac{\partial}{\partial x_k}\sigma_{ik}$. Stress and strain tensor are connected through the elasticity tensor C_{iklm} with

$$\sigma_{ik} = C_{iklm}\eta_{lm} \tag{2.4}$$

This is the general form of Hooke's law, where the stress is the equivalent force and the strain the displacement, while the elastic constants are given by the elasticity tensor [Ros99].

2.2. Coherent Phonon Propagation in Layered Media

The previously derived description of displacement, stress and strain can now be used to find a formalism for the propagation of the deformation in media. The lateral size of the laser spot, which generates the acoustic phonons, is normally much larger than the depth ξ of the induced stress. Therefore, the coherent phonon dynamics induced by an ultrashort laser pulse can be simplified and considered to be in one dimension.

The dynamics of acoustic phonons can be described in the simplest picture by a one-dimensional linear chain of atoms. The equation of elastic motion based on the classical wave equation can describe the phonon dynamics. For an isotropic medium it is given by [Tho86]:

$$\rho \frac{\partial^2 u}{\partial t^2} = \frac{\partial \sigma}{\partial z} \tag{2.5}$$

where u is the particle displacement, ρ the mass density, and σ the photoinduced stress consisting of different contributions of the generation process, which will be described in Chapter 2.4. Here, the wave equation is calculated for the displacement u but it can be similarly written for the strain η [Tho86].
As only the z-direction is important, it is possible to simplify $u_z \rightarrow u$, $\eta_{ij} = \eta(z) = \frac{\partial u}{\partial z}$, $\sigma_{ij} = \sigma_{33} = \sigma$, and $C_{iklm} = C_{zzzz} = C$. Using Equation (2.4) and (2.5) the wave equation for a longitudinal wave can be written as

$$C \frac{\partial^2 u}{\partial z^2} = \rho \frac{\partial^2 u}{\partial t^2} \tag{2.6}$$

The equation can be solved for the assumption of a plane wave with the amplitude b, the frequency ω and the wave vector q

$$u = b e^{-i(qz - \omega t)} \tag{2.7}$$

When inserting this solution into the wave equation, it is possible to deduce a linear relationship between the angular frequency ω and the wave vector q

$$\omega = \sqrt{\frac{C}{\rho}} q = vq \tag{2.8}$$

hence, for the longitudinal sound velocity v_l it can be obtained:

$$v_l = \sqrt{\frac{C_{11}}{\rho}} \tag{2.9}$$

with the elastic constant C_{11}. The linear phonon dispersion relation $\omega(q)$, which is derived from the continuum model, only holds true for the long wavelength limit and hence small wave vectors $q \to 0$.

The dispersion relation obtained from an atomistic linear chain model not limited for the long wavelength range is given by

$$\omega(q) = 2\sqrt{\frac{f}{m}}\left|\sin\left(\frac{qa}{2}\right)\right| \tag{2.10}$$

with the mass m, the coupling constant f, and the distance between two atoms a. This equation only holds true for the acoustic branch of the phonon dispersion relation.

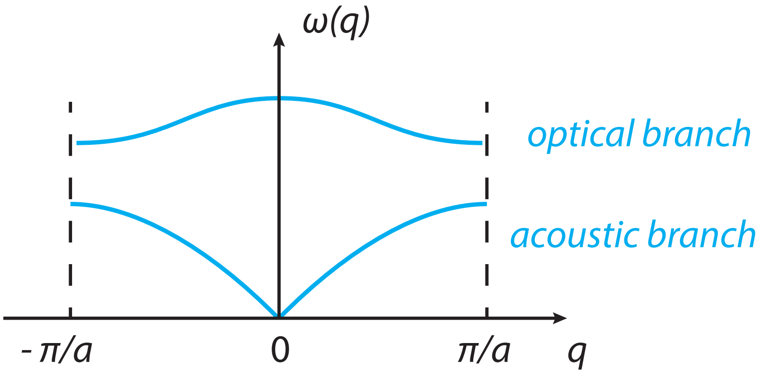

Figure 2.2.: Schematic of the phonon dispersion relation $\omega(q)$ of an atomistic linear chain with the acoustic and optical branches in bulk material. The Brillouin zone boundary is at $q = \pm\pi/a$.

Figure 2.2 shows the dispersion relation schematically. Two branches are visible, an acoustic and an optical branch. In this thesis only acoustic phonons will be important. Therefore, the focus will be on their properties. The dispersion relation is periodical for $2\pi/a$ and $q = \pm\pi/a$ as the boundary of the Brillouin zone, where a is the lattice constant of the solid.

The wave vectors of the photons are in the range of $10^5\,\mathrm{cm}^{-1}$. This is much smaller than the size of the Brillouin zone, which is in the range of $10^8\,\mathrm{cm}^{-1}$ [Ash05]. Therefore, one can only obtain information about the phonons close to $q = 0$. Experiments, which were performed in this thesis, are all within the linear regime of the dispersion relation.
For additional photoinduced stress σ from outside of the system an additional source term appears in the wave equation and it now can be written as [Rue15]

$$\frac{\partial^2 u}{\partial t^2} - v^2\frac{\partial^2 u}{\partial z^2} = \frac{1}{\rho}\frac{\partial\sigma(z,t)}{\partial z} \tag{2.11}$$

The photoinduced stress σ arises due to different processes, which will be discussed in Chapter 2.4.

2.2.1. Reflection and Transmission of Phonons at Interfaces

For the investigation of traveling acoustic phonons in multilayer systems, reflection and transmission at the interfaces need to be taken into account. The strain pulses will be partly reflected and transmitted. A detailed calculation can be found for example in [Aul73, Ros99]. Reflection and transmission can be computed by taking into account the boundary conditions for the stress and the displacement, which needs to be the same at the interface in both materials. A schematic of reflection and transmission in two layers is given in Figure 2.3. In the first medium, the resulting displacement is given by the incident and reflected part of the incident wave

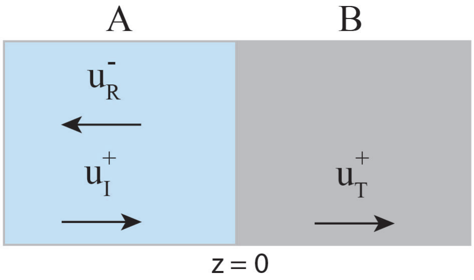

Figure 2.3.: Schematic of reflection and transmission at an interface of a system with the two layers A and B.

$$u_I^+(t) = a^+ e^{i(q_a z - \omega t)} \quad \text{and} \quad u_R^-(t) = a^- e^{-i(q_a z + \omega t)} \tag{2.12}$$

where a^+ and a^- are the amplitudes of incident and reflected wave, respectively, $q_a = \omega/v_l$ is the wavenumber and ω the frequency. In the second medium, the displacement is given only by the transmitted part

$$u_T^+(t) = b^+ e^{i(q_b z - \omega t)} \tag{2.13}$$

with b^+ the amplitude of the transmitted wave. The boundary conditions at a perfect interface for displacement and stress can be used, which are given at the interface at $z = 0$ by

$$u_I(z=0) + u_R(z=0) = u_T(z=0) \tag{2.14}$$

$$\sigma_I(z=0) + \sigma_R(z=0) = \sigma_T(z=0) \tag{2.15}$$

The reflection coefficient r is defined as $u_R^- = r u_I^+$, and similarly the transmission coefficient $u_T^+ = t u_I^+$. For the stress it is $\sigma = \rho v^2 \partial_z u = \rho v^2 i q_a u$. The boundary conditions result into

$$1 + r = t \tag{2.16}$$

$$Z_1 - Z_1 r = Z_2 t \tag{2.17}$$

The acoustic impedance is defined as $Z = \rho v_l$ with the longitudinal sound velocity v_l and the density ρ. The reflection coefficient r and the transmission coefficient t depend on the acoustic impedances of the top layer Z_1 and the adjacent layer Z_2 of the two involved materials and are defined as

$$r = \frac{Z_2 - Z_1}{Z_2 + Z_1} \tag{2.18}$$

$$t = \frac{2Z_2}{Z_2 + Z_1} \tag{2.19}$$

In the case of layers where the acoustic impedances are given by $Z_1 > Z_2$, a phase shift of the reflected wave of π occurs and hence a sign change of the acoustic strain pulse occurs.

2.3. Acoustic Eigenmode Calculations in Various Systems

In this section, calculations of acoustic eigenmodes in various layered systems of stratified media will be derived and discussed. The equations for the basic approach of the transfer matrix formalism will be derived for a two layer system and a massless spring model will be introduced. The eigenmodes for a single and a bilayer for different boundary conditions together with an analytical model for superlattices will be given. These theoretical considerations will enable the comparison of experimental and theoretical results.

2.3.1. Transfer Matrix Formalism

The reflection of light – and similar for phonons – from arbitrary multilayer systems is of interest for many applications as for optical coatings or simply for the acquisition of information about the mechanical properties of the structure itself. A general approach based on transfer matrices allows to calculate acoustic eigenmodes in multilayer systems as well as in superlattices with an arbitrary number of layers in the respective superlattice period.

The equations for the basis of this approach will be derived briefly for a two layer system, which is the basis for further variations of the structure. More details on the transfer matrix method can be found for example in [Tam88].

Two Layer System

A two layer system with the layers A and B is shown in Figure 2.4 (a).

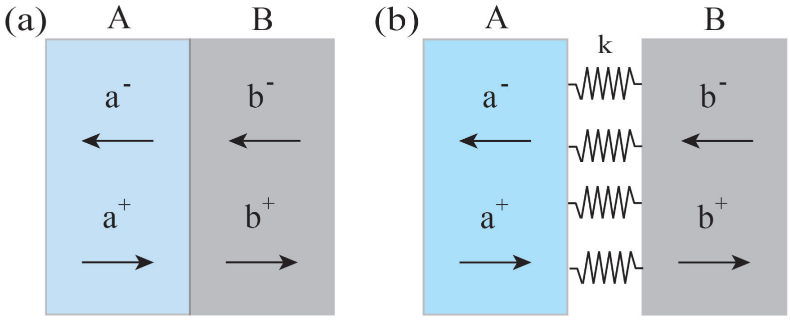

Figure 2.4.: Schematic of system with the two layers A and B (a) with a perfect interface and (b) with a massless spring with the spring constant k between the layers, which accounts for imperfect adhesion.

In this system, the following two boundary conditions have to be taken into account:

$$u_a(z_a = d_a) = u_b(z_b = 0) \tag{2.20}$$

$$\sigma_a(z_a = d_a) = \sigma_b(z_b = 0) \tag{2.21}$$

with the displacement u given by:

$$u_a(z_a) = a^+ e^{ik_a z_a} + a^- e^{-ik_a z_a} \tag{2.22}$$

and the stress σ, which can be written as:

$$\sigma_a(z_a) = iq_a C_a a^+ e^{iq_a z_a} - iq_a C_a a^- e^{-iq_a z_a} \tag{2.23}$$

a and b are the respective amplitudes of the waves. When using Equation (2.22) and (2.23) in Equation (2.20) and (2.21) the following is obtained:

$$a^+ e^{iq_a d_a} + a^- e^{-iq_a d_a} = b^+ + b^- \tag{2.24}$$

$$iq_a C_a a^+ e^{iq_a d_a} - iq_a C_a a^- e^{-iq_a d_a} = (b^+ - b^-) \tag{2.25}$$

Using the Equations (2.24) and (2.25), together with $C_j = \rho_j v_j^2$ and $(iq_a C_a)/(iq_b C_b) = \rho_a v_a / \rho_b v_b = Z_a/Z_b$, it can be written in the matrix form

$$\begin{pmatrix} e^{iq_a d_a} & e^{-iq_a d_a} \\ Z_{ab} e^{iq_a d_a} & -Z_{ab} e^{-iq_a d_a} \end{pmatrix} \begin{pmatrix} a^+ \\ a^- \end{pmatrix} = \begin{pmatrix} 1 & 1 \\ 1 & -1 \end{pmatrix} \begin{pmatrix} b^+ \\ b^- \end{pmatrix} \tag{2.26}$$

Equation (2.26) can be transformed into the transfer matrix T_{ab}:

$$\underbrace{\frac{1}{2} \begin{pmatrix} (1 + Z_{ab}) e^{iq_a d_a} & (1 - Z_{ab}) e^{-iq_a d_a} \\ (1 - Z_{ab}) e^{iq_a d_a} & (1 + Z_{ab}) e^{-iq_a d_a} \end{pmatrix}}_{T_{ab}} \begin{pmatrix} a^+ \\ a^- \end{pmatrix} = \begin{pmatrix} b^+ \\ b^- \end{pmatrix} \tag{2.27}$$

This is the fundamental concept of the transfer matrix method, which can now be applied to different systems.

2.3.2. Imperfect Adhesion – Massless Spring Model

In the case of the interface between two layers being not considered as perfectly adhered, the description of the behaviour at the interface becomes more complicated. The acoustic impedances are not the only factors anymore that account for reflection and transmission of an acoustic pulse. In the case of a non-perfect, elastic binding between two layers additionally the adhesion between the adjacent layers needs to be considered. In the transfer matrix method massless springs can be introduced between each layer to account for imperfect adhesion, as illustrated in Figure 2.4 (b). This is in contrast to the previous calculations, where perfect adhesion was always assumed.

The spring is characterized by the spring constant k. The stress has to be again the same at both sides of the interface, whereas the displacement is not rigid anymore but is now given by a linear relationship. Hence, the boundary conditions are

1) $\sigma_a = \sigma_b$
2) $\sigma_a = k(u_b - u_a)$

with the displacement u_a from (2.22) in 1)

$$C_a(a^+ e^{ik_a d_a} - a^- e^{-ik_a d_a}) = C_b(b^+ - b^-) \tag{2.28}$$

$$\Rightarrow Z_{ab}(a^+ e^{ik_a d_a} - a^- e^{-ik_a d_a}) = (b^+ - b^-) \tag{2.29}$$

This results into:

$$T_{ab} \begin{pmatrix} a^+ \\ a^- \end{pmatrix} = \begin{pmatrix} b^+ \\ b^- \end{pmatrix} \tag{2.30}$$

where $T_{ab} = \begin{pmatrix} 1 & -1/k \\ 0 & 1 \end{pmatrix}$ is the transfer matrix of a two-layer model for the interface with a discontinuous displacement u and a discontinuous strain σ due to the imperfect adhesion modeling with a spring.

2.3.3. Single Layer on a Half-Infinite Substrate

The acoustic eigenmodes of a single layer A on a half-infinite substrate B, as shown in Figure 2.5 (a), will be discussed in the following. Therefore, the wave equation needs to be solved for the occurring boundary conditions similar to the two-layer model, which was previously discussed. The paragraph is based on [Het13]. Here, two waves are counter propagating in the layer, while due to the half-infinite boundary condition only one wave is propagating in the substrate away from the surface. The three waves for the

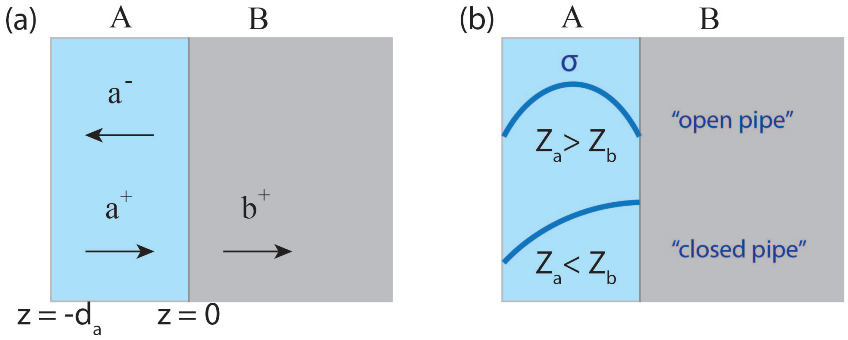

Figure 2.5.: Schematic of system with layer A on substrate B. (a) Displacement waves in layer A and substrate B. (b) The generated stress σ is shown in the layer A for the two cases of $Z_a > Z_b$ and $Z_a < Z_b$.

displacement are denoted by

$$u_a^+ = a^+ e^{ik_a z} \tag{2.31a}$$
$$u_a^- = a^- e^{-ik_a z} \tag{2.31b}$$
$$u_b^+ = b^+ e^{ik_b z} \tag{2.31c}$$

At the interface at $z = 0$ the boundary conditions apply:

$$\text{displacement:} \quad a^+ + a^- = b^+ \tag{2.32}$$
$$\text{stress:} \quad \rho_a v_a^2(-ik_a a^+ + ik_a a^-) = \rho_b v_b^2(-ik_b b^+) \tag{2.33}$$

The combination of displacement and stress and using $k_j = \frac{\omega}{v_j}$ and $Z_{ij} = \frac{\rho_i v_i}{\rho_j v_j}$ yields

$$-a^+ + a^- = -Z_{ba}(a^+ + a^-) \tag{2.34}$$

For the free surface the boundary conditions are the following

$$\text{stress:} \quad \sigma(z = -d_a) = 0 \tag{2.35}$$

Resulting into

$$a^+ e^{ik_a d_a} - a^- e^{-ik_a d_a} = 0 \tag{2.36}$$

Equations (2.33), (2.34) and (2.36) can be rewritten into the matrix form

$$\underbrace{\begin{pmatrix} 1 & 1 & -1 \\ 1 - Z_{ba} & -(1 + Z_{ba}) & 0 \\ e^{ik_a d_a} & e^{-ik_a d_a} & 0 \end{pmatrix}}_{M} \begin{pmatrix} a^+ \\ a^- \\ b^+ \end{pmatrix} = \begin{pmatrix} 0 \\ 0 \\ 0 \end{pmatrix} \tag{2.37}$$

The linear set of equations is solvable if det M = 0, which yields the solutions for the eigenmodes ω of the layer system. Together with the complex frequency $\omega = \omega' + i\omega''$ this yields

$$\begin{aligned}(1+Z_{ba})e^{-i\omega'' d_a/v_a}\left[\cos\left(\frac{d_a}{v_a}\omega'\right)+i\sin\left(\frac{d_a}{v_a}\omega'\right)\right]\\ -(1-Z_{ba})e^{i\omega'' d_a/v_a}\left[\cos\left(\frac{d_a}{v_a}\omega'\right)-i\sin\left(\frac{d_a}{v_a}\omega'\right)\right]=0\end{aligned} \tag{2.38}$$

This can be divided into real and imaginary part:

$$\text{real part:}\quad \underbrace{\cos\left(\frac{d}{v_a}\omega'\right)}_{A_1}\underbrace{\left[(1+Z_{ba})e^{-i\omega'' d_a/v_a}-(1-Z_{ba})e^{i\omega'' d_a/v_a}\right]}_{A_2}=0 \tag{2.39}$$

$$\text{imaginary part:}\quad \underbrace{\sin\left(\frac{d}{v_a}\omega'\right)}_{B_1}\underbrace{\left[(1+Z_{ba})e^{-i\omega'' d_a/v_a}+(1-Z_{ba})e^{i\omega'' d_a/v_a}\right]}_{B_2}=0 \tag{2.40}$$

Now, two cases have to be distinguished in dependence of the acoustic impedances to obtain the desired eigenfrequencies:
For $Z_a > Z_b$, i.e. $Z_{ba} < 1$, the same results will be obtained as for a free-standing membrane. $B_2 \neq 0$ and therefore B_1 needs to satisfy

$$\sin\left(\frac{d_a}{v_a}\omega'\right)=0 \tag{2.41}$$

Hence, the eigenfrequencies are given by

$$\omega' = n\frac{\pi v_a}{d_a} \quad \leftrightarrow \quad f = n\frac{v_a}{2d_a} \quad \text{for} \quad n = 1,2,3... \tag{2.42}$$

For the second case, when $Z_a < Z_b$, i.e. $Z_{ba} > 1$, the eigenmodes of the stress can be seen in Figure 2.5 (b). The eigenfrequencies are given by

$$\omega' = (2n-1)\frac{\pi v_a}{2d_a} \quad \leftrightarrow \quad f = (2n-1)\frac{v_a}{4d_a} \quad \text{for} \quad n = 1,2,3... \tag{2.43}$$

The results can also be explained by standing waves. $Z_a > Z_b$ modes are "open-pipe oscillations". The membrane is acoustically harder than the substrate, the stress at the interface is small and hence it can be treated as an open end.
$Z_a < Z_b$ can be seen similarly. These modes are called "closed-pipe oscillations". The layer is strongly acoustically decoupled from the substrate and only uneven modes can be detected [Aki11].

2.3.4. Bilayer Membrane

Freestanding

The eigenmodes of a bilayer are discussed based on [Gro17a]. At the free surface, perfect reflection is assumed again. The reflection at the thin film is given by the spectral transfer function

$$\Gamma = R_{ba} + \frac{T_{ba}T_{ab}}{\exp(-2iq_a d_a) - R_{ab}} \tag{2.44}$$

which indicates the ratio between the acoustic wave u_b^- incident on the interface and the reflected acoustic wave u_b^+ propagating away from the interface. The spectral transfer function and the boundary condition of a stress free surface at $z = d_b$ yield

$$u_b^+(z=0) = \Gamma u_b^- \qquad\qquad u_b^+(z=d_b) = e^{-2iq_b d_b} u_b^- \tag{2.45}$$

The combination of both results into the resonance condition of a two layer system

$$e^{-2iq_b d_b} = \Gamma = 1 - 2\left[1 + i\omega\frac{Z_b}{k_{ab}} + \frac{Z_b}{Z_a}\frac{1+e^{2iq_a d_a}}{1-e^{2iq_a d_a}}\right]^{-1} \tag{2.46}$$

Using the propagation time needed for the respective layers $t_1 = d_a/v_a$ and $t_2 = d_b/v_b$:

$$\sin(\omega(t_1+t_2)) = \left[\left(1-\frac{Z_b}{Z_a}\right) + \frac{\frac{\omega Z_b}{k_{12}}\tan(\omega t_2)}{\frac{\omega Z_b}{k_{12}}\tan(\omega t_2) - 1}\right]\sin(\omega t_b)\cos(\omega t_a) \tag{2.47}$$

The eigenmodes can be obtained by solving for the frequency ω. An analytical solution can be found when approximations are used. When assuming almost identical mechanical layers and thus impedances of the two layers $Z_a \approx Z_b$ and a perfect adhesion with the spring constant $k \to \infty$, the eigenmodes are given by

$$\sin(\omega(t_1+t_2)) = 0 \qquad\qquad \omega_n = \frac{n\pi}{(t_1+t_2)} = n\omega_0 \qquad\qquad (n = 1, 2, ...) \tag{2.48}$$

This result yields with the assumption of two similar layers the solution of a single layer with a combined thickness of both layers. For a small acoustic mismatch between the layers the solution will not change significantly. However, small perturbations will modulate the frequencies for strong adhesion sine-like. For the exact calculations see [Gro17a].

2.3.5. Acoustic Phonons in Superlattices: Analytical Model

So far, the discussion was limited to single layers and bilayers or bulk material. Another variation of the acoustic properties appears when investigating the acoustic behaviour in multilayer systems consisting of periodically repeating thin layers, so-called superlattices. The superlattices investigated in this thesis possess in one direction an artificial periodicity d_{SL} while the other directions are homogenous and infinite. Therefore, the following theoretical discussion is limited to one-dimensional superlattices.

Compared to bulk material, the electron and phonon dispersion and the lattice-dynamical properties in superlattices change considerably [Ryt56, Car89]. The dispersion relation of bulk material is given in Figure 2.2. Due to the repetitive structure, the dispersion relation in superlattices changes. The periodicity of the dispersion relation is not given anymore by the interatomic distance a but by the thickness d_{SL} of one period of the superlattice. The periodicity of the superlattice leads to a back-folding of the dispersion relation into a new and reduced mini-Brillouin zone with the boundaries given by $q = \pm\pi/d_{\mathrm{SL}}$.

In bulk material and for small wave vectors, the dispersion relation of acoustic phonons is linear with $\omega = vq$. This was derived in Equation (2.8) for the angular frequency ω, the sound velocity v and the wave vector q. In contrast, the dispersion relation of a superlattice can be approximated by the back-folding of the bulk dispersion by reciprocal superlattice vectors [Ryt56] into the new mini-Brillouin zone as indicated in Figure 2.6.

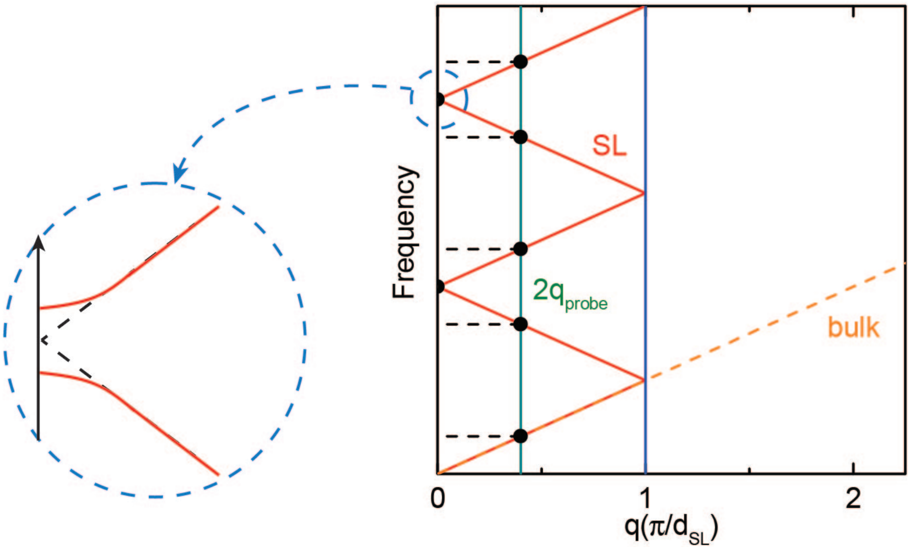

Figure 2.6.: Schematic of the acoustic phonon dispersion relation of a superlattice. Dotted orange line: Linear dispersion relation for bulk material. Red line: Back-folded dispersion relation of a superlattice. Blue line: Boundary of the reduced Brillouin zone. Green line: $2q_{Probe}$ laser line. The inset in the dotted circle on the left side shows the dispersion relation close to the Brillouin zone center with a band gap opening taking into account the acoustic modulation (solid red line) and without a band gap opening when the acoustic modulation is left out (dotted black line).

For an infinite superlattice, the transfer matrix formalism can also be applied to obtain the appearing eigenmodes of the acoustic phonons. The exact calculation can be found elsewhere [Tam88, Het13]. The acoustic dispersion relation of a superlattice with a two layer period of the layers A and B can be calculated by the elastic continuum model according to Rytov [Ryt56], which will be discussed in the following. The presented derivation follows the explanation given in [Car89]. This model applies both to crystalline and amorphous materials and the description is similar for longitudinal and transversal acoustic phonon modes.

For a one-dimensional propagation of an elastic wave in z-direction for an alternating structure of the two materials A and B the wave equation is given as in Equation (2.5) by:

$$C_{A,B}\frac{\partial^2 u_{A,B}}{\partial z^2} = \rho_{A,B}\frac{\partial^2 u_{A,B}}{\partial t^2}$$

where ρ is the density, C the elastic constant and u the atomic displacement in the respective material. When integrating the wave equation over an infinitesimal interval crossing any interface at z_i, here defined as $z_i = 0$, this will lead to the boundary condition:

$$C_A\frac{\partial u_A}{\partial z}\bigg|_{z_i=0} = C_B\frac{\partial u_B}{\partial z}\bigg|_{z_i=0} \tag{2.49}$$

which represents the continuity of the stress given at each interface. The continuity of the atomic displacements is:

$$u_A(z_i) = u_B(z_i) \tag{2.50}$$

These two boundary conditions are applied for the continuity at the interfaces and the periodicity of the structure needs to be taken into account. The displacement field in the two unit cells on either side of the origin is obtained. This results finally into the dispersion relation between the frequency ω and the wavevector q:

$$\cos(qd) = \underbrace{\cos\left(\omega\left[\frac{d_A}{v_A}+\frac{d_B}{v_B}\right]\right)}_{1.} - \underbrace{\frac{\epsilon^2}{2}\sin\left(\frac{\omega d_A}{v_A}\right)\sin\left(\frac{\omega d_B}{v_B}\right)}_{2.} \tag{2.51}$$

d_A , d_B are the respective layer thicknesses and v_A, v_B the respective sound velocities. This equation is similar to the Kronig-Penney dispersion relation for electrons in a square-wave potential [Kro30]. The first part of the equation represents the geometry of the structure. The second term of the dispersion relation including the correction term ϵ describes the acoustic modulation. It depends on the relative difference between the acoustic impedances given by $Z_{A/B} = \rho_{A/B}v_{A/B}$ and ϵ is given by

$$\epsilon = \frac{\rho_B v_B - \rho_A v_A}{\sqrt{\rho_B v_B \rho_A v_A}} \tag{2.52}$$

A difference in the acoustic impedances ΔZ of the two materials leads to an opening of the band gap at the center and edges of the mini-Brillouin zone, which increases with an increasing ΔZ. For superlattices with III-V compounds, which will be investigated in this thesis, ϵ is quite small ($\epsilon/2 \cong 10^{-2}$) and, hence, the second term can be neglected in a first approximation to

$$\cos(qd) = \cos\left(\omega\left[\frac{d_A}{v_A} + \frac{d_B}{v_B}\right]\right) \tag{2.53}$$

Here, only the geometrical contribution of the modulation is taken into account. It corresponds to the folding of an average elastic dispersion relation.
At the zone center and edges, double degenerate modes occur with the energies $\Omega_\nu = \frac{\nu\pi v}{d}$, where ν indicates the integer values at the zone center and edge.

Figure 2.6 depicts the folded acoustic phonon dispersion relation of a superlattice. The boundary of the reduced Brillouin zone is at $q = \pi/d_{SL}$ instead of $q = \pi/a$ as for the regular Brillouin zone. The back-folded dispersion relation is given by Equation (2.53). The green line represents the $2q_{probe}$-laser line.
The inset on the left side of Figure 2.6 shows the effect of the acoustic modulation ϵ on the dispersion relation close to the Brillouin zone center. When the acoustic modulation is taken into account a band gap opening appears at $q = 0$ (solid red line) at the center and at the edge of the Brillouin zone with $q = \pi/d_{SL}$. When the acoustic modulation is left out there is no band gap opening (dotted black line).

2.4. Optical Generation of Coherent Acoustic Phonons

In this thesis, the main part of the experiments was performed by the optical excitation of coherent acoustic phonons in different samples. A femtosecond light pulse is absorbed over the optical absorption length ζ and generates a strain pulse, which is propagating with the sound velocity v into the material in z direction. A time-delayed probe pulse detects the induced reflectivity change. When the generation process is on a much shorter time scale than the oscillation time, the phonons are generated impulsively. Hence, the phonons possess a well defined phase and thus are coherent. For all phenomena discussed in this thesis this assumption is valid.
The generation mechanisms for the investigated metals and semiconductors in this thesis are the thermoelastic effect, the deformation potential and the piezoelectric effect. Coherent stress is resulting from these effects, causing coherent acoustic phonons. In the following chapter, the essential opto-acoustic mechanisms for the generation of coherent acoustic phonons in solids by ultrashort laser pulses are described, based on [Rue15, Tho86]. Further possible mechanisms as electrostriction and magnetostriction do not contribute to the generation processes of the investigated materials and are thus neglected. However, details can be found in [Rue15, Kor08].

2.4.1. Thermoelasticity

Figure 2.7 (a) shows the electronic distribution in a metal: for an equilibrated material there exists an undisturbed thermal Fermi-Dirac distribution with the initial temperature $T_0 = T_e$ [Val07]. A light pulse ($\sim 100\,\mathrm{fs}$) excites the electrons above the Fermi level. The intraband absorption results in a non-equilibrium electron distribution. At this point, no internal temperature can be assigned to the electronic system. A thermal distribution – at a higher temperature than in the equilibrium state – is reached through electron-electron scattering on a time scale of a few 100 fs [Val07]. Within the next few picoseconds, electron-phonon coupling causes the excitation of incoherent phonons. This process causes a return to an equilibrium at a temperature T_L. The temperature T_L is only slightly higher compared to the initial temperature T_0. The phonons generated during the relaxation processes have no phase relation and contribute to the population of thermal phonons. The excited carriers contribute to the deformation potential mechanism, which is described in the next section.

The increase of the temperature of the lattice is due to the energy transfer from the initially excited electrons to the phonons sublattice. Figure 2.7 (b) shows an anharmonic interatomic Lennard-Jones potential. r_0 is the distance between the atoms of the lattice for $T = 0\mathrm{K}$. When there is an increase in vibrational energy, the mean lattice parameter $r(T)$ will increase. Thus, a volume change is induced due to thermal expansion, when

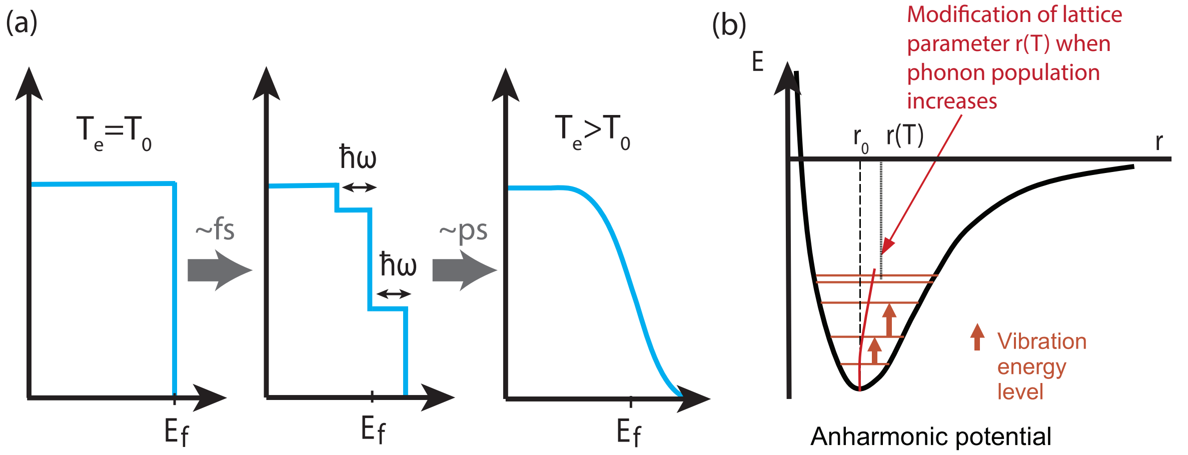

Figure 2.7.: (a) Intraband absorption in a metal causes a non-equilibrium electron distribution. This non-thermal distribution returns to an equilibrium with a higher temperature than in the equilibrium state. Image taken and adapted from [Val07] (b) Thermoelastic excitation causes a change of the mean interatomic distance $r(T)$ in an anharmonic potential. Strain is induced. Image taken and adapted from [Rue15].

lattice anharmonicity exists. The expansion is linked to the increase of the temperature ΔT, caused by incoherent phonons. Therefore, it is now in phase with the pump pulse. The change of the lattice parameter leads to a thermoelastic (TE) stress given (in one dimension) by [Tho86]

$$\sigma_{TE} = -3B\beta\Delta T_L \tag{2.54}$$

where β is the linear expansion coefficient and B the bulk modulus. This term can be used as source term in the wave equation (2.5), which was discussed for the propagation of acoustic phonons. The temperature change can be written as

$$\Delta T_L = \frac{(1-R)Q}{AC_v\alpha}\exp(-z/\alpha) \tag{2.55}$$

where R is the optical reflectivity, Q the energy per laser pulse, α the optical absorption coefficient, A the illuminated area, and C_v the specific heat per unit volume [Tas94]. The sharp features of the propagating strain are smoothed when the heat flow is included. The heat diffusion is given by the thermal diffusivity $D = K/C$, with K the thermal conductivity and C the specific heat capacity [Tho86].

The TE part in metals is larger than in semiconductors, as the absorption coefficient in metals is normally much larger. In metals, thermoelasticity is the main mechanism for acoustic phonon generation for phonon frequencies up to hundreds of GHz. Here, the acoustic spectrum is influenced by the strength of the electron-phonon coupling, which influences the distance over which the electrons transfer their energy into the sample.

For a strong coupling, the lattice is instantly heated and the deposition distance is about the same length as the optical skin depth of the excitation pulse $\zeta = \lambda_{\mathrm{pump}}/4\pi\kappa$, with κ the imaginary part of the refractive index. For example for Cr the optical skin depth is approximately 19 nm, for GaAs it is 760 nm.

The excitation process can be described in more detail by taking into account the hot-electron and heat diffusion, which are on the same timescales as the generation of the stress. To include the hot-electron diffusion, the two temperature model is often used. It will not be discussed here but details can be found in [Tas94, Rue15].

2.4.2. Deformation Potential

In semiconductors, the processes are similar to the ones previously described. The fast lattice heating correlates to intraband relaxation processes of electrons in the conduction band and holes in the valence band. This is shown in Figure 2.8 for the band structure of a semiconductor being excited by a laser pulse with an energy larger than the band gap energy. Due to the excess energy of the electrons after excitation, the electrons relax to the conduction band edge by electron-phonon coupling on a timescale of a few picoseconds [Dem11]. The increase of the lattice temperature results in thermoelastic stress.

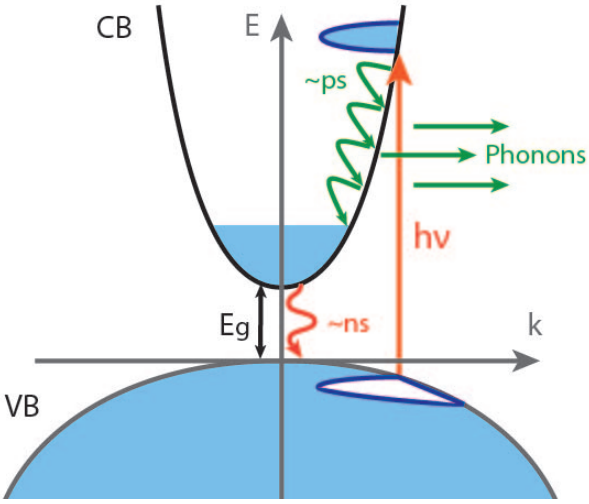

Figure 2.8.: Band structure of a semiconductor, where the electrons are excited above the band gap into the conduction band (CB) and leave holes in the valence band (VB). Intraband relaxation takes place on a picosecond time scale and incoherent phonons are generated. Electrons and holes recombine on a nanosecond time scale. The Figure was taken and adapted from [Rue15].

A change in the electronic distribution due to an external disturbance of a short light pulse will lead to a change of the electronic distribution. On a microscopic point of view this change leads to a modification of the interaction of electrons and holes. The lattice will be deformed. Hence, there will be strain in the material and acoustic phonons will be emitted. This connection between the change of the electronic distribution and strain in the solid is known as the deformation potential (DP) mechanism. This can be written as [Rue15]:

$$\frac{\delta V}{V} = \frac{\delta U}{d_{eh}} \tag{2.56}$$

with d_{eh}(eV) representing the deformation potential coefficient, U the electronic energy and $\delta V/V$ the strain introduced by the acoustic phonons with V as volume.
The deformation can be described by a modification of the band structure. Figure 2.9 (a) shows the scheme of the deformation potential according to a band structure description. The generated electron-hole pairs will change the band structure. The position of the atoms will change according to the new electronic distribution, which changes the interatomic distance. Hence, stress will be induced by the deformation.

The deformation potential can also be seen in the molecular approach as shown in Figure 2.9 (b). Excited electrons shift to empty electronic levels. The wave functions are overlapping with the wave function of neighboring atoms. This can lead to a binding or non-binding, which will either increase or decrease the distance between the atoms.

The photoinduced stress appearing in an isotropic medium is given by

$$\sigma_{DP} = \sum \delta n_e(k) \frac{\partial E_k}{\partial \eta} \tag{2.57}$$

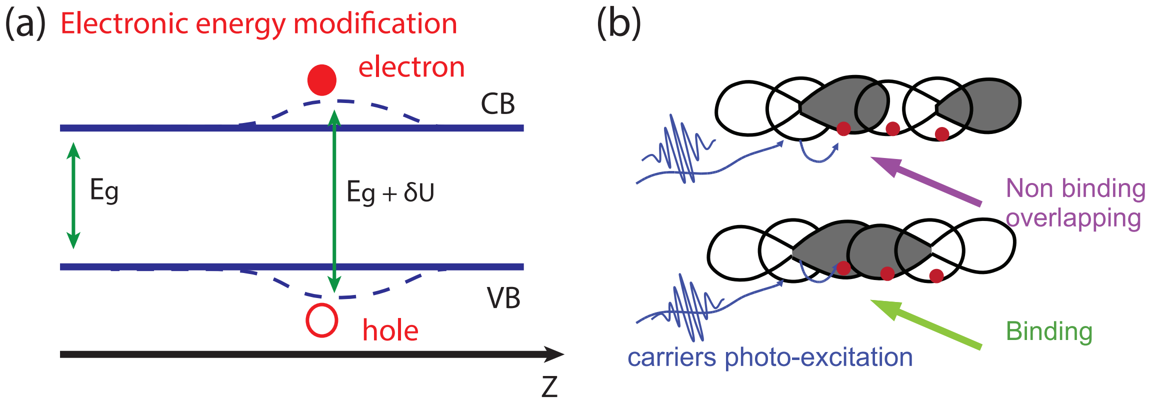

Figure 2.9.: (a) Schematic of DP in the band structure model for a semiconductor. When the electronic distribution is disturbed by an absorbed light pulse, the distances between the atoms are changed. Strain appears, which means phonons are generated. (b) Molecular view of DP. The grey and white coloured orbitals correspond to opposite signs of the wave functions. Binding or non-bondong will lead to a compression or expansion of the interatomic distance. This Figure was taken and adapted from [Rue15].

where $\delta n_e(k)$ is the change of the electronic concentration, k the wave vector, η the strain and $\frac{\partial E_k}{\partial \eta}$ the deformation potential parameter.

For semiconductors, the deformation potential is important for the generation of coherent acoustic phonons between 1 GHz and 1 THz as soon as electrons in the valence band are excited towards the conduction band with ultrashort laser pulses. Considering a solid, where the photon energy is equal to the direct band gap, it can be simplified for an isotropic solid to be [Rue15]:

$$\sigma_{DP} = -d_{eh} N_e \tag{2.58}$$

with the electron-hole-phonon deformation potential parameter d_{eh} and the carrier concentration N_e.

For GaAs – as this semiconductor will be investigated in Chapter 4 – the ratio of the part of the deformation potential and the part of thermoelasticity can be estimated. For the DP, the strain can be estimated to be [Wri01]

$$\sigma_{DP} = -d_{eh} N_e = -B N_e(x,t) \frac{\partial E_g}{\partial P} \tag{2.59}$$

with the bulk modulus B, the hydrostatic deformation potential $\frac{\partial E_g}{\partial P}$ and the number of excited electrons given by

$$N_e(x,t) = \frac{(1-R)Q\alpha}{A(E-E_g)} \exp(-\alpha x) \tag{2.60}$$

The Equations (2.59) and (2.60) together with (2.54) and (2.55) can be combined and, hence, the ratio of both strain generation processes results into

$$\frac{\sigma_{DP}}{\sigma_{TE}} = \frac{\partial E_g}{\partial P} \frac{C_v}{3\beta(E-E_g)} \approx 5.8 \tag{2.61}$$

The material parameters used are taken from [Wri01] with $\partial E_g / \partial P \approx 9 \cdot 10^{-11}$ eV/Pa. Hence, the contribution of DP is a factor of about 6 larger than the TE contribution. Therefore, TE can be neglected for the generation in GaAs.

In superlattices, the DP stress follows the given periodicity and absorption profile. This allows the control of the generated and detected acoustic phonon modes [Bar99, Rue15]. More details about acoustic phonons in superlattices are given in Section 2.3.5 and 2.5.4.

2.4.3. Piezoelectric Effect

In materials which are non-centro symmetric, a coupling between the strain and the macroscopic electric field inside the material appears [Rue15]. The coupling is due to the fact that a strain induces a polarization P. This mechanism is known as the piezoelectric effect. Similar, an applied electric field is able to induce strain. Hence, this leads to a deformation of the crystal known as the inverse piezoelectric effect.

The inverse piezoelectric tensor p_{ij} relates to an induced stress, when an electric field is applied. This can be written as:

$$\sigma_j = p_{ij} E_i \tag{2.62}$$

While for the deformation potential and the thermoelastic effect a change in the orientation of the material does not change the occuring stress, it indeed does change for the piezoelectric effect. Reversing the direction of the crystallographic orientation of the electric field will change the sign of the photoinduced stress.

For the generation of acoustic phonons via the piezoelectric effect a modulation of the internal electric field must be induced. The absorption of a laser pulse first excites free carriers, which then modulate the internal electric field. The electric field subsequently induces strain through the piezoelectric effect according to Equation (2.62).

2.5. Optical Detection of Reflectivity Changes

In the pump-probe setup used in this thesis, the absorption of a short laser pulse at the sample surface leads to traveling acoustic phonons. The resulting change in the sample reflectivity ΔR can be detected with a time-delayed probe pulse. By scanning the time delay between pump and probe pulse, the temporal evolution of ΔR can be resolved. Similarly, changes in the transmission can be detected as well by choosing a matching experimental setup. Here, only measurements in reflection geometry are presented. The following discussion about the detection mechanisms is based on [Tho86, Rue15].

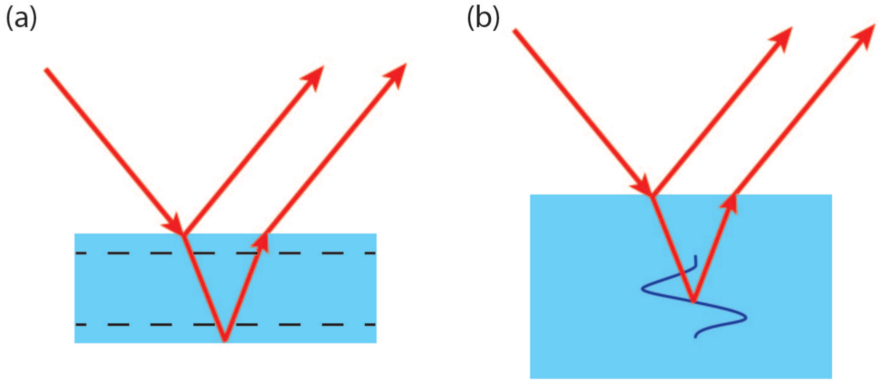

Figure 2.10.: Mechanisms for the optical detection of a reflectivity change. A probe pulse is incident on the perturbed sample. (a) *Interferometric detection* by interference of reflections at the top and bottom surface of a thin layer, which is extended and compressed. (b) *Photoelastic detection* by interference of a part of the light pulse reflected at the surface with the other part reflected at the propagating strain pulse.

The initially generated strain can change the optical reflectivity in different ways. It can be divided into interferometric effects, the photoelastic effect – both shown in Figure 2.10 – and surface tilting. More information on surface tilting can be found elsewhere [Gus95]. The focus will be on the photoelastic detection, as this is the most important detection mechanism in the scope of the experiments conducted in this thesis. The schematic shown in Figure 2.10 (b) illustrates the case of a transparent layer. For opaque samples, the detection would be only close to the surface on a scale of a few nanometers.

2.5.1. Photoelastic Detection

The changes in the real part $\Delta n(z,t)$ and the imaginary part $\Delta\kappa(z,t)$ of the index of refraction due to strain are given by

$$\Delta n(z,t) = \frac{\partial n}{\partial \eta_{33}} \eta_{33}(z,t), \tag{2.63}$$

$$\Delta \kappa(z,t) = \frac{\partial \kappa}{\partial \eta_{33}} \eta_{33}(z,t). \tag{2.64}$$

with the elastic strain tensor η_{33}. In first order approximation of the strain, the reflectivity change yields:

$$\Delta R(t) = \int_0^\infty f(z) \eta_{33}(z,t) dz \tag{2.65}$$

with the so-called sensitivity function $f(z)$:

$$f(z) = f_0 \left[\frac{\partial n}{\partial \eta_{33}} \sin\left(\frac{4\pi n z}{\lambda} - \phi\right) + \frac{\partial \kappa}{\partial \eta_{33}} \cos\left(\frac{4\pi n z}{\lambda} - \phi\right) \right] e^{-z/\zeta} \tag{2.66}$$

where f_0 is defined as

$$f_0 = 8 \frac{\omega \left[n^2(n^2+\kappa^2-1)^2 + \kappa^2(n^2+\kappa^2+1)^2 \right]^{1/2}}{c \left[(n+1)^2 + \kappa^2 \right]^2} \tag{2.67}$$

with the phonon frequency ω and the phase ϕ is given by:

$$\tan\phi = \frac{\kappa(n^2+\kappa^2+1)}{n(n^2+\kappa^2-1)} \tag{2.68}$$

ζ is the optical penetration depth. The sensitivity function indicates how the strain contributes to the change in the reflectivity at different distances from the surface of the sample. Generally $f(z)$ is an oscillation that damps exponentially with ζ and with a nonzero phase at the surface with $z = 0$. The penetration depth ζ is given by $\zeta = \frac{\lambda}{4\pi\kappa} = \alpha^{-1}$ with the laser wavelength λ and the imaginary part of the refractive index κ. The influence of the absorption length will be discussed in the following.

Time-resolved Brillouin Scattering

The sensitivity function exhibits an oscillation, which describes the time-resolved Brillouin scattering. The probe light is reflected at the traveling strain pulse inside the material and interferes with the light reflected at the surface. During this process, the light intensity is modulated with the frequency:

$$f = \frac{2nv_l}{\lambda_{probe}} \tag{2.69}$$

with λ the wavelength of the probe pulse and n the real part of the refractive index. This equation can also be derived when considering the momentum conservation of $\Delta k_L = 2k_L = q$ when the probe pulse with the wave vector k_L is reflected on a phonon with the wave vector q [Hud09]. The change of the wave vector of the probe light is then $2k_L$. As can be seen immediately from the equation, the measured Brillouin frequency can be used to determine the speed of sound or the refractive index of a material when the respective other parameter is known.

In dependence of the investigated material and the wavelength of the excitation pulse, the incident light is absorbed over a certain depth ζ, causing a varying stress profile. Figure 2.11 shows different generated stress profiles in dependence of the absorption length together with the resulting measured reflectivity change.
Metal layers for example have penetration depths of a few tens of nanometers, meaning that they can only be measured in an area close to the surface. The absorption profile is exponentially shaped close to the surface of the sample. Figure 2.11 (a) shows the absorption close to the surface with the corresponding reflectivity changes in Figure 2.11 (c). For strong absorbing materials, a short echo pulse is generated. In contrast, Figure 2.11 (b) shows a homogeneous absorption over the whole layer – as it is the case for many semiconductors where the penetration depth is relatively large – and phonons can be detected in the whole sample [Wu07, Hud09] due to the homogeneous and low absorption. The corresponding reflectivity change is shown in Figure 2.11 (d). A short pulse is no longer visible but Brillouin oscillations can be seen.

The origin of Brillouin oscillations and an acoustic echo generated in a strongly absorbing metal is effectively the same [Dev15]. However, the oscillation of the Brillouin oscillation is more damped, the more the material changes from transparent to opaque. This finally results in a short echo pulse. Between Figure 2.11 (c) and (d) the transition of the reflectivity response is depicted in green.

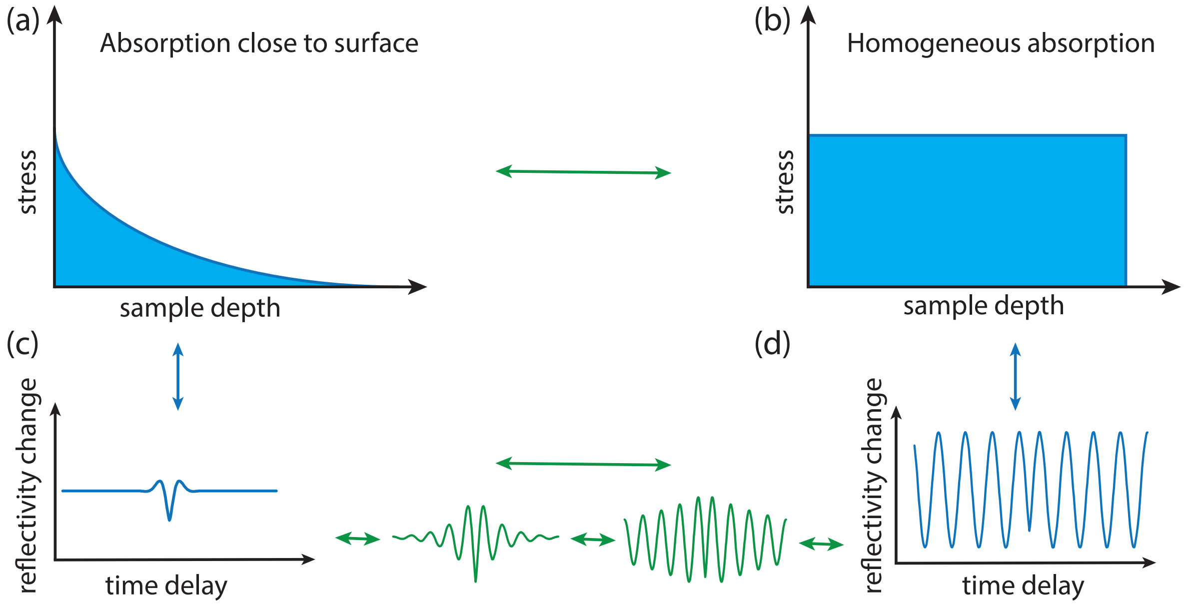

Figure 2.11.: Top part: stress profile in the moment of absorption in a sample in the case of (a) a material with a short penetration depth – for example a metal layer – and (b) a long penetration depth and hence a homogeneous absorption over the sample – for example in a semiconductor. Bottom part: the corresponding reflectivity change. The transition of the reflectivity change between a pulse (c) and Brillouin oscillations (d) is indicated in green. As the physical origin of Brillouin oscillations and a pulse echo is the same, the signals can be converted from one into the other by changing the material from opaque to transparent. The figure is adapted from [Dev15].

2.5.2. Interferometric Detection

Interferometric, also called Fabry-Perot like, detection results from a light pulse traveling in a thin film, where the light interacts at the two parallel surfaces, which form a cavity [Ris16, Gro17a]. A part of the light pulse will be reflected, while a part will be transmitted and travels back to the surface, where it interferes with the directly reflected part. As a part of the light pulse will undergo several round-trips through the two interfaces, the thin film can be seen as a Fabry-Perot cavity. The displacement of the two surfaces – due to thermal expansion and strain – causes an interferometric change in the reflectivity. Figure 2.10 (a) illustrates the principle of interferometric detection. The optical reflectivity for the refractive index n_2 of the material and n of air is given by

$$R = \left| \frac{n - n_2}{n + n_2} \right|^2 \tag{2.70}$$

For a Fabry-Perot cavity the intensity modulation is given for an incident light pulse with the intensity I_0 by

$$I_r = I_0 \frac{\mathcal{F} \sin^2(2\pi n_2 d/\lambda)}{1 + \mathcal{F} \sin^2(2\pi n_2 d/\lambda)} \tag{2.71}$$

with the layer thickness d and the finesse $\mathcal{F} = 4R/(1-R)^2$ of the cavity. In Chapter 6 the interferometric detection is the main detection mechanism for the investigated polymer. Instead of the simplest case of a Fabry-Perot cavity, the reflectivity is in the investigated case not the same at both interfaces.

2.5.3. Detection in Multilayer Systems

Matsuda et al. [Mat02] presented a thorough discussion of the perturbation of the reflectivity caused by strain in arbitrary multilayer systems.

This discussion is similar to the propagation of electromagnetic waves, for which this formalism was introduced originally. The relative change in the complex reflectance is given by [Mat02]:

$$\begin{aligned}\frac{\delta r}{r} = \frac{ik^2}{2k_0 a_0 b_0} \Bigg\{ & \int_z^0 P_{12}^{(0)} \eta(z') \left[a_0 \exp(ik_0 z') + b_0 \exp(-ik_0 z')\right]^2 dz' \\ & + \sum_{n=1}^{N+1} \int_0^{d_n} P_{12}^{(n)} \eta(z' + z_{n-1}) \left[a_n \exp(ik_n z') + b_n \exp(-ik_n z')\right]^2 dz' \\ & + \sum_{n=1}^{N+1} (a_n + b_n)^2 \left[\epsilon^{(n-1)} - \epsilon^n\right] u(z_{n-1}) \Bigg\}\end{aligned} \tag{2.72}$$

Here, r is the complex reflectance for the unperturbed multilayer. k and k_n are the wave vectors in vacuum and in the respective layer, respectively. a_n and b_n are the respective amplitudes of the optical counter-propagating waves and $\epsilon^{(n)}$ the dielectric constants in the respective layers. $P_{12}^{(n)}$ is the photoelastic constant of the nth layer.

The first term in Equation (2.72) stands for the modulation of the medium in front of the multilayer stack. In the case of air, this term can be neglected as the strain pulse cannot propagate there. The second term describes the bulk photoelastic effect and the last term the interface motion. In the case of a single layer and not a layer stack, Equation (2.72) reduces to the formalism derived for photoelastic detection in Section 2.5.1.

2.5.4. Detection in Superlattices

Light scattering spectroscopy of superlattices has strict selection rules due to the conservation of the wave vector q. Only eigenmodes can be detected which have a symmetry to couple to the light of the probe pulse and at the same time to conserve the momentum. To conserve q, the phonons must have a wavevector amplitude close to zero, which means near the Brillouin zone center. This is due to the fact that the magnitudes of the wavevectors of incident and scattered radiation are very small compared to the one of a general vector in the Brillouin zone. Therefore, the generation of the acoustic phonons is restricted to the zone center at $q = 0$. Modes can be detected most efficiently at the effective wave vector of

$$q = 2q_{Probe} = \frac{2\pi n}{\lambda}, \tag{2.73}$$

with q_{Probe} being the wave vector of the probe pulse and n the refractive index averaged over one superlattice period [Tam88, Bar99, Bru12]. The selection rules in Raman spectroscopy are similar [Car89].

Finite-size Effects

It is important to note, that the selection rules for generation and detection only apply to ideal superlattices with an infinite number of layer repetitions. Effectively, there are no ideal superlattices but only finite-size samples with a finite number of periods. The finite-size together with the spectral width of the laser pulses cause a broadening of the respective generation and detection sensitivity and create an overlap of generation and detection bandwidth. This “violation” of the selection rules due to imperfectness of both the signal and the sample is needed to enable the detection of acoustic dynamics in superlattices with pump-probe measurements. Modes can be detected at the zone center with $q = 0$ and at the intersections of the dispersion relation with $2q_{Probe}$.

In Figure 2.6 the modes that can be detected are indicated by black circles. The typical phonon spectrum observed in experiments thus consists of triplets in the spectral domain, which corresponds to the first folded phonon modes at the Brillouin zone center [PW12]. In the case of a perfectly infinite superlattice the detection would not be possible.

There are different possibilities to avoid the limitations due to the restricted bandwidth overlap of the generation and detection processes. One option are phonon cavities, which are similar to optical microcavities. Here, phonons are confined in layered structures surrounding a spacer material, when the spacer thickness is an integer multiple of the half acoustic wavelength $\lambda/2$ at the center of one of the SL minigaps [Tri02a].

CHAPTER 3

Ultrafast Pump-Probe Spectroscopy

Many relevant physical processes are occuring on a timescale of picoseconds to femtoseconds. This is too fast to be observed in real-time and with purely electronic measurement techniques being limited to a temporal resolution of up to 10 ps [Füs12]. Examples of these fast processes include picosecond ultrasound [Tho86], spin-dynamics [Bea96], long-living coherent lattice or charge carrier dynamics in solid-state [Dem99], high-resolution terahertz spectroscopy [Kla09], or the characterization of high-speed optoelectronic devices [Bar06] as well as fundamental processes in biology [Ros08, Deh15].

For the investigation of ultrafast processes, optical methods must be used. The development of mode-locked femtosecond lasers in the end of the 1980s facilitated the access to these ultrashort time scales by using them in pump-probe spectroscopy as “high-speed cameras” [Pra12], assembling the whole process by single “snap-shots”.
Since then, there has been a lot of investigation on the light-matter interaction in a variety of materials and material systems [Tho84, Vol16, Rue15]. The principle of pump-probe spectroscopy is to excite the sample with an optical pulse into a defined non-equilibrium state and to use a second time-delayed pulse to measure the dynamics of the sample as a function of the time delay between the two pulses [Geb10b]. The temporal length of the laser pulses restricts the temporal resolution.

In the following, the fundamental principle of pump-probe spectroscopy will first be explained in general. Then, specifically the principle of high-speed asynchronous optical sampling is introduced, as the main experimental part of this thesis was performed with this method. Thereafter, details about the experimental setup will be given and an exemplary measurement will be shown and briefly explained. Details on the generation and detection of femtosecond laser pulses and other information about fundamentals of photonics will not be given here, but can be found in any introduction to photonics text book as e.g. in [Sal07, Pra12].

3.1. General Principle

Ultrafast pump-probe spectroscopy is based on a train of pump and probe laser pulses usually generated by a single mode-locked laser [Tho84, Tho86, Pra12]. The pump pulse excites dynamics in the sample, while the probe pulse is temporally delayed by being guided a variable distance before it reaches the same spot on the sample. As the pump pulse induces a change in the optical properties of the sample, the probe pulse detects the reflectivity or transmission changes. The back reflected (in some cases also the transmitted) part of the probe pulse is then detected and analyzed. The dynamics excited in the sample can be resolved temporally by the measurement of the reflected probe pulse for different time delays.
Details on the mechanisms occuring inside the sample during the pump-probe spectroscopy measurement after being excited by a laser pulse can be found in Chapter 2.

The simplest way to implement a pump-probe spectroscopy setup is to use a pulsed laser and a beam splitter. In Figure 3.1, the general pump-probe principle is shown schematically.

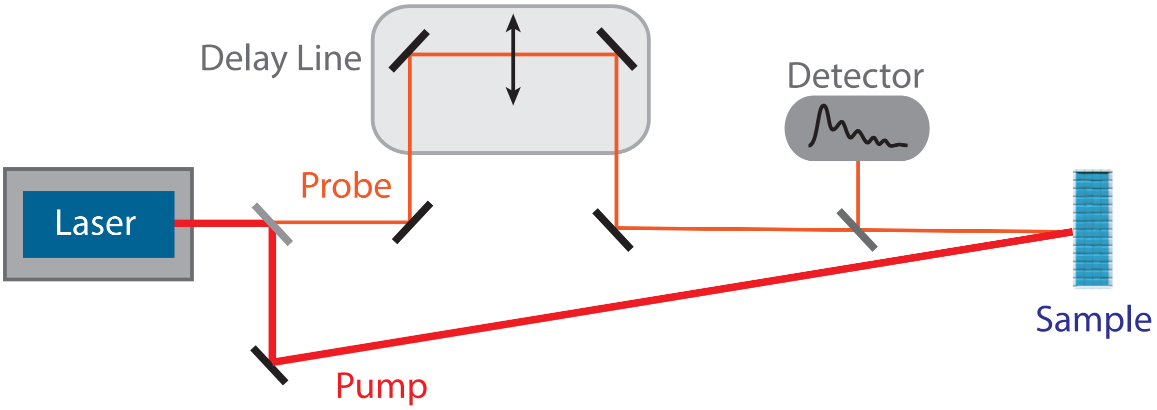

Figure 3.1.: General principle of pump-probe spectroscopy: A laser pulse is split into two parts, a stronger pump and a weaker probe pulse. The pump pulse – here presented as thick red line – excites the sample. The probe pulse – here presented as thin orange line – is delayed compared to the pump pulse through a variable delay line and detects the reflectivity change of the sample at the same spot excited by the pump pulse. The probe pulse is reflected back and is measured at the detector.

At the beam splitter, the laser pulse is split into a stronger pump pulse and a weaker probe pulse. While the pump pulse excites the sample, the probe pulse is delayed compared to the pump pulse through a delay line, e.g. a mechanical delay stage. The delay line changes the path the probe pulse is taking until it reaches the sample. By varying the delay of the probe pulse, the signal, which is induced by the pump pulse in the sample, can be scanned over several measurements. The response of the sample is hence given dependent on the change of the delay line, which represents the time delay. As an example, a change of the optical path of 37.5 cm with the light velocity of $3 \cdot 10^8\,\mathrm{m\,s^{-1}}$ will cause a time delay of 1.25 ns.

There are several complications arising from this method, especially the fact that the mechanical delay line causes artifacts such as divergence of the laser beam that cause spot size variations, laser beam pointing instabilities, sensitivity to external noise and long measurement times [Bar07, Hud09].

One approach to circumvent these drawbacks is the so-called asynchronous optical sampling, a modified variation of the basic pump-probe setup.

3.2. Asynchronous Optical Sampling

Asynchronous optical sampling (ASOPS) was first introduced by Elzinga et al. in 1987, with a repetition rate of the lasers employed of 80 MHz [Elz87]. Bartels et al. applied this method to high-repetition rate lasers with a repetition rate of approximately 1 GHz [Bar06].

The main difference compared to conventional pump-probe systems is that ASOPS enables to scan over a nanosecond time delay without any mechanical delay line. An alternative to the mechanical delay line is realized through two mode-locked lasers – as opposed to one – with a small offset in the repetition rates Δf. The offset introduces the "asynchronous" part of this method.

One laser generates the pump pulses with the frequency f_{pump}, the other laser the probe pulses with $f_{probe} = f_{pump} - \Delta f$. At some point, both laser pulses arrive at the trigger diode at the same time. This event is used as the beginning of the measurement and the time difference of the two pulses is $\Delta t = 0$. Due to the offset the time delay Δt is ramped between 0 and the inverse repetition rate of the pump laser $1/f_{pump}$.

The time difference between the two pulses is increased linearly from each pulse pair to the next with Δt:

$$\Delta t = \frac{1}{f_{probe}} - \frac{1}{f_{pump}} = \frac{\Delta f}{(f_{probe} \cdot f_{pump})} \tag{3.1}$$

After a measurement time of $T = 1/\Delta f$, pump and probe pulses arrive again at the same time at the detector and a new measurement starts. In the used system, the scan of one measurement needs a time of $T = 1/\Delta f = 1/5\,\mathrm{kHz} = 200\,\mu\mathrm{s}$.

Figure 3.2 depicts the general principle of ASOPS. The first row shows the time domain dynamics of the reflectivity changes $\Delta R/R$, which are induced by the pump pulses shown in the row below. R is the unperturbed static reflectivity of the sample. The third row depicts the probe pulses with a different repetition rate, which detect and scan the reflectivity change in the sample. The bottom row shows the assembled signal. The final result is obtained by an average over several thousands of measurements to achieve a high signal-to-noise ratio. Two time scales are shown in the Figure. The first line shows the actual time of the sample dynamics with a maximum of the measurement window given by the inverse of the repetition rate (for 800 GHz a measurement window of 1.25 ns is achieved). The last row shows a different time scale due to the detection process. The measurement window of 1.25 ns is "stretched" to the inverse of the measurement time with $T = 1/\Delta f = 1/5\,\text{kHz} = 200\,\mu\text{s}$ as indicated above.

Factors that mainly limit the temporal resolution of an ASOPS measurement are the pulse width, the repetition rate, the stability of the repetition rate and the bandwidth of the detection [Bar07, Hud09].
Another advantage of ASOPS systems is the possibility to shift the wavelength of both laser pulses individually.

In this thesis, high-speed ASOPS is used for the investigation of the dynamics in the sample structures.

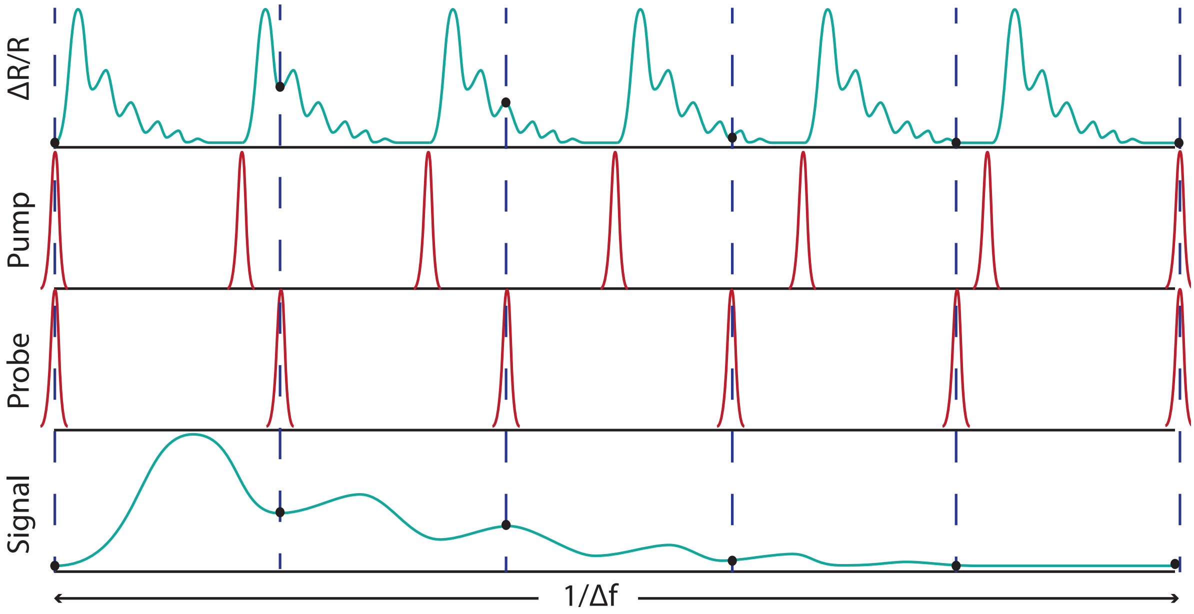

Figure 3.2.: Principle of asynchronous optical sampling measurement: The first row depicts the time-domain dynamics of the reflectivity change $\Delta R/R$, which are induced by the pump pulses shown in the row below. The third row shows the probe pulses with a smaller repetition rate compared to the pump pulse, which detect and scan the temporal behaviour of the reflectivity changes in the sample. The bottom row exhibits the assembled signal.

3.3. Experimental Setup

In Chapter 3.1 and Chapter 3.2 the principles of pump-probe spectroscopy in general and in particular the basics of ASOPS were discussed. The exact experimental high-speed ASOPS setup, which was used for the measurements in this thesis, will be described briefly in the following. A. Bartels introduced the setup in 2006 [Bar06]. A more detailed description of the entire setup can also be found in [Geb10a, Hud09, Hei17].

Optical excitation and detection of coherent acoustic phonons are realized by means of high-speed asynchronous optical sampling. The setup consists of two mode-locked Ti:sapphire lasers (GIGAJET TWIN SERIES, LASER QUANTUM, GERMANY), which are assembled in one housing with a mirrored configuration of the resonators. Ti:sapphire lasers are the most common ultrafast lasers in the wavelength range close to 800 nm [Rau08, Spe91]. They are pumped by a diode-pumped solid-state 10 W cw-laser (VERDI, COHERENT) at a wavelength of 532 nm, whose output power is split into two identical parts. Figure 3.3 displays a schematic of the experimental setup.
The two Ti:sapphire oscillators consist each of 6 mirrors, a prism and a Ti:sapphire crystal, forming a ring cavity. The prisms can be used to change the wavelength of the laser beams as light of different wavelengths is refracted differently. By changing the angle of the mirror, the wavelength that will be intensified can be chosen. The wavelengths can be set between 750 nm and 850 nm. Pump and probe wavelengths are centered in most cases at 790 nm and 820 nm, respectively, which corresponds to photon energies of 1.57 eV and 1.51 eV.
Each of the two lasers has a repetition rate of approximately $f_{rep} = 800\,\text{MHz}$, which gives access to a scan window of $\tau = 1/f_{rep} = 1.25\,\text{ns}$.
The repetition rate offset is stabilized using active feedback. Therefore, a part of each of the two laser beams is separated and redirected in two photo diodes, which transmit the repetition rate to the stabilization unit. For the stabilization of the repetition rate, one laser is used as master – here the probe pulse is used – with the repetition rate f. The second laser is linked as slave – here the pump pulse – with $f + \Delta f$ and the stabilized offset in the laser repetition rates set to $\Delta f = 5$ kHz. This stabilization is realized with a phase-locked loop. Details on the stabilization can be found in [Hud09, Geb10b].
The repetition rates can be measured and generate an error signal that represents the time dependent deviation of the actual offset from the desired one. The error signal is split into a low frequency and high frequency part. These error signals regulate the offset by using two piezoelectric actuators inside the cavity of the pump laser with resonator mirrors glued onto them.

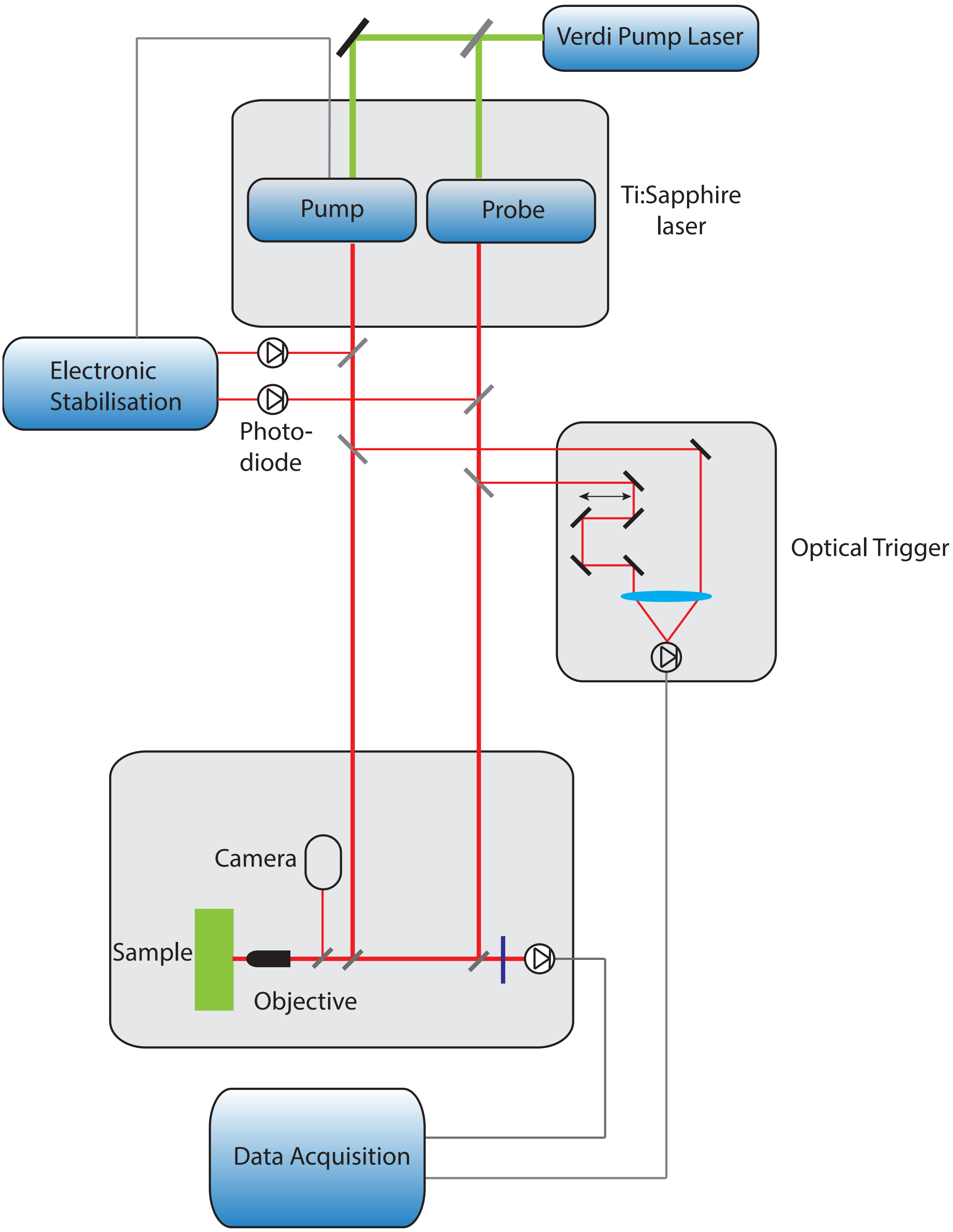

Figure 3.3.: Schematic of the experimental setup. The main parts of laser generation, electronic stabilization, optical trigger, sample and detector for the data acquisition are shown. Details are given in the main text.

Without the phase-locked loop, the repetition rate would change irregularily due to thermal fluctuations and mechanical vibrations.
The repetition rate offset corresponds to a measurement time of 200 µs for a single time trace and enables a signal-to-noise ratio of about 10^7 in approximately 250 s data aquisition time. The temporal resolution, which is dependent on the repetition rate of the two lasers and their offset together with the bandwith BW, can be estimated with $\Delta f/(BW(f+\Delta f)) = 50\,\mathrm{fs}$ [Geb10b]. The actual time resolution is worse than this value, however, as the optical pulse width and the timing jitter limits the resolution too. Through the dispersive optical elements that the pulse needs to propagate through, the group velocity dispersion increases and the pulses are stretched to approximately 200 fs. A single prism compressor can be utilized to introduce negative dispersion and the pulses can be shortened to a pulse duration of ~ 68 fs.

Femtosecond laser pulses are generated by coupling the modes of the lasers passively via the non-linear optical Kerr effect, which is the most commonly used technique for the generation of ultrashort laser pulses [Pra12]. Information on the Kerr effect can be found in standard photonic books as e.g. in [Sal07].

A short trigger event is necessary to define the starting point of the measurements. It provides the same phase correlation between pump pulses and transients. An optical trigger is implemented by a photo diode with the nonlinear principle of two-photon absorption. A GaP (EPD-440-0/0.9) photo diode is used, which is able to absorb light in the range of 190 nm and 570 nm, i.e. it is transparent at the fundamental wavelength of the Ti:sapphire lasers. A small part of the probe and pump laser pulses is therefore redirected into it. One of the pulses is guided over a delay line before it reaches the trigger diode. The change of the delay between the pump and the probe pulse enables a shift of the starting point of the data acquisition to any point in the sampling window. Two-photon absorption in the photo diode provokes a distinct voltage peak that indicates the time, when both laser pulses reach the trigger simultaneously.

The measurements are performed with a collinear setup in reflection geometry. A half wave plate together with a polarizing beam splitter cube are used to regulate the pulse power and additionally to polarize the laser pulses perpendicularly. Pump and probe pulses are overlapped with a polarizing beam splitter cube. For focusing the laser beam on the surface of the sample to a spot size of approximately 2 µm, a 50x NIR microscope objective (MITUTOYO, JAPAN) with a numerical aperture of NA = 0.42 is used.
For the knowledge of the exact position of the laser beams on the sample, the sample can be illuminated additionally by white light and the reflected light is then redirected into a CCD camera.
The pump pulse incident on the sample excites coherent acoustic phonons, which are monitored by the change of the reflectivity by the delayed probe pulse. In this way it

is possible to obtain direct access to the dynamics of the coherent acoustic phonons in the investigated system. Details on the generation and detection processes of acoustic phonons are given in Chapter 2.4 and Chapter 2.5.

A photodetector with a bandwidth of 125 MHz measures the probe pulse after being reflected at the sample. Before the probe pulse is detected, the pump pulse is separated from it with a polarizer, when pump and probe pulse are polarized perpendicular to each other. Additionally, due to the offset of the wavelengths of pump and probe pulse, a bandpass filter can be used to stop the pump pulse from reaching the photo detector.

For the data acquisition, an oscilloscope card (COMPUSCOPE, GAGE 14200) is used with a bandwidth of 125 Mbit/s. A sampling rate of 100 MHz can be achieved. In about 2 minutes it is possible to obtain approximately 10^6 averages with a signal to noise ratio of up to 10^7.

The samples are mounted on an electronically controllable XYZ stage. For temperature dependent measurements this stage was replaced by a motorized XY heating/freezing system (MDS 600 - LINKAM SCIENTIFIC INSTRUMENTS).

3.4. Interpretation of Typical Features and Extraction of Measurement Data

In this section, a brief overview is given about the processing of the obtained measurement data. In Figure 3.4, the result of a typical pump-probe measurement is shown to explain generally the detected features.

In Figure 3.4 (a), the time-resolved reflectivity change is depicted of a semiconductor bilayer on a substrate. In the first few picoseconds, the transient shows a strong change in $\Delta R/R$, which stems from the ultrafast heating of the sample with the laser pulse. This is the so-called electronic peak. In dependence of the exact material parameters of the investigated sample, the sign of the electronic peak changes. The subsequent relaxation is caused by electron-electron and electron-phonon scattering, where the excess energy is transferred to the lattice and phonons are generated. The excitation mechanisms are hereby dependent on several parameters that are discussed in Chapter 2. After the initial dynamics, an oscillatory component arises that stems from the excitation of coherent acoustic phonons in the sample. A zoom-in is shown for a part of the transient for the better visibility of the oscillations.

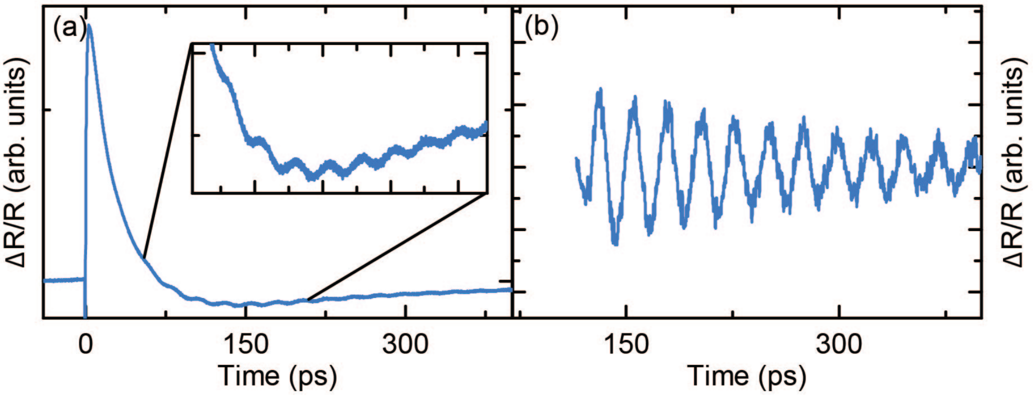

Figure 3.4.: Typical ASOPS measurement data. The depicted data were obtained from a semiconductor bilayer on a substrate. (a) Time-resolved reflectivity change with a zoom-in of the indicated area. (b) Corresponding extracted oscillation, where the slowly decaying background is removed.

In order to quantitatively analyze the vibrational contributions of the coherent acoustic phonons, the slowly decaying electronic and thermal background needs to be subtracted. Figure 3.4 (b) depicts the extracted oscillation.

Two methods are used in this thesis to extract these oscillations. One method is to apply a moving average. A smooth background fit is yielded through the calculation of a series of averages of different parts of the signal, which then can be subtracted from the signal. Best results are achieved if only one frequency component needs to be extracted.

The other utilized procedure is to fit a multi-exponential function to the time domain data and to subtract it. The phononic contribution of the measured transient is revealed. A fast Fourier Transformation is used to obtain the phonon spectrum and to extract the frequencies of the measured acoustic phonon modes.

CHAPTER 4

Interface Adhesion and Structural Characterization of Rolled-Up GaAs/InGaAs Multilayer Tubes

I WOULD RATHER HAVE QUESTIONS THAT CAN'T BE ANSWERED THAN ANSWERS THAT CAN'T BE QUESTIONED. – *Richard Feynman*

Rolled-up microtubes [Sch01a, Pri00], consisting of a thin strained bilayer that rolls up after being released from the substrate, were first realized in 2000. They are promising candidates for applications in various interdisciplinary fields. Examples are given in microfluidics [Gri12], where microtubes can be used as microfluidic channels to chemically sense polar solvents and biophysics [Xi14], where cell dynamics can be analyzed within the confined three-dimensional environment of the microtubes. In optoelectronics [Li09] rolled-up microtubes are used to construct quantum dot microtube lasers.

Additionally, the fabrication technique of these three-dimensional structures provides a new pathway for the realization of hybrid radial superlattices through the roll-up of a bilayer which results in a microtube consisting of a number of windings [Den04, Son06, Kra06, Den07].
An important step to simplify the fabrication process has been achieved by producing crystalline superlattices without the need to grow the full layer stack by molecular beam epitaxy (MBE) but instead by growing a strained bilayer of two materials, which – upon release from the substrate – undergoes a rolling-up process [Sch01a, Pri00]. This leads to the formation of multilayer rolls, i.e., radial superlattices.
A variety of potential applications for these rolled-up superlattices were already demonstrated. Thermoelectric devices containing rolled and pressed-back nanomembrane hybrid superlattices consisting of a composition of n- or p-doped single-crystalline semiconductors and a polycrystalline metal layer show reduced thermal transport [Gri14]. This offers potential for on-chip solutions for energy harvesters. Another possibility are inorganic rolled-up field effect transitors [Gri12] with transistor characteristics close to planar ones and the advantage of an ultracompact three-dimensional architecture. A

further application, metamaterial rolled-up optical hyperlens structures [Sch12], have been demonstrated.

However, the interest is not limited to the radial geometry of these multilayer structures. Firstly, the simplicity of the fabrication process [Sch01a, Pri00] compared to conventional techniques, renders this type of superlattice especially appealing. Secondly the possibility to use novel materials and material combinations [Den04, Den08, Bar14], which remain challenging in usual growth techniques, is advantageous. Examples for these novel materials are graphene, which can be integrated into current electronic technologies with the help of this roll-up technique [Bar14] and a variety of hybrid material combinations consisting of semiconductor/organic, Si/SiO$_x$ and semiconductor/ metal systems [Den06, Son07, Den07, Den08].

A crucial point, that determines and possibly hampers the applications potential of these multilayer tubes, is their internal mechanical contact, which is defined by the adhesion between individual boundary interfaces of the windings. An imperfect mechanical contact, for example, can result in heat accumulation and thermal stress [Ma15], influencing the quality factor of optical cavities [Son07, GS16]. Thus, a detailed characterization of these microstructures is necessary to establish a better understanding of their mechanical properties including the adhesion between the individual windings, similar to the investigations in other material systems by picosecond ultrasonics [Tho87, Tas98, Pel16, Gro17b].

Well-established techniques to experimentally study the acoustic phonons and eigenmodes of nanostructures like static Raman and Brillouin spectroscopy, which can provide access to the acoustic dynamics in the rolled-up superlattices, have already been applied [Ang12, Ber06, Wu96, Rod12]. However, at present, the frequency resolution that has been achieved with these techniques on single structures is very limited.

The results shown in this work are obtained by using ASOPS, which offers superior frequency resolution compared to conventional Raman and Brillouin spectroscopy. This renders invasive and thus destructive methods, e.g., focused ion beam based characterization in combination with SEM imaging, unnecessary. ASOPS allows to determine the distinct vibrational modes and to resolve single microtubes spatially.

In the next sections, the fabrication of the investigated samples will be explained followed by an overview of the six different types of samples and their respective structures.

In the beginning of the experimental part, measurements of a planar, MBE grown bilayer and a planar, MBE grown multilayer will be shown as a reference. This is followed by the presentation of the acoustic phonon modes of a variety of rolled-up multilayer tubes which are compared to the planar samples.

The experimental results and their interpretation will then be studied in the context of calculations of the phonon mode spectra obtained via a transfer matrix method including interface adhesion and the Rytov model which were both introduced in Chapter 2.3.5.

4.1. Sample Preparation and Structure

The sample fabrication process is described briefly in this section. A more detailed description of the fabrication process of the rolled-up multilayer tubes can be found in [Sch01b, Den02, Den08, Gri12].

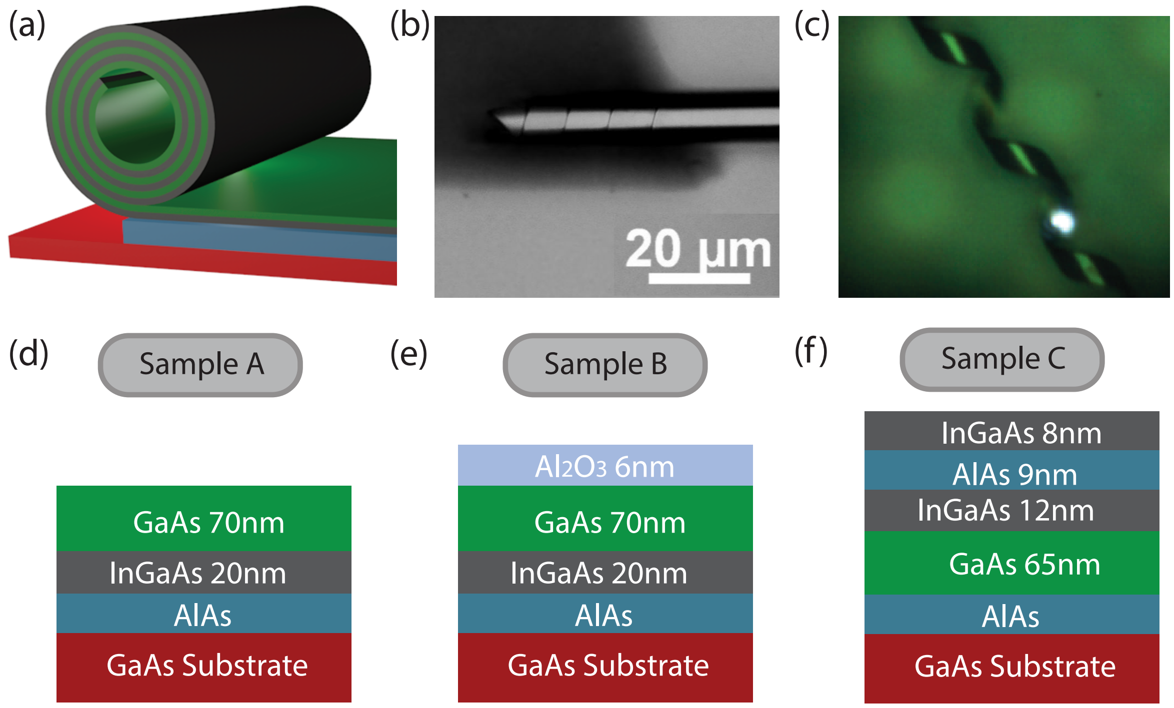

Figure 4.1.: (a-c) Investigated shapes of samples. (d-f) Sample structures of sample A, B and C. The samples all consist of a GaAs substrate with an AlAs sacrificial layer followed by the rolled-up multilayer tubes on top. Before the roll-up, (d) sample A consists of a layer of GaAs and $In_{0.2}Ga_{0.8}As$, while (e) sample B has an additional layer of Al_2O_3 on top of the GaAs and $In_{0.2}Ga_{0.8}As$ layers. (f) Sample C consists of a layer combination of $In_{0.2}Ga_{0.8}As$, AlAs, $In_{0.2}Ga_{0.8}As$ and GaAs. The rolled-up multilayer tubes consist of up to five windings. Sample A is investigated in a regular tubular shape as shown in (a) and a spiral shape as given in (c). Sample B has a cigar-like shape as shown in (b). Sample C is investigated in a regular tubular shape as shown in (a).

Six types of samples are investigated in the following. The layer structures can be divided into three samples A, B and C. Furthermore the sample geometry is distinguished in planar and rolled-up samples where sample A_p denotes the planar sample and sample A_r the rolled-up sample A. Corresponding notation is used for sample B and C. Sample A_{5MBE} is planar and consists of five repetitions of the bilayer used in sample A, all grown by molecular beam epitaxy.

The basic structures of the investigated superlattice structures of sample A, B and C are shown schematically in Figure 4.1 (d-f). In the following, the fabrication process of sample A is outlined. The general fabrication steps are similar for all samples.

Molecular beam epitaxy (MBE) is utilized to grow two layers on a GaAs substrate with a sacrificial AlAs layer between substrate and layers. In sample A_p, a layer of $In_{0.2}Ga_{0.8}As$ (with the thickness $d_{InGaAs} = 20\,nm$) and a layer of GaAs ($d_{GaAs} = 70\,nm$) are grown on top of the AlAs sacrificial layer (see Figure 4.1 (d)). The $In_{0.2}Ga_{0.8}As$ layer is compressively stressed through the MBE growth [Sch01a] due to the mismatch of the lattice parameters, as can be seen in Figure 4.2.

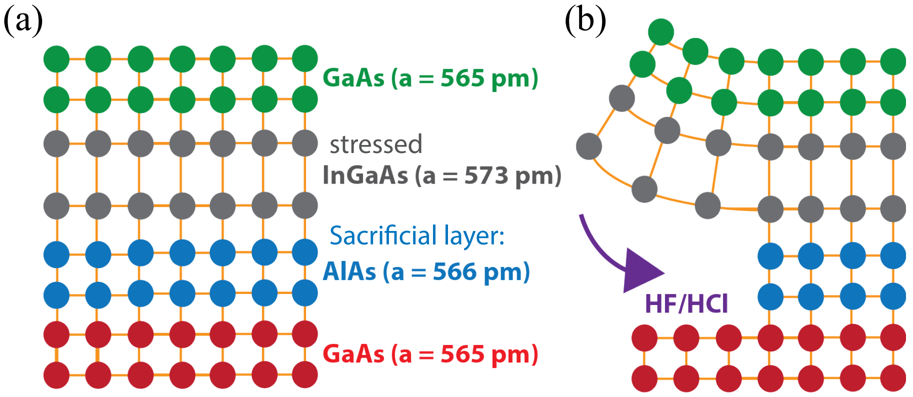

Figure 4.2.: Schematic of lattice structure of investigated samples. (a) MBE grown, planar layer stack. The $In_{0.2}Ga_{0.8}As$ layer is compressively stressed during the growth process due to a difference of the lattice parameters. The lattice parameters are given in the image. (b) The etchant starts to dissolve the sacrificial AlAs layer and hence the bilayer of $In_{0.2}Ga_{0.8}As$ and GaAs begins to roll up, releasing the stress in the $In_{0.2}Ga_{0.8}As$ layer. After the etchant is removed from the sample, the bilayer rolls up into several windings and a rolled-up multilayer tube is formed.

The bilayer is released using selective wet chemical removal with hydrogen chloride (HCl) of the sacrificial layer, which directly results in its roll-up into several windings denoted as sample A_r. This roll-up process is driven by the interatomic forces of the $In_{0.2}Ga_{0.8}As$ layer: the interatomic distances expand as soon as the AlAs is removed by HCl to release the inherent stress. This process in turn starts to stress the GaAs layer as its interatomic distance expands at the interface with the $In_{0.2}Ga_{0.8}As$ layer, as can be seen in Figure 4.2 (b).

For a controlled release of the layers, starting edges are defined by lithography before the removal of the sacrificial layer [Den09]. Depending on the shape of the starting edges the geometry of the final tube can be varied from a regular tubular shape (shown in Figure 4.1 (a)) to a cigar-like shape (depicted in Figure 4.1 (b)) with a varying amount of windings up to half-windings (Figure 4.1 (c)) [Bel06]. For details on the starting edges see Appendix A.1.

The number of windings determines the number of periods [Kra06] of the newly formed superlattice (SL), while the radius and the number of windings itself can be controlled by the thickness, strain and etching time of the epitaxial layers [Pri00]. The achieved radius R of the rolled-up tube can be estimated by

$$R = \frac{2(d_1 + d_2)^3}{3\epsilon d_1 d_2} \tag{4.1}$$

where d_1 and d_2 represent the layer thicknesses, respectively, and ϵ the strain [Den02]. For the investigated samples, the diameter of the multilayer tubes are approximately 10 µm and the number of windings range from 1 to 5 resulting in a tube wall thickness of up to 480 nm.

In comparison to the above described sample A, sample B possesses an additional layer of amorphous Al_2O_3 ($d_{Al_2O_3} = 6\,nm$) deposited by atomic layer deposition on top of the GaAs layer (Figure 4.1 (e)). The Al_2O_3 layer is used to avoid unintended side-rolling effects during release of the layer from the substrate. For more information on side-rolling effects see Appendix A.2.
In order to achieve a varying number of windings for sample B_r, a trapezoidal shape is cut in the MBE grown layers, the Al_2O_3 is deposited and then the necessary trench for stress relief is cut at one side of the trapezoid. Therefore the number of windings varies in sample B_r depending on the position on the tube, with a maximum of layers at the center. Sample B_r is also investigated after being pressed back to the substrate, hence being planar again.
A fixed number of windings at every part of the tube, like in sample A, is obtained by a rectangular cut. For comparison and as a reference sample, a plane SL with 5 double layers of GaAs ($d_{GaAs} = 70\,nm$) and $In_{0.2}Ga_{0.8}As$ ($d_{InGaAs} = 20\,nm$) was additionally grown by MBE, denoted as sample A_{5MBE}.

Sample C consists of the following layers: $In_{0.2}Ga_{0.8}As$ ($d_{InGaAs} = 8\,nm$), AlAs ($d_{AlAs} = 9\,nm$), $In_{0.2}Ga_{0.8}As$ ($d_{InGaAs} = 12\,nm$), GaAs ($d_{GaAs} = 65\,nm$) on top of the sacrificial AlAs layer and the GaAs substrate. The sample structure can be seen in Figure 4.1 (f). Similar to the Al_2O_3 layer, AlAs is used to avoid side-rolling effects and is used as an alternativ to Al_2O_3 for a possibly improved roll-up process.

4.2. Experimental Results

In the following, the results obtained from the as-grown, planar, unrolled samples A_p and B_p will be presented. These results will be followed by those of the planar MBE grown 5 period superlattice sample A_{5MBE}. Finally, this will be compared to the coherent phonon dynamics in the rolled-up mulitlayer tubes for sample types A_r and B_r, followed by a discussion of sample C and information will be given on the pressed sample B.

The results presented in Section 4.2.1 and Section 4.2.2 were published in Brick et al. [Bri17b].

4.2.1. Planar Samples

Sample A

Figure 4.1 (d) shows the structure of the planar, MBE grown sample A_p which will be presented first.

Upon excitation of the sample with a femtosecond laser pulse, the time-resolved relative reflectivity change $\Delta R/R$ given in Figure 4.3 (a) can be obtained of sample A_p. Explanations of the excitation processes and the detection mechanisms can be found in Chapter 2.4 and Chapter 2.5, respectively. The slowly decaying electronic and thermal background is subtracted from the time domain data and the vibrational contributions of the acoustic phonons, which can be seen in the inset of Figure 4.3 (b), are extracted.

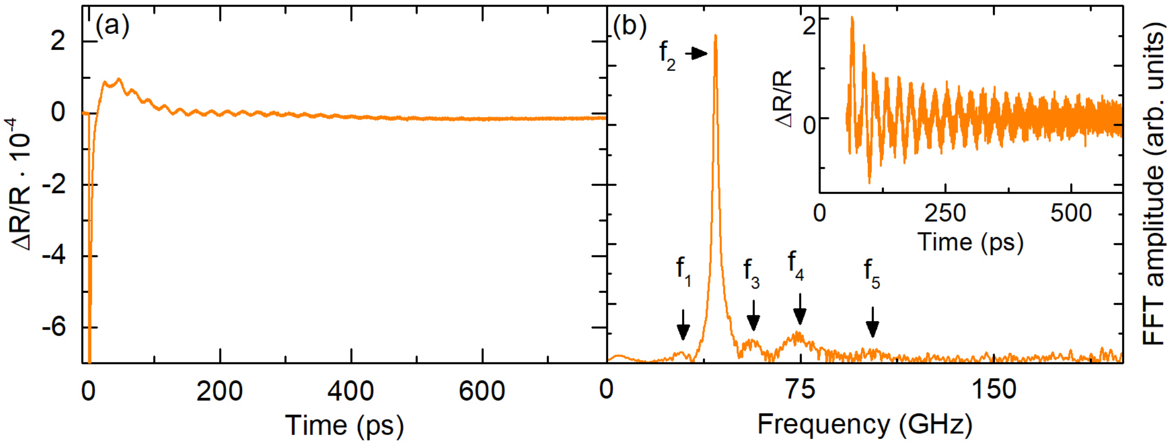

Figure 4.3.: (a) Time-resolved reflectivity change of the planar sample A_p. (b) FFT spectrum of the planar, sample A_p as in Figure 4.1 (d). The inset shows the extracted time-resolved reflectivity change.

The respective Fast Fourier Transformation (FFT) of the time domain data of sample A_p is shown in the main part of Figure 4.3 (b). The FFT reveals distinct peaks at

frequencies of $f_1 = 28\,\mathrm{GHz}$, $f_2 = 42\,\mathrm{GHz}$, $f_3 = 56\,\mathrm{GHz}$, $f_4 = 73\,\mathrm{GHz}$ and $f_5 = 103\,\mathrm{GHz}$. The most prominent frequency peak at 42 GHz results from time-resolved Brillouin scattering in the underlying GaAs substrate. The origin of the associated change in the refractive index is partially reflected probe light from the strain pulse. This light interferes with the light being reflected from the top of the sample giving rise to time-resolved Brillouin oscillations with frequencies corresponding to the speed of sound in the material [Dev15]. Brillouin oscillations are discussed in detail in Chapter 2.5 of this thesis.
The assignment of the observed frequency mode to a Brillouin oscillation can be confirmed by calculating the Brillouin frequency of GaAs, $f = 2nv_{\mathrm{GaAs}}/\lambda = 42\,\mathrm{GHz}$, where $n = 3.66$ is the refractive index, $v_{\mathrm{GaAs}} = 4730\,\mathrm{m\,s^{-1}}$ the longitudinal sound velocity of bulk GaAs, and $\lambda = 820\,\mathrm{nm}$ the wavelength of the probe laser pulse. The obtained value is in good agreement with the measured frequency of the most prominent peak.
Additionally, this finding can be supported by comparison to a reference measurement on a pure bulk GaAs substrate. In Figure 4.4, the FFT of the planar sample $\mathrm{A_p}$ is compared to the FFT of pure bulk GaAs. The inset shows the transient.

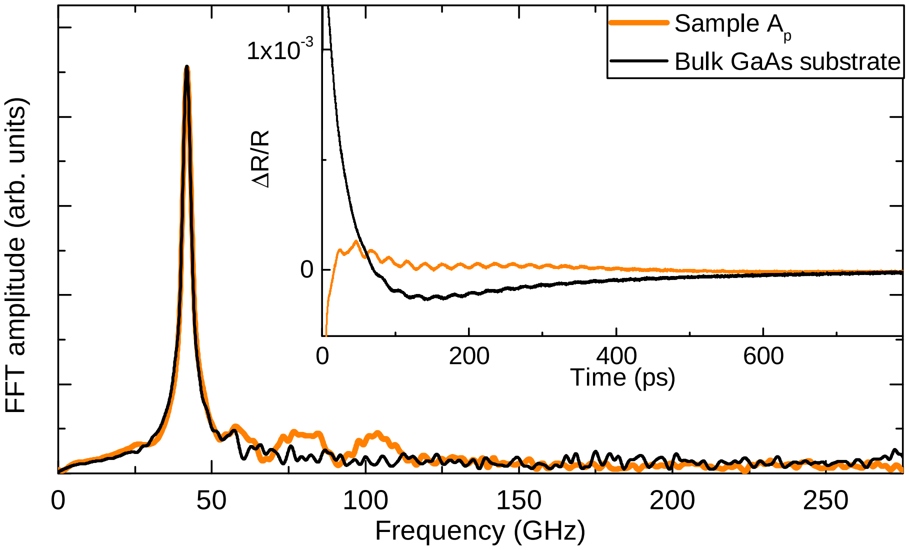

Figure 4.4.: FFT of the pure bulk GaAs substrate (black line) compared to the planar sample $\mathrm{A_p}$ (orange line). The orange line is twice as thick as the black one and the FFTs are smoothed for better visibility of the peaks. The frequency mode at 42 GHz can be attributed to the GaAs substrate. The inset depicts the time-resolved reflectivity change.

The frequency peak at 28 GHz, visible in Figure 4.3 (b), represents the solution of the eigenmode of a single layer with the combined thicknesses of both layers. Details on the eigenmode calculation of a bilayer on a half-infinite substrate can be found in Chapter 2.3.
The other observed frequencies represent higher harmonics of the fundamental thickness

oscillation as explained further below in Figure 4.6. The modes attributed to the thickness oscillation of the layers $In_{0.2}Ga_{0.8}As$ and GaAs vanish for the bulk substrate, as expected. The mode at 42 GHz persists and can thus be unambiguously attributed to the time resolved Brillouin scattering in the GaAs substrate.

Sample B

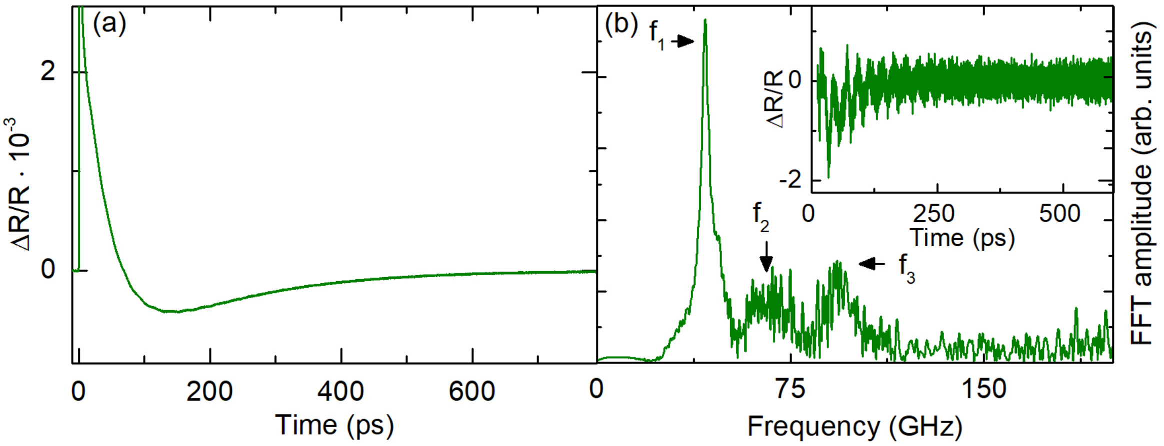

Figure 4.5.: (a) Time-resolved reflectivity change of the planar sample B_p. (b) FFT spectrum of the planar, sample B_p as in Figure 4.1 (e)). The inset shows the extracted time-resolved reflectivity change.

The FFT and time-resolved reflectivity change of the planar sample B_p (the structure was given in Figure 4.1 (e)) are given in Figure 4.5. Distinct frequencies are observed at $f_1 = 42\,\text{GHz}$, $f_2 = 67\,\text{GHz}$ and $f_3 = 93\,\text{GHz}$. Similarly to sample A_p, a frequency peak at 42 GHz can be found also originating from the time-resolved Brillouin scattering in the GaAs substrate. The remaining frequency peaks are a result of the combined oscillation of the three layer system and higher harmonics.

The measured frequency modes versus the mode number for the samples A and B on a GaAs substrate and for the same samples as “freestanding membranes” are shown in Figure 4.6 (left). The frequency modes were obtained from the FFT measurements shown in Figure 4.6 (right). The measurements for the freestanding membranes were obtained using one winding of the rolled-up samples A_r and B_r, as explained later on in detail. For the planar samples A_p and B_p, the frequency modes were obtained experimentally and plotted against the mode number for two cases: for the samples on a substrate and for the samples as a freestanding membrane. As expected a linear relation with different slopes is found, depending on the thickness of the sample, the sound velocity and the boundary conditions of the respective sample.

The lifetimes of the different modes strongly differ. The Brillouin oscillation is observed as long as the strain pulse traveling into the substrate is probed by the probe pulse, i.e. for a time given by $t = (\alpha v)^{-1}$ with the absorption coefficient α and the sound velocity v. This relation is only valid when the acoustic damping is neglected. The spectral width and lifetimes of the modes resulting from the eigenmodes of the top layers are determined by the rapid dissipation through coupling to the substrate. This allows the differentiation of the different layer systems by their eigenmode spectrum.

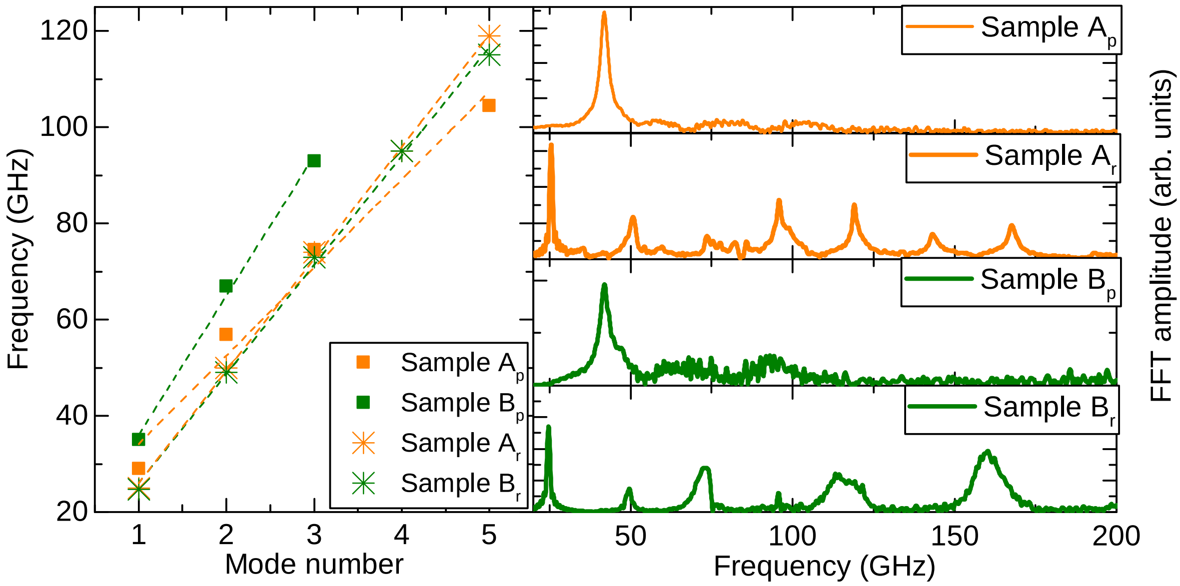

Figure 4.6.: Frequency peak as a function of the mode number for sample A (orange dots) and sample B (green dots) on a substrate and as a freestanding membrane (obtained from measurements on one winding of sample A_p and B_p), respectively, extracted from experimental results.

Planar Sample A with 5 Repetitions

The planar superlattice sample A_{5MBE} will be investigated in this section. Coherent acoustic phonons are excited and detected in the planar MBE grown superlattice with a repetition of 5 double layers of GaAs and $In_{0.2}Ga_{0.8}As$.

Figure 4.7 shows the extracted time-resolved reflectivity change of sample A_{5MBE} shown in orange.

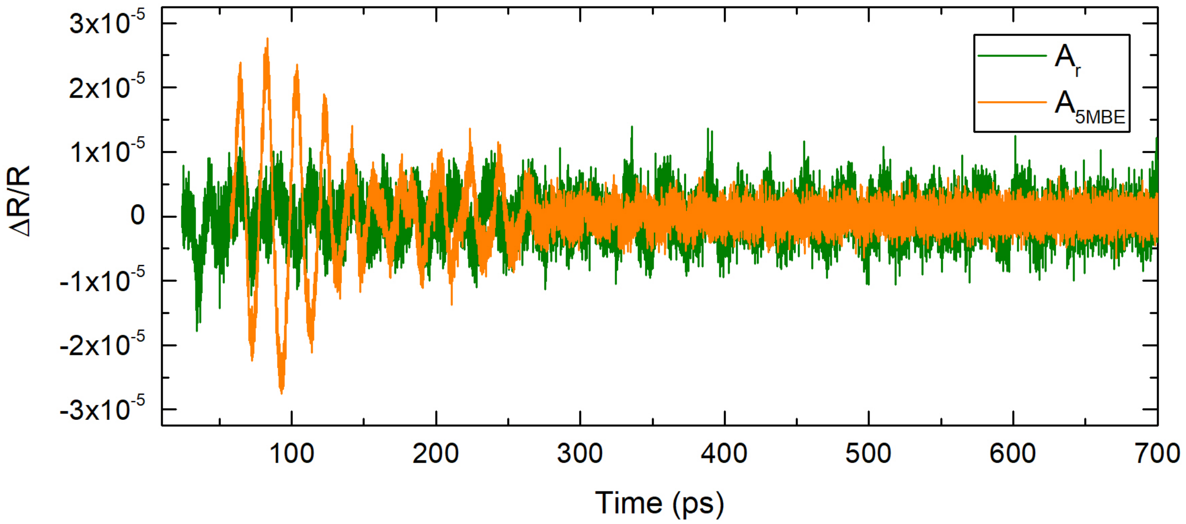

Figure 4.7.: Extracted time-resolved reflectivity change of the planar MBE grown sample A_{5MBE} (depicted in orange) and of the rolled-up mulitlayer tube A_r (depicted in green).

Figure 4.8 (a) shows the obtained frequency modes (bottom part) and theoretical calculations (top part) of the acoustic phonon dispersion relation of the sample A_{5MBE}, which will be discussed in the following.

The mode spectrum exhibits triplet structures that are characteristic for acoustic phonon modes of a superlattice [Bar98]. In order to gain a better quantitative understanding, the acoustic phonon dispersion relation of an SL with two layers by means of the elastic continuum model according to Rytov [Car89, Ryt56, Ruf98] was calculated. Details on the calculation of dispersion relations with the Rytov model are given in Chapter 2.3.5.

The blue line in the top part of Figure 4.8 represents the calculated back folded acoustic phonon dispersion relation with the observed $2q_{\text{Probe}}$ modes at the intersection of the $2q_{\text{Probe}}$ line (horizontal red line) and the dispersion relation. The following parameters were used: for the sound velocities $v_{\text{InGaAs}} = 4550\,\text{m}\,\text{s}^{-1}$ and $v_{\text{GaAs}} = 4730\,\text{m}\,\text{s}^{-1}$ and for the densities $\rho_{\text{InGaAs}} = 5384\,\text{kg/m}^3$ and $\rho_{\text{GaAs}} = 5320\,\text{kg/m}^3$.

The experimentally obtained frequency modes show an excellent agreement with the

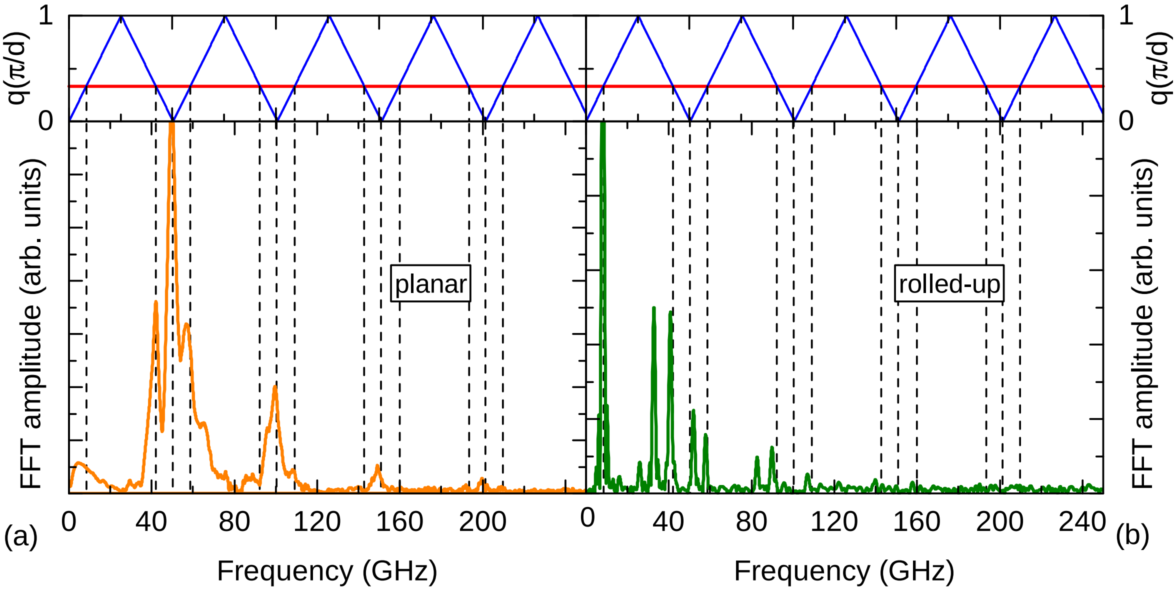

Figure 4.8.: (a) The top part of the figure reveals the calculated back folded acoustic phonon dispersion relation (blue line) with the observed $2q_{\text{Probe}}$ modes at the intersection of the $2q_{\text{Laser}}$ line (horizontal red line) and the dispersion relation. The bottom part displays the FFT of sample $A_{5\text{MBE}}$, the MBE grown SL with 5 double layers of GaAs and $In_{0.2}Ga_{0.8}As$. The frequency peaks determined from the experimental results match well with the calculated modes obtained from the acoustic phonon dispersion relation (vertical dotted lines) calculated by the Rytov model. (b) is similar to (a), but for the rolled-up SL sample A_r. The frequency peaks appear at similar positions as for sample $A_{5\text{MBE}}$ but the peaks of the MBE grown sample are broadened compared to the ones from sample A_r.

calculated dispersion relation despite the small number of periods of the SL. Thus, it can be concluded that 5 periods are, in this case, sufficient to observe acoustic SL behaviour despite results which stated a larger number of repetitions [Dw93, Tri02b]. The spectrum is independent of the position on the sample.

The measurements demonstrate broadening of the frequency peaks overlapping with the surrounding frequency peaks. This broadening of the line width of the mode can be explained when considering the underlying substrate: the modes can propagate into the substrate; they are not neatly defined.

4.2.2. Rolled-up Multilayer Tubes

Rolled-up Multilayer Tubes – Sample A

In the next step, the previously discussed results of the planar MBE grown superlattice $\mathrm{A_{5MBE}}$ will be compared to the superlattice structure obtained by the roll-up process, i.e. the rolled-up multilayer tube of sample $\mathrm{A_r}$.

The extracted oscillation is shown in Figure 4.7 (green line). In Figure 4.8 (b) the FFT of the rolled-up SL is compared to the previously discussed sample $\mathrm{A_{5MBE}}$ in Figure 4.8 (a). The distinct difference that can immediately be recognised is the absence of a triplet structure as observed in Figure 4.8 (a). The dispersion relation and the expected mode positions are the same as before and are again marked with dashed vertical lines to make this point more apparent. While some of the observed modes correspond well to the theoretical calculations, others cannot be easily explained by this theoretical approach. The additional modes appear at frequencies of $f = 26\,\mathrm{GHz}$, $32\,\mathrm{GHz}$ and $83\,\mathrm{GHz}$. These modes can be explained by weak adhesion between the individual double layers. We will come back to this point later on.
From the line width of the obtained frequency spectra one can see that the modes of sample $\mathrm{A_r}$ have a longer life-time compared to sample $\mathrm{A_{5MBE}}$. The line width for sample $\mathrm{A_{5MBE}}$ is almost twice compared to $\mathrm{A_r}$. For example, the mode widths around $50\,\mathrm{GHz}$ are $\omega_r = 2.45\,\mathrm{GHz}$ and $\omega_{MBE} = 4.13\,\mathrm{GHz}$. The longer lifetime can be attributed to the new boundary conditions for this sample type. The upper part of the tube exhibits two air interfaces and thus shows increased confinement compared to the sample deposited on a substrate.

Furthermore, it is important to emphasize that the tube structures of sample $\mathrm{A_r}$ also show distinct differences in their mode spectrum when investigating different spatial positions along the multilayer tubes. An example of this behaviour is given in Figure 4.9. More details on the variation of measurements of sample $\mathrm{A_r}$ are shown later on in Figure 4.11.
Figure 4.9 (a) shows the extracted oscillations of the time domain data and the respective FFT of position 1 as already presented in Figure 4.8 (b). Figure 4.9 (b) shows the data obtained at a different position, position 2, on the same tube. A considerable increase in the mode spacing is observed. These findings are discussed in the following.

So far, the theoretical calculations have considered the system as an infinite superlattice. This approach worked well for the MBE grown superlattice but cannot account for the observations of the tube spectra. Therefore, a transfer matrix approach is now being used. The acoustic eigenmode spectrum from one single double layer up to five double layers of GaAs and $\mathrm{In_{0.2}Ga_{0.8}As}$ is calculated in order to gain better insight into the acoustic properties of the tubes. Details on the calculations with the transfer matrix formalism

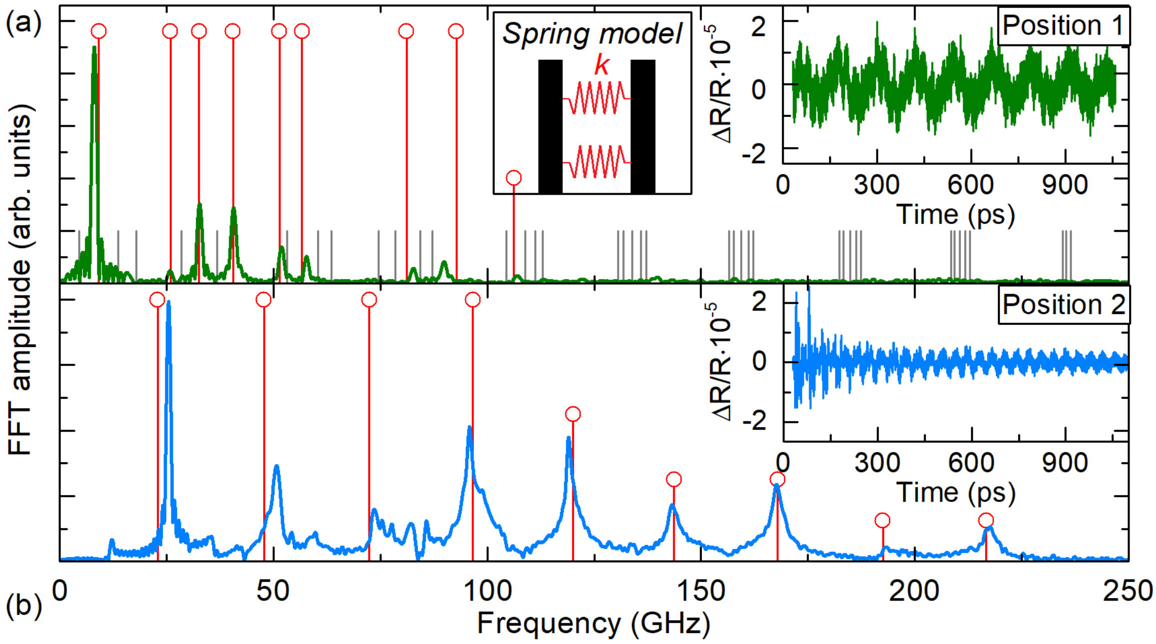

Figure 4.9.: (a) The inset shows the extracted oscillations at position 1 of sample A (with a number of 5 windings). In the main part of the figure the respective FFT is shown. The vertical lines in the FFT spectrum are the frequency modes obtained from calculations based on the transfer matrix method including a spring model, as shown schematically. The corresponding sound velocities are listed in the main text. (b) Same as (a) but for position 2.

can be found in Chapter 2. The same sound velocities and densities as indicated before for the Rytov model were used.

The results of the calculations are presented as vertical lines in Figure 4.9. The modes that show the best coincidence with the measured spectrum are marked in red, while all other modes are drawn in light gray for better visibility.

The mode spectrum for position 2, presented in Figure 4.9 (b), shows very good agreement with the calculations of a single bilayer and not a layer stack. Therefore, it can be concluded that, at this tube position, the individual windings are not mechanically coupled and consequently frequencies of the oscillation of a single bilayer of GaAs and $In_{0.2}Ga_{0.8}As$ can be observed. The oscillations of the detached single bilayer contain the fundamental mode of the thickness oscillation which can be calculated to be $f = v/2d = 26\,\text{GHz}$ and higher harmonics up to 220 GHz, where v is again the combined weighted sound velocity of the layers, and d the total bilayer thickness.

Explaining the eigenmode spectrum of position 1, presented in Figure 4.9 (a), is, however, not as straightforward. A first attempt assuming perfect adhesion between the 5 bilayers did not yield results similar to the observed mode spectrum. Therefore, a massless spring between the bilayers is introduced into the transfer matrix calculations to account for non-perfect adhesion. A schematic of this spring model is depicted in the middle part of Figure 4.9 (a) and was also described in Chapter 2.

The assumption of non-perfect interface adhesion is reasonable, as this was already observed for position 2. A single tube exhibits areas where the roll-up process is not perfect but partly detached and the characteristic mode spectrum of a single bilayer is detected.

This finding is supported by Figure 4.10, which shows the scanning electron microscopy image (SEM) of two cross sections at different positions of sample $\mathrm{A_r}$, obtained by focused ion beam milling. Parts of the rolled-up multilayer tube can be seen where the layers seem to be attached very nicely, while there are also parts where there does not seem to be any direct coupling at all.

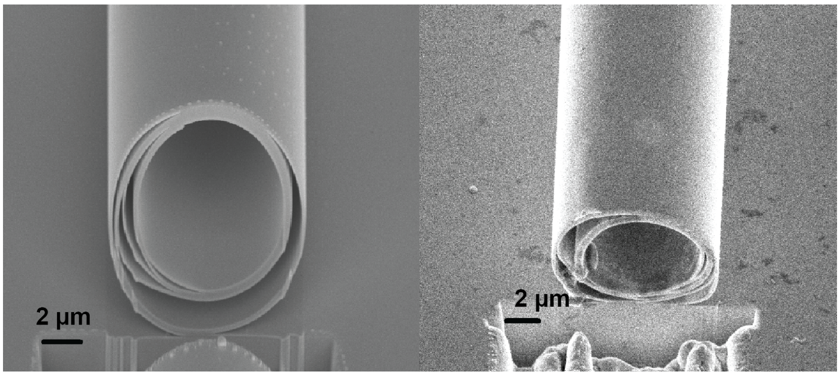

Figure 4.10.: Scanning electron microscope images of two cross sections of sample $\mathrm{A_r}$ obtained by focused ion beam milling. Parts where the windings are closely attached, and parts where they are not attached at all, can be seen.

The calculation presented for position 1 in Figure 4.9 (a) uses a massless spring between the individual bilayers and assumes the simplest case with the same spring constant between each bilayer for the mechanical coupling between the neighbouring windings.

A spring constant of $k = 5 \cdot 10^{9}\,\mathrm{kg\,m^{-2}\,s^{-2}}$ is obtained in this case, which is several orders of magnitude smaller than typical metal/semiconductor contacts ($k = 6.32 \cdot 10^{18}\,\mathrm{kg\,m^{-2}\,s^{-2}}$) [Ant06, Gro13] and epitaxially grown semiconductor layers. The calculated modes that show the best coincidence with the measured spectrum are marked in red, while all other modes are drawn in light gray for better visibility in Figure 4.9 (a). A good qualitative agreement between the measured eigenmode spectrum and the calculated modes can be achieved. Therefore, one can conclude that the adhesion at this part of the tube is indeed coupling all neighbouring windings and provides the spring constant as given above. If the coupling by adhesion varies between different neighbouring windings, or if some of the windings are not coupled at all, then the mode specta show a considerably more complicated pattern. However, such spectra can still be distinguished from the aforementioned cases at position 1 and 2. Furthermore, it is possible to assume that the main part of the signal stems from the upper part of the multilayer tube, which effectively constitutes a type of freestanding membrane. This also accounts for the similar damping times of the two presented cases which are comparable in the time domain, as shown in Figure 4.9, due to the absence of a direct substrate coupling.

For a deeper understanding, acoustic phonon mode spectra of partially coupled tube windings of sample A_r and spatially resolved scans along the length axis of individual tubes are discussed. The phonon modes measurements for various tube positions of sample A_r, consisting of 5 windings, are shown together with the phonon modes calculated with the transfer matrix model including the massless spring in Figure 4.11 (a).

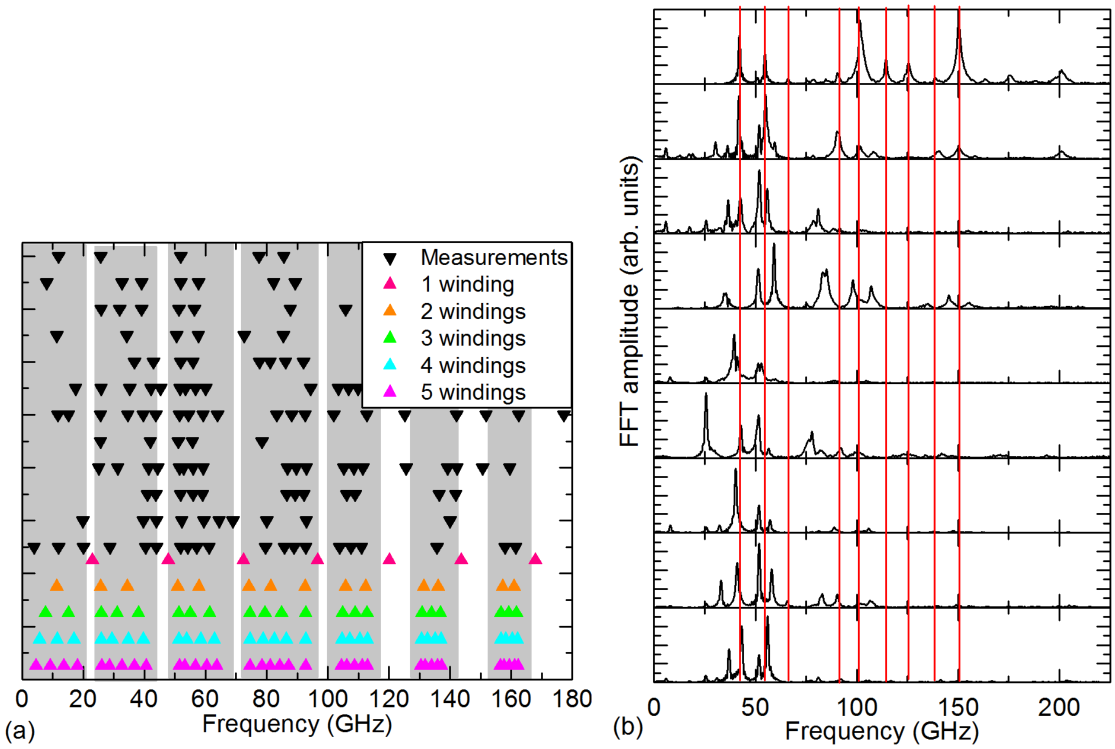

Figure 4.11.: (a) Each row shows the peak frequencies in the frequency spectrum of different measurements of sample A_r (black triangles) compared to calculations for 1 to 5 windings (coloured triangles). Areas of frequency groups are marked by a gray rectangle for better visibility. (b) FFT at different positions along a multilayer tube of sample A_r. A clear shift of the frequencies is visible, the vertical red lines are a guide to the eye to see the shift of the frequencies more clearly. The depicted measurements were obtained all on spots of the same sample but with varying distances between each spot.

The system complexity for 5 windings, including varying adhesion between individual windings, results in a considerable number of free parameters, which impedes a quantitative modeling. Depending on the coupling, the multilayer tubes undergo frequency shifts or a superposition of mode spectra for sub-systems including one or more windings. Despite the complex mode spectra, a grouping of the modes becomes apparent. This grouping is captured by the simulations for different winding numbers. It is indicated by the gray shaded areas, which show the expected mode ranges given by the simulations for up to 5 windings in Figure 4.11 (a).

In Figure 4.11 (b) FFTs at different positions along a multilayer tube of sample $\mathrm{A_r}$ are shown. A clear shift of the frequencies is visible. However, an unambiguous assignment of the phonon modes to a specific number of coupled windings is not possible in this case. This multilayer tube is one of the examples where the windings are neither sufficiently coupled nor decoupled. Nevertheless, this finding by itself already conveys important information about the rolled-up multilayer tube's structural quality. Furthermore, it is possible to observe the distinct changes the mode spectra undergo while scanning along the multilayer tube, which reveals a strongly inhomogeneous tube structure without sufficient winding adhesion.
In general, parts of the rolled-up multilayer tube where the layers are tightly attached can be distinguished from parts where they are loosely attached, which agrees with the observations of non-uniform structures in tubes that were shown in the scanning electron microscopy image in Figure 4.10.

The sound velocities used in the transfer matrix calculations deviate from the bulk velocities, which can be attributed to residual strain in the layers [Ber06]. Although the layers are released from the sacrificial layer, some residual stress remains. This effect has been taken into account in the calculations, resulting in modified sound velocities. When a layer is compressed, the sound velocity increases and this leads to a shift of the frequency to higher values. Analogously, in a layer which is tensile stressed, the sound velocity decreases [Bho06]. The best agreement between theory and experiment is obtained for the following sound velocities: for sample $\mathrm{A_r}$ they are found to change by a factor of 1.05 to $v_{\mathrm{InGaAs}} = 4778\,\mathrm{m\,s^{-1}}$ and with a factor of 0.89 to $v_{\mathrm{GaAs}} = 4210\,\mathrm{m\,s^{-1}}$. As expected, the sound velocity in the $\mathrm{In_{0.2}Ga_{0.8}As}$ layer is increased as this layer is compressed, and v_{GaAs} is decreased as this layer is tensile stressed [Bho06]. As can be seen for the bilayer in Figure 4.9 (b), the key features of these measurements are well reproduced by the calculations. A spring constant of $k = 50 \cdot 10^{8}\,\mathrm{N\,m^{-1}}$ is assumed in this case. Minor deviations between theory and experiment can be due to the presence of an oxide layer on top of the sample [Den07, Den02].

Rolled-up Multilayer Tubes – Sample B

In the following, the results obtained from the multilayer tubes of sample B_r, which exhibit an increasing winding number, are presented. In Figure 4.12, the optical microscope image of sample B_r is depicted. From left to right the number of windings increases from 1 to 5. Each area of the tube with a specific winding number was addressed and measured separately. This system is investigated, as it is possible to assign the measured modes to a certain number of windings.

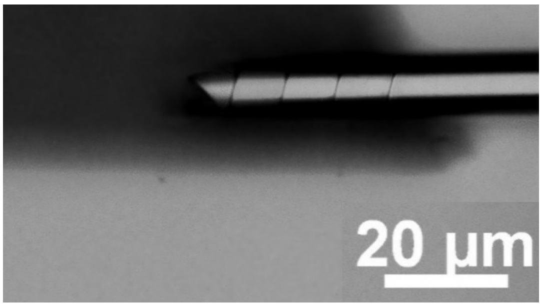

Figure 4.12.: Image of cigar-like shaped sample B taken with an optical microscope. From left to right the number of windings changes from 1 to 5.

Figure 4.13 (a) and (b) show the extracted oscillations and the respective FFTs, sorted for winding numbers from 1 to 5. The time domain data in Figure 4.13 (a) already reveals a decrease in the acoustic signal response with increasing winding number.
This becomes even more apparent in the frequency domain shown in Figure 4.13 (b). One can observe the characteristic eigenmode spectrum of the single triple layer, which is similar to the results of the single bilayer of the previous sample A_r, shown in Figure 4.9 (b). With increasing winding number the mode spacing decreases and a strong decrease in the acoustic signal amplitude can be found. In fact, for 4 and 5 windings the time resolved Brillouin contribution from the GaAs substrate dominates the signal completely and the tube modes almost vanish. The acoustic contributions are highlighted with red arrows for better visibility.
Before this intriguing point is discussed, first the mode spectra with up to three windings will be studied in more detail. Following the earlier used approach, the eigenmode spectra are calculated including a massless spring connecting individual windings. For sample B_r, the sound velocities change due to the roll-up by a factor of 1.003 to $v_{\mathrm{InGaAs}} = 4564\,\mathrm{m\,s^{-1}}$ and by a factor of 0.9 to $v_{\mathrm{GaAs}} = 4273\,\mathrm{m\,s^{-1}}$.

The vertical lines in Figure 4.13 (b) represent the calculated modes with a spring constant value of $k = 5 \cdot 10^9\,\mathrm{N\,m^{-1}}$. Matching modes are marked in red while the other modes are depicted in gray for a better visibility.
Again, good agreement between the measurement of the single three layer winding and the calculations where the spring constant does not have any influence on the calculation

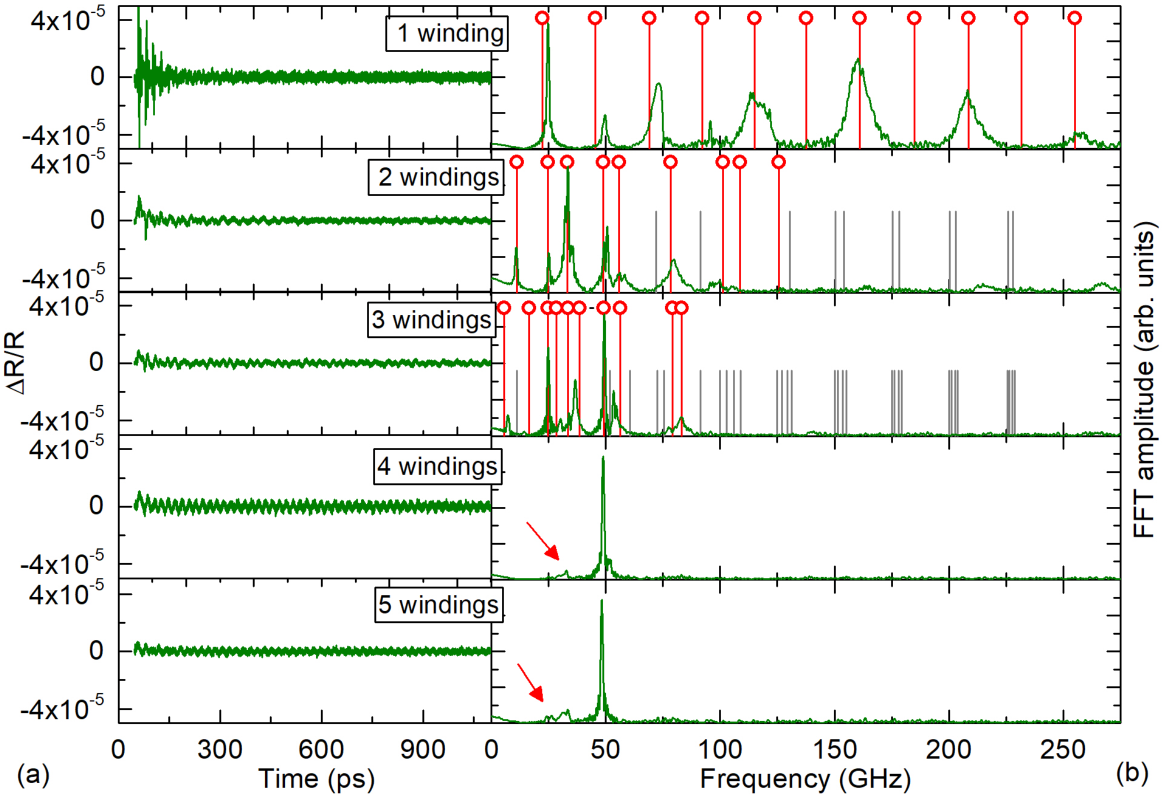

Figure 4.13.: (a) Extracted oscillations of the time-resolved reflectivity change in different parts of the coil with a number of windings from 1 to 5. The lifetime increases and the amount of higher frequency components decreases with the increasing number of layers. (b) Respective FFTs. A transition from the frequencies of a single oscillating bilayer towards the modes of a superlattice is visible. The vertical lines represent the calculated modes. All matching modes are marked in red, while the others are marked in gray for better visibility. For 4 and 5 windings, the acoustic contributions are marked for better visibility with a red arrow.

is achieved. The same results as without a spring are obtained. Small deviations may be caused due to the assumption of a planar geometry. Although the laser spot is smaller than the tube width, the weak curvature may influence the mode spectrum slightly. A good qualitative agreement between the calculations and the observed spectra for increasing winding numbers is also found. The main features and the general trend of decreasing mode spacing with increasing winding number are reproduced.

A more detailed look at the sample structure is required for the discussion of the mode spectra for 4 and 5 windings, where most frequency modes disappear. The detection process might be changed. The main difference between the multilayer tube of sample B_r and the tubes of sample A_r presented in Figure 4.9, where the acoustic contributions are still clearly visible for a 5 windings tube, is the presence of the additional Al_2O_3 layer.

With increasing number of windings, the possible contribution of this layer to the overall acoustic dissipation increases and can thus be responsible for a decrease of the detected phonon amplitudes.

Another point which needs to be taken into account is, that the tubes effectively form a kind of optical cavity, where the upper and lower parts of the tube resemble mirrors with an air gap in between. This geometry can affect the detection process of coherent acoustic phonons in the multilayer tubes and lead to a suppression of the detected phonons. Details are given in Figure 4.14. Due to the high sensitivity of this cavity effect to the air spacer thickness, i.e. the tube's diameter, a quantitative modelling of the detection process even for less winding numbers is strongly hindered.

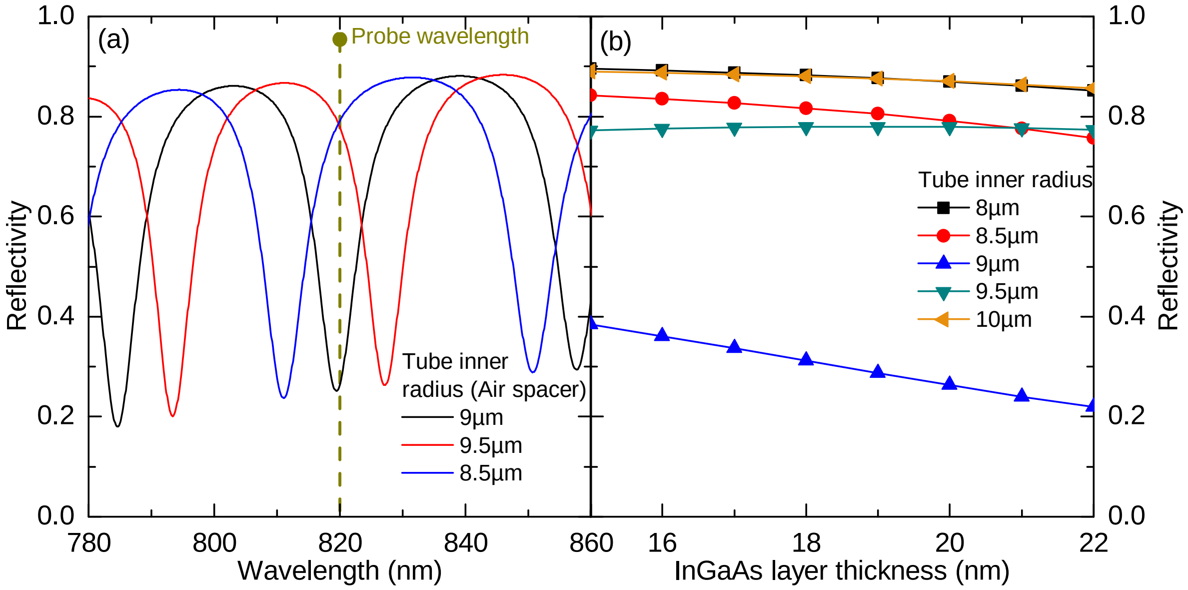

Figure 4.14.: (a) Simulations of the reflectivity of sample A_r as a function of the laser pulse wavelength for three different tube inner radii (air spacer) with $r = 9\,\mu m, 9.5\,\mu m$ and $8.5\,\mu m$. (b) Simulations of the reflectivity of sample A_r, plotted as a function of the $In_{0.2}Ga_{0.8}As$ layer thickness for different tube inner radii ranging from $r = 8\,\mu m$ to $r = 10\,\mu m$.

In Figure 4.14 simulations of the reflectivity are shown. In Figure 4.14 (a), it can be seen that the reflectivity of the sample depends strongly on the air gap in the cavity of the rolled-up tube, i.e. the inner tube radius. For a probe wavelength of 820 nm, the inner tube radius determines whether it is positioned on a slope or a minimum. In the first case high sensitivity is expected, while changes in the reflectivity should be minimal for the second case.

This behaviour was investigated in more detail in Figure 4.14 (b), where the presence of coherent phonons by reflectivity calculations for several $In_{0.2}Ga_{0.8}As$ thicknesses is simulated. The slope at the nominal thickness of 20 nm is here a measure of the detection

sensitivity and is strongly dependent on the inner tube radius.
It is important to note that the actual phonon-induced thickness change is far below the nanometer range. However, the data shown here is presented in a broader thickness range in order to account for small deviations in the nominal layer thickness. The above discussion also holds true, e.g. if the nominal thickness is 21 nm.

Despite these current limitations for sample structure B_r, it is possible to unambiguously distinguish the number of windings in these multilayer tubes for up to three windings, if the individual windings are sufficiently coupled by adhesion. For sample structure A_r, it is possible to observe acoustic features for up to five windings.

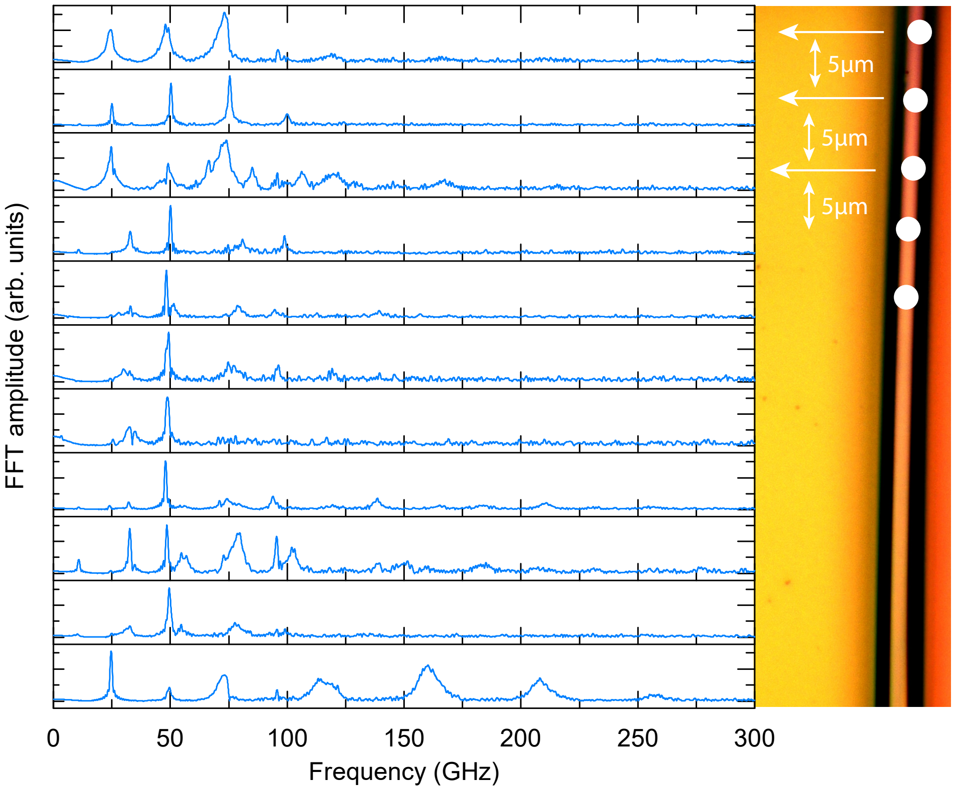

Figure 4.15.: Scan along a rolled-up multilayer tube. Each FFT spectrum has a distance of approximately 5 µm to the next spectrum. The right part shows a microscope image of the tube, where the measured spots are indicated by white circles. Arrows indicate the corresponding FFT spectrum on the tube for the first measurements.

In addition, the inhomogeneous behaviour can be observed again by scanning the position along the multilayer tube. The spectra in Figure 4.15 show the measurements obtained along a tube with an interval spacing of approximately 5 µm. Although the distance between the measurements is small, the spectra change considerable.

4.2.3. Half-windings

Sample A

As described above, so-called half-windings or spirals can be obtained when stripes roll up under a certain angle to the crystal direction [Bel06]. In Appendix A.1 information about the roll-up are given. The half-windings contain only InGaAs and GaAs as in sample A. In the inset of Figure 4.16 (a), a microscope image of the half-winding sample is depicted.

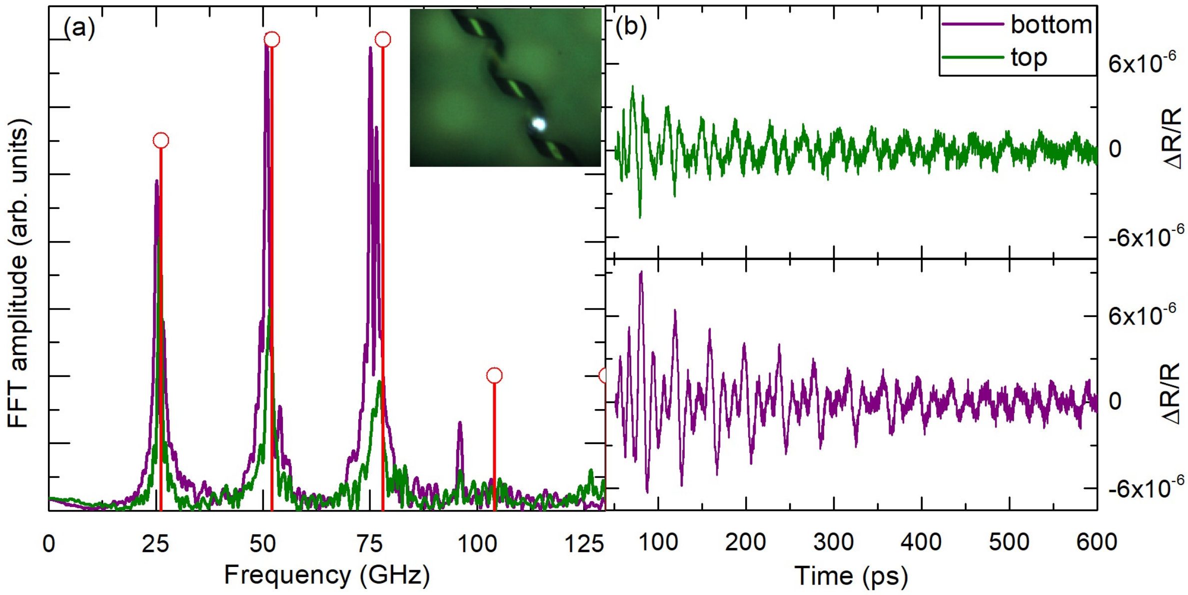

Figure 4.16.: (a) FFT of half-windings. A comparison of a measurement where first $In_{0.2}Ga_{0.8}As$ is excited ("top", depicted in green) and a measurement where first GaAs is excited ("bottom", depicted in purple) can be seen. The red vertical lines show the calculated modes for a freestanding bilayer membrane of GaAs and $In_{0.2}Ga_{0.8}As$. The inset contains a microscope image of the half-windings. (b) Extracted oscillations of the time-resolved reflectivity change for both measurements.

By turning the bilayer it is possible to measure it from both sides, once from the InGaAs side and then from the GaAs side. For the parts where the GaAs is on top, the bilayer is in contact with the substrate. For the parts where InGaAs is on top, it is completely freestanding. Contrary to the expectations, the bottom part shows an almost identical spectrum as the top part. Figure 4.16 (b) shows the extracted oscillations and (a) the respective FFTs of the measurements. The results are displayed in green (for InGaAs on top of the half-winding) and in purple (for InGaAs on the bottom of the half-winding).

The red vertical lines in the FFT indicate the modes calculated by the transfer matrix model for a freestanding membrane. The calculated modes are in good agreement with the experimental ones. Almost the same frequencies are obtained for both configurations with only a slight difference for the measurement when InGaAs is on top or on bottom of the half-winding. Hence, the adhesion between the parts of the bilayer, where it is in contact with the substrate, is negligible.

4.2.4. Further Sample Variations

Pressed Superlattices – Sample B

Rolled-up multilayers can also be used to produce planar superlattices by pressing the rolled-up tubes mechanically using a nanoimprinter [Zan09, Gri14]. Again, this is a promising approach for materials that are problematic in MBE fabrication and has been already utilized for heat conduction investigations by Grimm et al., which aimed for improvement of the thermoelectric figure of merit [Gri14].

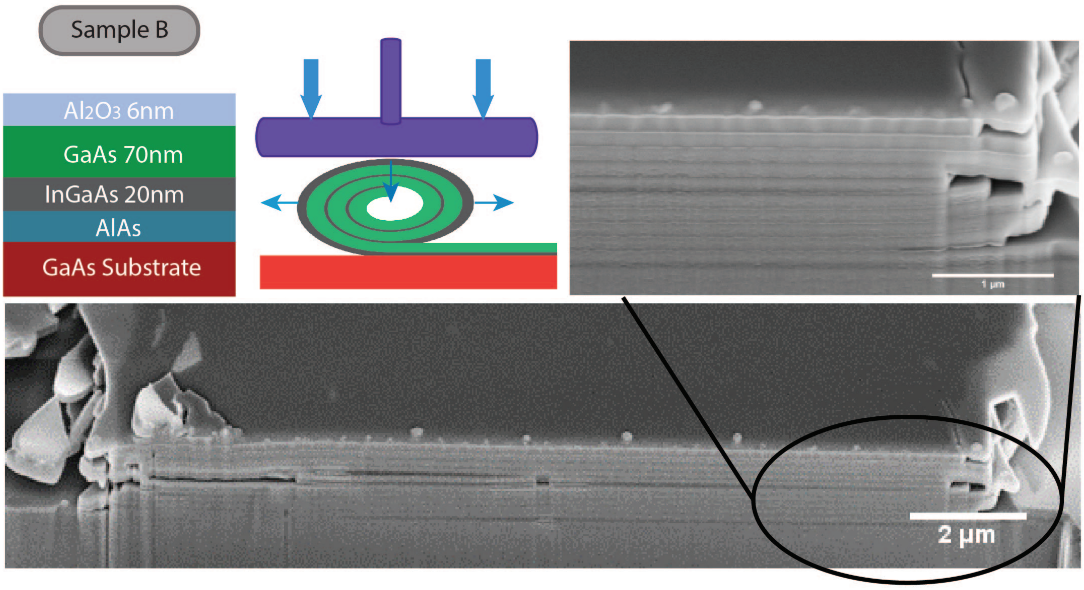

Figure 4.17.: Rolled-up multilayer tubes can be pressed mechanically to form a planar superlattice. Left top part: Sample structure. Middle top part: Principle of the fabrication process. Bottom part: SEM image with a FIB cut of the pressed sample B, showing a zoomed in part in the top right figure. The SEM images were obtained from collaborators from the IFW Dresden.

For the investigation of these kind of samples the same layer stack as for sample B was used. As a reminder, the sample structure of B is shown again in the top left part of Figure 4.17. The SEM image in Figure 4.17 shows a FIB cut of a pressed superlattice with 10 repetitions of the bilayer and a schematic of the fabrication process of the

nanoimprinting.
This fabrication method raises the question if the applied pressure can indeed produce well-adhered layers, which should manifest themselves in a characteristic superlattice acoustic mode spectrum. Thus, direct access to the multilayer quality is possible.
While some small regions seem to be neatly ordered, defects can already be seen on most parts of the pressed superlattice in the SEM image of the sample in Figure 4.17.

Figure 4.18 reveals the peak frequencies of the frequency spectra of different measurements of the pressed sample B (black). A grouping of the frequencies can be observed, similar to the results of the rolled sample A_r, which were already presented in Figure 4.11. No superlattice characteristics can be observed. For a comparison, the frequency modes of sample A_r that showed the expected modes of a superlattice (given in Figure 4.9 (a)) are indicated by the green vertical lines in Figure 4.18.

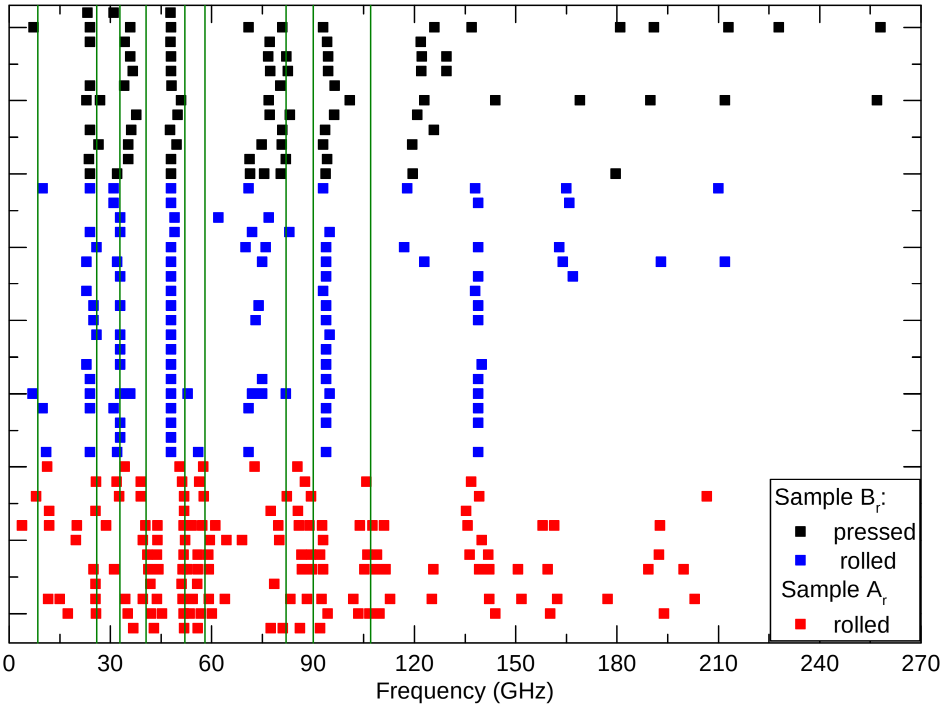

Figure 4.18.: Peak frequencies of frequency spectra of different measurements of the pressed sample B_r (black squares), rolled sample B_r (blue squares) and rolled sample A_r (red squares). Each row exhibits the frequencies of one measurement. The light green vertical lines indicate the position of the superlattice mode of sample A_r, which was discussed earlier.

Modes with features of an oscillating bilayer are also observed in this pressed configuration. The contact between the neighbouring windings is apparently weak. The procedure of pressing does not seem to considerable enhance the adhesion.
Besides the appearing oscillating bilayer behaviour, there are differences to the results

obtained from the rolled-up and planar MBE grown samples, which were presented earlier. For an easier comparison, parts of the data of the rolled-up and planar MBE grown samples are presented in Figure 4.18, together with the data of the pressed sample. The frequency peak positions of the pressed samples, the rolled-up sample B_r and to the rolled-up sample A_r are presented in black, blue and red, respectively. Differences become visible and will be addressed in the following.

The first look at the peak positions might be misleading: while the frequency modes seem to become more orderly for the samples B_r with Al_2O_3, they are in fact only much noisier and the amplitudes decrease dramatically compared to the measurements on sample A_r without Al_2O_3. This can be seen more clearly when comparing the frequency spectra of the different samples in Figure 4.19.

One would expect the pressed sample B to yield a better adhesion than the rolled-up sample B_r and therefore the modes to be similar to the calculated ones. However, the obtained modes do not show modes of a superlattice. The quality of the adhesion does not seem to be improved.

There are several possible explanations of this behaviour. As shown in the SEM images of Figure 4.17, defects appear in the pressed samples in the form of air gaps between the individual bilayers. These air gaps, which appear at different positions on the bilayers of the pressed tubes, limit the number of adhered layers. The pressing procedure does not seem to sustainably increase the adhesion between the windings in comparison to the rolled-up tubes.

The results for the pressed sample B_r are hence similar to the rolled-up sample B_r. The lack of the appearance of superlattice modes or modes of several connected windings might be due to difficulties in the detection, generation or the damping of the modes. For sample B_r, an explanation of the disappearance of the modes was given above by cavity effects of the large air gap in the center of the tubes. However, this effect can be excluded here, as the air gap was removed by pressing the sample. Although there are no air gaps left at the micrometer scale, there might be nanometer sized air gaps remaining at some spots of the samples.

Strong damping effects can also be excluded when comparing the oscillations given in Figure 4.19. The oscillations last for almost the whole time window during which the dominant part is given by the Brillouin oscillation.

Furthermore, the generation process does not seem to be a reason for the change of the detected modes: as a thin Al_2O_3 layer is almost transparent at 820 nm, the generation should not change notably compared to sample A.

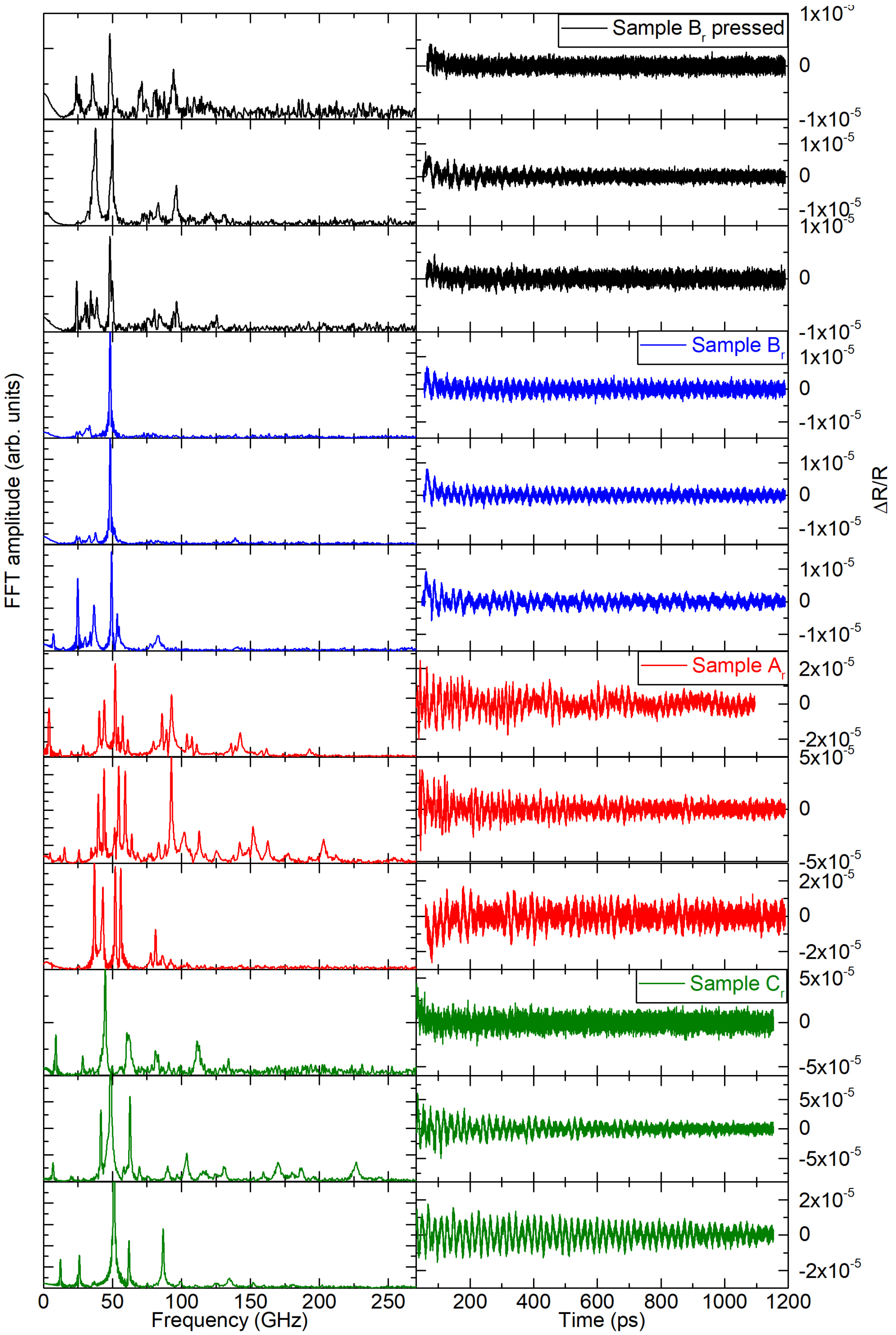

Figure 4.19.: Comparison of FFTs and extracted oscillations of the time-resolved reflectivity change of the pressed sample B_r (black), sample B_r (blue), sample A_r (red) and sample C_r (green).

In the current state, a qualitative characterization of the pressed microtubes is possible. A quantitative description will require a more detailed investigation of a high-quality sample that can act as a benchmark to test the theoretical calculations against well-known structural parameters in the rolled and pressed forms. Therefore, accurately defined samples with very good adhesion – all with the same layer sequence – would be required to successively change these parameters. Samples with a single winding up to five or more windings would be needed and measurements of the rolled-up tube followed by measurements after the same tube was pressed – then planar – would be required.

Rolled-up Multilayer Tubes with AlAs – Sample C

In sample C_r, in order to suppress side-rolling effects during the roll-up process of the multilayer tubes AlAs is used instead of Al_2O_3. The shape of sample C is also a rolled-up multilayer tube (as shown in Figure 4.1 (a)).

The frequencies obtained by the evaluation of the measurements show again a wide variety, hinting to inhomogeneous interfaces as can be seen in Figure 4.19. Modes up to 350 GHz can be observed.

The results are also ambiguous and a similar behaviour as in the measurements of sample B arises. Thus, the exchange of the Al_2O_3 by the AlAs does not improve the internal structural quality of the tubes. It is necessary to investigate more accurately defined samples.

4.3. Conclusion

In conclusion, a detailed experimental and theoretical study of the acoustic phonon modes in rolled-up multilayer tubes consisting of the materials $\mathrm{In_{0.2}Ga_{0.8}As}$, GaAs, $\mathrm{Al_2O_3}$ and AlAs was presented.

The MBE grown planar multilayers $\mathrm{A_p}$ and $\mathrm{B_p}$ were excited optically and the detected coherent acoustic phonon modes were analysed. The modes of the MBE grown 5 bilayer structure of sample $\mathrm{A_{5MBE}}$ exhibit the properties of a back-folded acoustic phonon dispersion relation of a superlattice. Calculations with the Rytov model are in good agreement with the experimental results. Some modes are close to the ones of the rolled-up multilayers of sample $\mathrm{A_r}$ but there is no triplet structure visible anymore. While some modes correspond to those obtained from the Rytov model, additional modes appear, which can be explained by weak adhesion.

Comparing sample $\mathrm{A_r}$ to the experimentally obtained results of the layer system of the rolled-up superlattice $\mathrm{B_r}$, intriguing differences are detected. Here, the Rytov model cannot account for the obtained features which can be attributed to imperfect adhesion between the individual windings of the tubes. A good qualitative agreement between a modeling approach based on transfer matrices including a massless spring that accounts for the interface adhesion and the observed eigenmode spectra was found for both sample $\mathrm{A_r}$ and $\mathrm{B_r}$. A spring constant was found of $k = 5 \cdot 10^9\,\mathrm{N\,m^{-1}}$ in this case, which is several orders of magnitude smaller than typical metal/semiconductor contacts. This enables to distinguish areas with varying interface adhesion between the windings on individual tubes. Areas with sufficient interface adhesion to couple the individual tube windings, as well as completely decoupled layers, are observed.

A more complicated case arises when the interface adhesion only couples some of the tube windings. These areas can be clearly identified. However, a detailed modeling is hindered due to the number of free parameters. Furthermore, the tubes of sample $\mathrm{B_r}$ exhibit areas where the detected signal amplitudes decrease drastically. A possible explanation is the radius dependent detection sensitivity of the coherent phonons. The upper and lower part of the tube resemble an optical cavity with strongly varying cavity spacing.

In addition to the planar and tubular geometries of sample A, a spiral shaped single winding has been also investigated. Due to the twist of the bilayer, it can be measured from both sides. In this geometry, the upper spiral part is freestanding while the lower part is in contact with the substrate. Interestingly both parts exhibit almost identical mode spectra which hints to a very weak spiral-substrate contact and no strong adhesion is present.

Another variation of the samples forming planar superlattices was analyzed. They were produced by mechanically pressing rolled-up tubes to the surface. The eigenmodes were found not to change considerably compared to those of the rolled-up samples. An important point regarding applications for e.g. thermal transport is the observation that, despite the applied pressure, the individual windings are still only weakly or partially coupled. This is evident by the lack of superlattice characteristica in the mode spectra. A correlation to SEM images indeed reveals the presence of submicron gaps.

The presented findings pose an important step towards the characterization of mechanical interface adhesion in nanoscaled systems. In particular, the microtubes investigated herein are a well-suited system to study the mechanical coupling in multilayer systems with increasing complexity depending on the number of windings.
For a more quantitative analysis of these multilayer tubes samples are needed, which exhibit more homogeneous interfaces of the individual windings. This could be achieved by thermal annealing of the samples under mechanical pressure. A reproducible strong adhesion between the layers is important to explicitly characterize an increasing number of connected windings.

These results are not only of general interest for all nanoscaled systems based on multilayer structures but are also crucial with respect to the possible application of the studied microtubes in various fields in nanotechnology. A possible application of the microtubes is nanoacoustics in biology for single cell dynamic imaging. Xi et al. showed that single cells can be encapsulated into the confined environment of a rolled-up microtube [Xi14]. Cell structures were already mapped by ultrasonic measurements by Dehoux et al. [Deh15]. Combining both and detecting cell dynamics non-invasivly from any side of the microtube using ASOPS is thought to be possible.
Besides the use in nanobiology there are numerous further fields as e.g. microtube lasers, nanophotonics and thermoelectric devices, where the structural homogeneity is crucial for reliable applications.

CHAPTER 5

Picosecond Photoacoustic Metrology of Silicon Dioxide on Silicon and Lithium Niobate Layer Systems

Thin films with submicron down to nanometer thickness play a fundamental role in a wide range of applications. Applications range from anti-reflection coatings [Rau11], filters [Sav10], stretchable electronics [Rog10] to thin film transistors [Par12]. Thin film technology forms the core of the current semiconductor industries.
One important area in the semiconductor industry is the fabrication and development of electro-acoustic filters [Sav10, Tad09], which are often used in modem devices e.g. in modern mobile phones. A large number of small size, high performance filters is needed as they enable mobile phones to receive and transmit a broad range of frequencies [Pen11]. The most commonly used technology for these filters is based on surface-acoustic-waves and bulk-acoustic-waves.

Ferroelectric thin films are applied in microsystems, high frequency electronics and alternative memories based on ferroelectric materials [Set06]. Adding ferroelectric films opens the possibility to include sensing and actuating functionalities to microelectromechanical systems (MEMS) [Set06].
An example of a ferroelectric, birefringent material that is used in numerous optical and acoustic applications is lithium niobate ($LiNbO_3$) [San10]. Since the 1990s it has been employed in surface-acoustic-wave (SAW) filters for radio frequency (RF) filtering functions in mobile phones [Lam16]. In combination with silicon dioxide (SiO_2) they form a system most commonly utilized in temperature-compensated SAW filters [Rup02]. SAWs have a range of applications also outside mobile phones and are used e.g. in other telecommunications, touch screens, microfluidics and a variety of sensors [Che15, Dra01].

SiO_2 was chosen as thin film material in filters as it was the only material with the ability to support different timing and filtering functions in mobile phones for a long time

[Lam16]. This is possible due to its intrinsic high quality factor Q, i.e. a low dissipation of SAWs, and high temperature stability. The Q factor is responsible for the timing accuracy. Additionally, less power is needed to sustain vibrations for a higher Q as the damping rate is $\propto 1/Q$.

Many applications of thin films require exact knowledge of film thicknesses in the nanometre range as well as their respective sound velocities, which depend on the strain inside the films amongst other parameters. In the following, an approach to measure both quantities simultaneously by means of time-resolved photoacoustic spectroscopy in thin SiO_2 films will be presented. This method has already been employed for measurements in similar systems, however without birefringent layers [Man08]. Here, it is shown additionally that the polarization dependent detection sensitivity in $LiNbO_3$ can be utilized to reveal information about the $LiNbO_3$ crystal orientation and the layer interface [Mou08, Pez06, Mou07]. Furthermore, this approach has the potential to be applied in metrology of other complex layer systems based on, e.g., birefringent polymers [Web00], nanocomposites [RE08] or indium tin oxide (ITO)-based devices [Har08] . Additionally, recently emerging materials, such as nanowire based assemblies [Mus06, Kün01] exhibiting strong birefringence, could be interesting to study from a more fundamental research point of view.
In the following parts of this chapter, two different devices will be investigated. They consist of a thin silicon dioxide layer which is placed on two different substrates, silicon and lithium niobate. The devices discussed in this chapter were provided by an industry collaboration.

5.1. Silicon Dioxide on Silicon Substrate

5.1.1. Sample Structure

First, the sample consisting of silicon dioxide on a silicon substrate will be analyzed. From top to bottom the sample consists of: A chromium layer of $d_{\mathrm{Cr}} = 18\,\mathrm{nm}$, which was deposited on the original device structure by thermal evaporation additionally. It is used as an opto-acoustic transducer to enhance the photo-acoustic signal. Then a layer of SiO_2 with $d_{\mathrm{SiO}_2} = 1143\,\mathrm{nm}$, which was prepared using reactive DC-pulsed magnetron sputtering (EVATEC CLUSTERLINE® 200 II) in addition to applying radio frequency (RF-) bias on the substrate holder. The silicon substrate has a thickness of 575 µm.
In the inset of Figure 5.1 the sample structure is depicted. The layers are not to scale.

Opto-acoustic transducer
In the case of weak light absorption in the investigated material, as it is the case for SiO_2, an opto-acoustic transducer is required in order to excite the sample. The opto-acoustic transducer consists of a thin metal layer deposited on the sample to enable the excitation of a strain pulse in the material of interest. In this metal layer the acoustic phonons will be mainly excited by thermoelasticity. Here, a thin chromium (Cr) layer is used as an opto-acoustic transducer. Similarly, an opto-acoustic transducer in form of a Cr layer will be used in Chapter 6 but in a different sample configuration. Cr is chosen because the electron-phonon coupling constant is high and therefore generates a coherent strain over a distance of the order of the optical absorption length [Tse06]. Additionally Cr is used as it forms strong bonds with oxide surfaces due to its oxidative nature [Moa13]. When the layer is placed on top of the sample its thickness needs to be chosen carefully. The layer needs to be thick enough to efficiently excite acoustic phonons but also not too thick as it is otherwise not transparent enough anymore to detect the dynamics inside the sample. In some cases a possibility to circumvent this problem is to place the transducer on the backside of the sample.

5.1.2. Experimental Results

A short laser pulse excites the sample from the side of the Cr film. Figure 5.1 shows a typical time-resolved reflectivity change obtained from this sample. It is possible to observe strongly that the fast electronic excitation of the Cr film yields a large change in the reflectivity $\Delta R/R$ of the order 10^{-4} during the first few tens of picoseconds [Sai03, Rue15, Fuj84]. Hot electrons are excited inside the opto-acoustic metal transducer by the short laser pulse. The electrons transfer their energy to the lattice via electron-phonon interaction. This process gives rise to an impulsive strain pulse in the Cr film, which propagates at the respective longitudinal speed of sound through the layer structure.

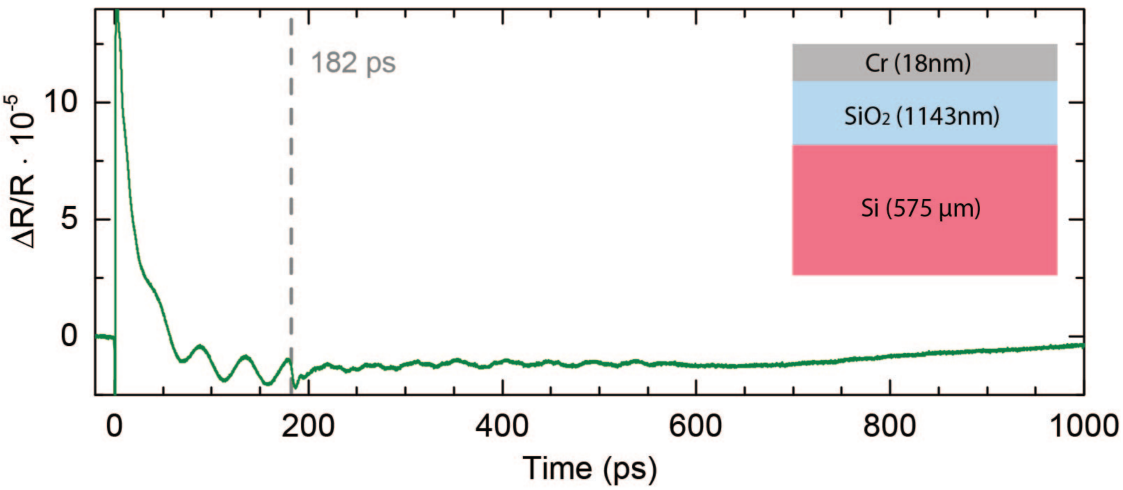

Figure 5.1.: Time-resolved reflectivity change of the silicon dioxide on silicon sample. The grey vertical line marks the abrupt change in the oscillatory behaviour appearing at 182 ps when the strain pulse is reflected at the interface to the Si substrate. The inset shows the schematic sample structure. The layers are not to scale.

The propagating strain pulse is monitored through the semi-transparent Cr film. The absorption coefficient of chromium at a wavelength of 820 nm is $\alpha = 5.33 \cdot 10^5\,\mathrm{cm}^{-1}$ [Joh74] and hence the optical penetration depth is $\sigma = 1/\alpha = 18.8\,\mathrm{nm}$. Partially reflected probe light from the strain pulse is the origin of the associated change in the refractive index. This light interferes with the light reflected at the top of the sample giving rise to time-resolved Brillouin oscillations with frequencies corresponding to the speed of sound in the material and the refractive index [Dev15]. Brillouin oscillations and in general the generation and detection processes are discussed in detail in Chapter 2.

The oscillatory part of the signal during the first 182 ps is dominated by the signal from the SiO_2 layer. After the strain pulse propagates through the SiO_2, it is reflected back at the interface to the Si layer, which can be observed as a pronounced change in the oscillatory behaviour in the transient after (182 ± 5) ps, as indicated by the gray vertical line in Figure 5.1. From this point on, both the SiO_2 and the Si layer contribute to the detected signal, which consists of time-resolved Brillouin oscillations from both layers as will be shown below. The exponentially decaying components of the background signal mainly originate from electron-phonon scattering and thermal diffusion in the Cr layer, respectively [Sai03, Rue15, Fuj84]. For details on the transients in general see Chapter 3.4 where an exemplary measurement is discussed.

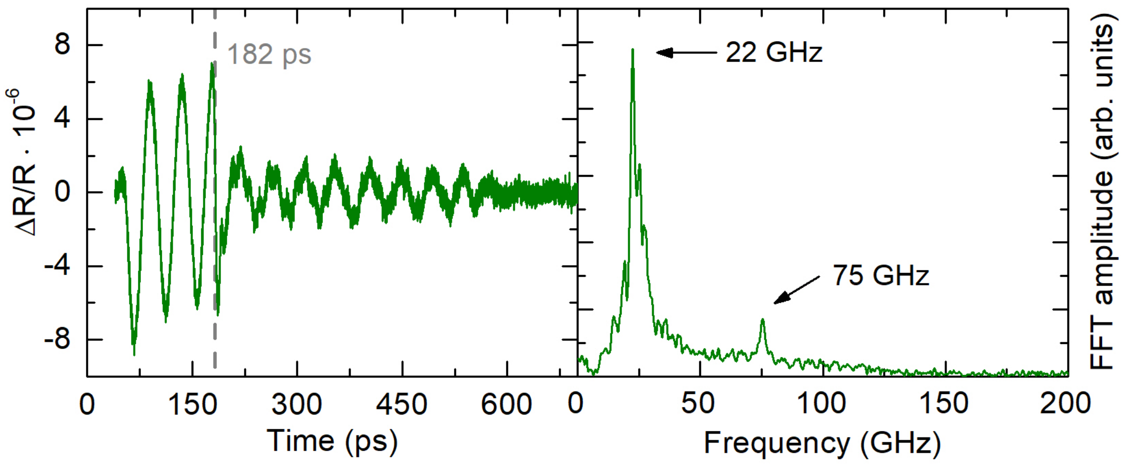

Figure 5.2.: Time-resolved reflectivity change with subtracted electronic background and respective FFT. Again, the change in the oscillatory behaviour is marked with a gray vertical line. The obtained frequencies are at 22 GHz and 75 GHz as indicated.

In Figure 5.2, the extracted time-resolved reflectivity change of the transient of Figure 5.1 without the electronic background is depicted together with the respective FFT. The frequency shift of the peaks of the individual signal sections compared to the FFT obtained over the full time window is negligible. Thus, the FFT is presented for the full measurement range of the time-domain of 1.25 ns.
In the time domain signal it is now possible to see the two parts of the signal more clearly, with the pronounced change in the oscillatory behaviour at 182 ps. This point indicates the time delay, when the acoustic pulse is reflected at the interface to the Si layer. Two frequencies can be observed in the FFT at $f_1 = 22\,\text{GHz}$ and $f_2 = 75\,\text{GHz}$.
From the beginning of the signal the frequency of $f_1 = 22\,\text{GHz}$ is present, which can be assigned to the Brillouin frequency of SiO_2. Using this measured Brillouin frequency, the longitudinal sound velocity for SiO_2 can be calculated to be $v_{\text{SiO}_2} = \lambda f / 2n = 6207\,\text{m}\,\text{s}^{-1}$, using $n = 1.45$ [Mal65].
The thickness of the SiO_2 layer can then be calculated to be $d = t v_{\text{SiO}_2} = 1129\,\text{nm}$ using the obtained sound velocity v_{SiO_2} and the time $t = 182\,\text{ps}$ of the change in the oscillatory behaviour. The thickness is in good agreement with the nominal value of $d = 1143\,\text{nm}$ provided by the grower (EVATEC AG, SWITZERLAND). In only one measurement, both the sound velocity and the thickness of a sample can be determined simultaneously.

The second frequency obtained from this measurement is $f_2 = 75\,\text{GHz}$, which appears from 182 ps onwards. It originates from the Brillouin oscillation of the Si layer. It can be used to calculate the longitudinal sound velocity $v_{\text{Si}} = 8412\,\text{m}\,\text{s}^{-1}$, with the refractive index $n = 3.68$ (see Appendix B for an overview of the material parameters). This value is in good agreement with the literature value for the longitudinal sound velocity of Si along the [100] direction of $v_{\mathrm{Si}} = 8430\,\mathrm{m\,s^{-1}}$ [Ins].

5.2. Silicon Dioxide on Lithium Niobate Substrate

5.2.1. Sample Structure

In the following, a sample similar to the one discussed in the previous section will be investigated. However, in this case the SiO_2 layer is grown on a $LiNbO_3$ substrate instead of Si.

The layer structure is depicted in Figure 5.3, consisting of four different layers which, from top to bottom, are Cr, SiO_2, $LiNbO_3$, and Al. The chromium layer of 18 nm was deposited by thermal evaporation and is used again as opto-acoustic transducer. The amorphous silicon dioxide layer has a thickness of 1140 nm. The crystalline lithium niobate has a thickness of 325 µm. A thermally evaporated aluminium layer of 100 nm forms the backside, which is needed for subsequent lithography steps in industrial applications.

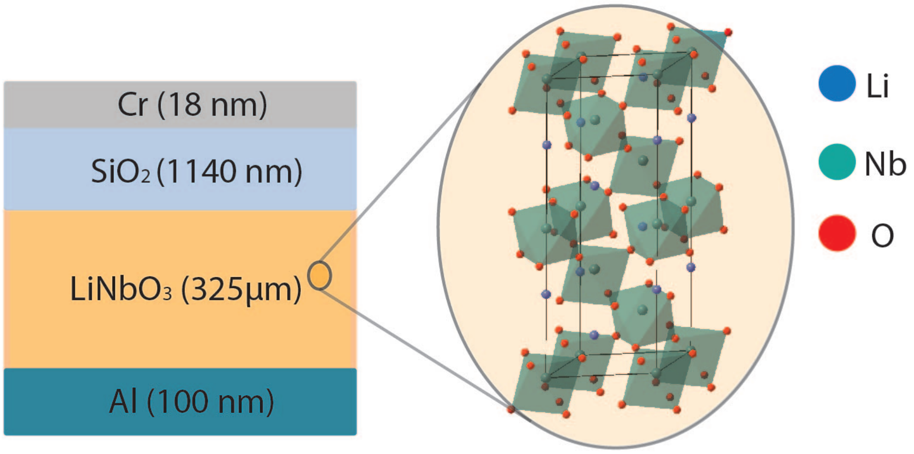

Figure 5.3.: Scheme of sample structure consisting from top to bottom of the following four layers: 18 nm Cr, 1140 nm SiO_2, 325 µm $LiNbO_3$ and 100 nm Al. The layers are not to scale. The trigonal crystal structure of $LiNbO_3$ is indicated on the right side.

Lithium niobate is an optically anisotropic material and thus exhibits birefringence. In addition, the optical absorption in the wavelength regime used, i.e. around 790 nm - 820 nm, is negligible [Xia04], since $LiNbO_3$ is transparent in the visible light regime. The corresponding trigonal crystal structure is displayed on the right part of Figure 5.3. The crystal structure is trigonal and uniaxial.

Light, which enters a birefringent material, is split into two beams that are polarized at a right angle to each other: an "ordinary" wave and an "extraordinary" wave. The waves are perpendicular to the optical path. In general it holds $n_o = n_x = n_y \neq n_z$ for the ordinary index of uniaxial crystals, and $n_e = n_z$ for the extraordinary index. The equation for the refractive index of uniaxial crystals is:

$$\frac{x^2 + y^2}{n_o^2} + \frac{z^2}{n_e^2} = 1. \tag{5.1}$$

From this equation one can see that the optical properties of a crystal are described by the refractive index ellipsoid, also called the optical indicatrix.

For a uniaxial crystal, the index ellipsoid reduces to an index of revolution. For an isotropic medium it becomes a sphere.

The vibration directions cut through the indicatrix, resulting in a plane with an elliptical cross section. The directions of vibration correspond to the mayor and minor axes of this ellipse. This refractive index ellipsoid is shown schematically in Figure 5.4.

For LiNbO$_3$, $n_o = 2.25 > 2.17 = n_e$, and it therefore belongs to the class of negative uniaxial crystals. Polarized light incident under an angle to the axes can be seen as the sum of the normal modes. Hence, each mode will have a different phase velocity.

While the ordinary part of the refractive index has a fixed value n_o, independent of the crystal orientation, the extraordinary part of the refractive index $n_e(\theta)$ for a propagation in a general direction is given by

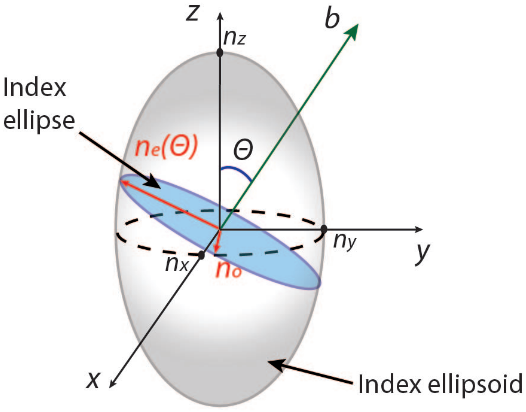

Figure 5.4.: Optical indicatrix: Refractive index ellipsoid of a uniaxial crystal used to determine the polarizations and refractive indexes of the normal modes of a wave traveling in the direction of b. The blue plane, the index ellipse, is perpendicular to b. $n_e(\theta)$ and n_o are the major and minor axes of the index ellipse. The figure was taken and adapted from [Sal07].

$$n_e(\theta) = \frac{n_o n_e}{\sqrt{n_o^2 \sin^2\theta + n_e^2 \cos^2\theta}} \tag{5.2}$$

where $n_e(\theta)$ varies between the values of n_o for $\theta = 0°$ and n_e for $\theta = 90°$. θ is the angle between the new orientation of the crystal and the optical axis as shown in Figure 5.4

[Sal07].

In uniaxial birefringent materials like lithium niobate, the Brillouin scattering process becomes much intricate due to the fact that photons do not propagate with the same velocity depending on their – ordinary or extraordinary – polarization [Lej16]. Birefringence therefore leads to a splitting of the Brillouin modes in up to four modes [Gre70]. Stimulated birefringence is utilized in several acousto-optic devices and allows light mode conversion between ordinary and extraordinary light waves. This is possible in several ferroelectric materials due to their photoelastic constants, which are larger than in other materials [Lej16].

In dependence of the crystal orientation, the respective sound velocity can be calculated. The Christoffel equation can be solved to calculate the phase velocities of three different wave modes that exist in an anisotropic solid. After solving the determinant of the Christoffel matrix, the longitudinal sound velocity can be calculated with:

$$v_l = \sqrt{\frac{c_{33}}{\rho}} \tag{5.3}$$

5.2.2. Experimental Results

Experiments without metal transducer

The sample is composed of the three layers SiO_2, $LiNbO_3$ and Al, as indicated in the schematic of the structure shown in Figure 5.5 (a).

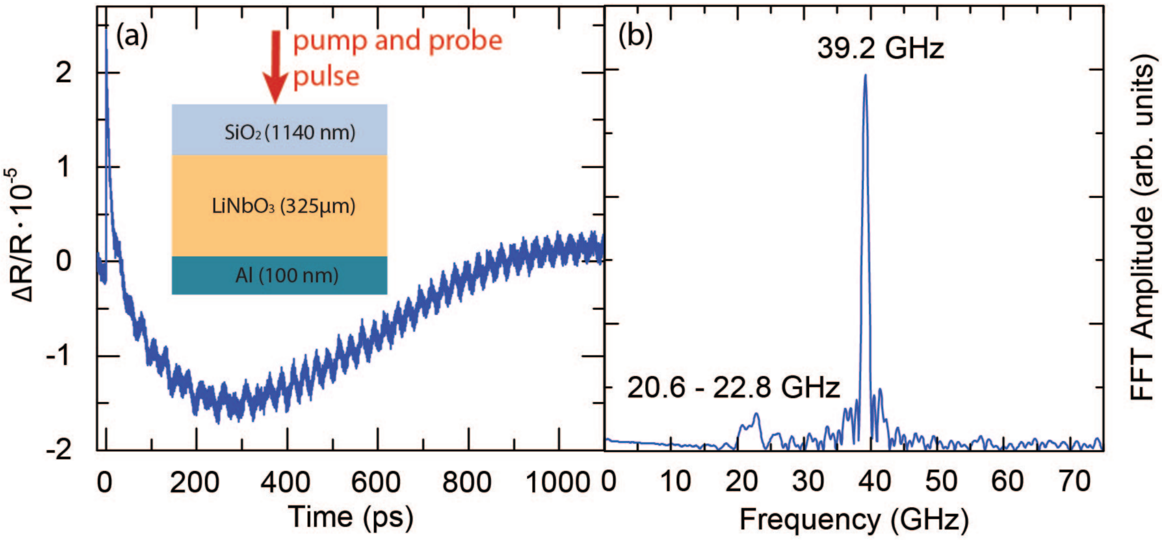

Figure 5.5.: (a) Time-resolved reflectivity change and (b) FFT of the $SiO_2/LiNbO_3$ sample without an opto-acoustic chromium transducer. The features of the structure, which will be discussed in detail in the following part, are already visible but extremely noisy. The sample structure is indicated in (a).

First the sample was investigated in this form. The results obtained in this configuration are also presented in Figure 5.5. Figure 5.5 (a) shows the time-resolved reflectivity change obtained after the optical excitation from the SiO_2 side along with the sample structure. Figure 5.5 (b) exhibits the corresponding FFT. Frequencies are detected between 20 and 23 GHz and at 39 GHz. The expected Brillouin frequencies would be at $f = \frac{2vn}{\lambda} = 20.5\,\text{GHz}$ and 35.9 GHz for SiO_2 and $LiNbO_3$, respectively.

As both SiO_2 and $LiNbO_3$ are almost transparent at a wavelength of 800 nm [Gao13, Xia04], no strain pulse is generated close to the surface, but the pulse is absorbed over a long distance. A strain pulse could theoretically be generated at the Al layer at the back, but this strain pulse needs to travel through the whole sample and attenuates strongly before it reaches the SiO_2 layer. In addition, and more importantly, the time it would need to travel through the sample is longer than 1.25 ns, which is the measurement time window of the setup used. The measurement is noisy and the frequency, which can be detected around 22 GHz, is visible but not distinct and almost vanishes in the noise.

To ameliorate the signal significantly and to enable the investigation of the interface of the SiO_2 and $LiNbO_3$ layer, an opto-acoustic metal transducer in form of a Cr layer was used as in the case of the previous sample with the Si substrate.

Experiments with metal transducer

The main part of the following results of the silicon dioxide on lithium niobate sample was published in Brick et al. [Bri17a].
In Figure 5.6, a typical transient of the reflectivity change after the optical excitation is shown. The excitation process is similar to the one described above for the silicon dioxide on silicon sample and can be found in detail in Chapter 2.5. The strong change in $\Delta R/R$ during the first picoseconds due to the fast excitation of electron-hole pairs followed by the slowly decaying electronic and thermal background can be seen.

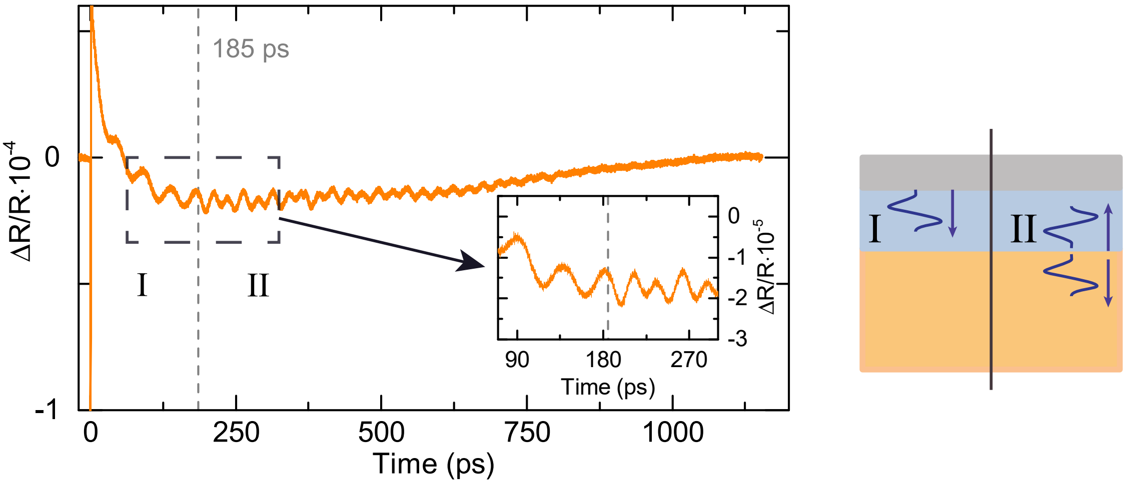

Figure 5.6.: Time-resolved reflectivity change of the $SiO_2/LiNbO_3$ sample. Two regimes are visible: regime I before 185 ps (marked with a vertical line in the data) where the signal stems from SiO_2 and regime II after 185 ps with a signal consisting of the interfering signal from SiO_2 and $LiNbO_3$. The origin of the regimes are shown in the right part.

Again, it is possible to classify two regimes, which are sketched in Figure 5.6.
The first part of the oscillation, regime I, is dominated by the signal from the SiO_2 layer. As the traveling strain pulse is still inside the SiO_2 layer, light is reflected at it and Brillouin oscillations of this layer can be detected. After propagating through the SiO_2, the pulse reaches the interface to the $LiNbO_3$ layer. One part of the pulse is reflected back into the SiO_2 layer, while the other part of the pulse continues inside the $LiNbO_3$ layer. This can be vaguely observed as a change in the oscillatory behaviour in the transient at 185 ps. From this point on, in regime II, both SiO_2 and $LiNbO_3$ contribute to the signal of the transient, which is a superposition of both of their time-resolved Brillouin oscillations.
Contrary to the SiO_2 on silicon sample, the change in the oscillatory behaviour is less

pronounced due to the fact that the acoustic impedances of the two layers are similar. The amplitude of the acoustic reflectivity at the interface can be calculated to be

$$r_{1/2} = \frac{Z_2 - Z_1}{Z_2 + Z_1} \tag{5.4}$$

for the first system it yields: $r_{\mathrm{SiO_2/Si}} = \frac{Z_{\mathrm{Si}} - Z_{\mathrm{SiO_2}}}{Z_{\mathrm{Si}} + Z_{\mathrm{SiO_2}}} = 0.12$ with the densities $\rho_{\mathrm{SiO_2}} = 2.65\,\mathrm{g/cm^3}$ and $\rho_{\mathrm{Si}} = 2.33\,\mathrm{g/cm^3}$ and the longitudinal acoustic sound velocities $v_{\mathrm{SiO_2}} = 5800\,\mathrm{m\,s^{-1}}$ and $v_{\mathrm{Si}} = 8433\,\mathrm{m\,s^{-1}}$. For the system with $\mathrm{LiNbO_3}$ it is $r_{\mathrm{SiO_2/LiNbO_3}} = 0.36$ with the density $\rho_{\mathrm{LiNbO_3}} = 4.64\,\mathrm{g/cm^3}$ and the longitudinal acoustic sound velocities $v_{\mathrm{LiNbO_3}} = 7090\,\mathrm{m\,s^{-1}}$. $r_{\mathrm{SiO_2/Si}} < r_{\mathrm{SiO_2/LiNbO_3}}$, which means that in the first case a smaller part is reflected back and hence the difference of the visible oscillation is larger than in the second case.

Figure 5.7 (a) shows the extracted oscillations without the electronic background from the transient of Figure 5.6. The fast and slow decaying components of the background signal, which were extracted for the further analysis, mainly stem from electron-phonon scattering and thermal diffusion in the Cr layer, respectively [Sai03, Rue15, Fuj84]. As mentioned before, for details on the analysis of the transient see Chapter 3.4.
In Figure 5.7 (c), the FFT of the extracted signal of Figure 5.7 (a) is shown. Again, the FFT is presented for the full measurement range of the time-domain because the frequency shift of the peaks of the individual signal sections compared to the FFT obtained over the full time window is negligible.
The peak at 20.5 GHz originates from the Brillouin oscillation in $\mathrm{SiO_2}$ and the one at 38.9 GHz from the Brillouin oscillation in $\mathrm{LiNbO_3}$. This allows the calculation of the longitudinal sound velocities v in the respective media by using the Brillouin frequencies, which are given by $f = 2nv/\lambda$, with the refractive index n of the respective media and the wavelength of the probe light λ.
For $\mathrm{SiO_2}$, again $n = 1.45$ [Mal65] was used and a longitudinal sound velocity of $v = 5784\,\mathrm{m\,s^{-1}}$ with an error of $\pm 141\,\mathrm{m\,s^{-1}}$ can be obtained. The literature value of $5800\,\mathrm{m\,s^{-1}}$ [Naz05] is well within the measurement error. The uncertainty of the sound velocity takes into account that there is a measurement inaccuracy for the frequency of ± 0.5 GHz. This approach is, however, more complicated in $\mathrm{LiNbO_3}$ as will be discussed in the following.
For the Al layer, no contribution can be observed in the measurements. The thin layer would be observable as a thickness oscillation, which would yield a mode at $f = (2n-1)v/4d = 16$ GHz for $n = 1$, with the longitudinal sound velocity of Al of $v = 6320\,\mathrm{m\,s^{-1}}$ [Che89] and the thickness $d = 100$ nm of the Al layer. In the obtained FFTs there is no evidence of this as there is no peak at 16 GHz. The signal in general is small for this sample and the attenuation is probably too high for obtaining a signal from the back of the sample.

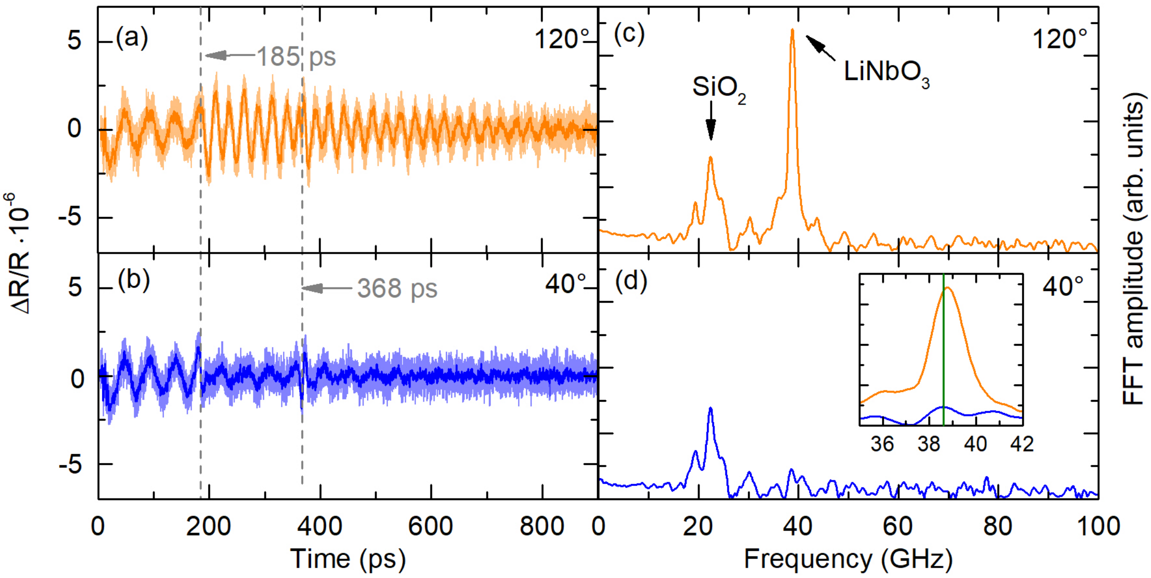

Figure 5.7.: (a), (b) extracted time-resolved reflectivity change for different polarization angles. The vertical dotted lines mark the discontinuities in the signal where the traveling acoustic pulse reaches the interface of SiO_2/$LiNbO_3$. (c), (d) respective FFTs. In the orange graphs the superimposed response of $LiNbO_3$ and SiO_2 can be seen (data from the rotation angle of 120° of Figure 5.8). In the blue graphs, the part stemming from $LiNbO_3$ is "turned off" (data from the rotation angle of 40° of Figure 5.8). The inset in (d) shows the shift of the $LiNbO_3$ frequency for the FFT at 120° and 40°. The green line is a guide to the eye to enable better visibility of the occuring frequency shift.

As already mentioned above, recent findings show that the birefringence in $LiNbO_3$ leads to a splitting into ordinary and extraordinary waves. This process hence can give rise to several Brillouin modes, which show a distinct dependence on the crystal orientation and the incident probe light polarization as shown by Lejman et al. [Lej16]. Lejman et al. demonstrate in their work the ultrafast acousto-optic mode conversion induced by coherent acoustic phonons in $LiNbO_3$. In particular, they observe a strong polarization dependence of the observed Brillouin mode amplitudes caused by different photoelastic constants for respective polarization orientations.

X-ray measurements revealed for the $LiNbO_3$ layer a crystal orientation of $(\bar{1}14)$, which results in a tilt of the crystal of 6.1° against the Z-axis. This yields for the refractive indices $n_o = 2.250$ and $n_e = 2.249$, i.e. almost identical values, for the negative birefringent crystal. Thus, for the measured frequency of $f = 38.9\,\mathrm{GHz}$ in $LiNbO_3$, a sound velocity of $v = (7090 \pm 90)\,\mathrm{m\,s^{-1}}$ is obtained. Using the Christoffel equation (details on the Christoffel equation can be found in [Aul73]), the sound velocities in $LiNbO_3$ can be estimated to be along the $(\bar{1}14)$ direction for the quasi-longitudinal mode $v_l = 7245\,\mathrm{m\,s^{-1}}$, and for the two quasi-transverse modes $v_{t1} = 3662\,\mathrm{m\,s^{-1}}$ and $v_{t2} = 3540\,\mathrm{m\,s^{-1}}$. The calculated longitudinal value agrees well with the measured one. In order to check for the possibility of a signal contribution from the transverse components, the expected Brillouin frequency of $f \approx 20\,\mathrm{GHz}$ can be calculated. Indeed, an additional mode close to this frequency can be observed in the FFT spectrum displayed in Figure 5.7. However, an unambiguous assignment is not possible due to the overlap with the SiO_2 mode. In the following, it will be shown how the polarization dependent signal detection of the quasi-longitudinal mode can be utilized in the measurements.

Figure 5.7 (b) and 5.7 (d) depict the extracted time-resolved reflectivity change and the respective FFT of a measurement of the sample with variation of the probe pulse polarization. For the two measurements, the polarization is roughly perpendicular (with 40° instead of 120°, the 0° polarization angle was chosen arbitrarily).

While there is a strong contribution from the $LiNbO_3$ layer to the time domain signal in Figure 5.7 (a), a change in the probe pulse polarization can almost completely suppress the contribution of $LiNbO_3$ as evidenced by the signal in (b). In the corresponding FFTs, the respective contributions of SiO_2 and $LiNbO_3$ are marked. In (d) only the contribution of SiO_2 is left.

This behaviour contains different types of information, which can be exploited. If only the contributions from SiO_2 are detected as in Figure 5.7 (d), the discontinuities caused by the acoustic pulse while propagating through the SiO_2/ $LiNbO_3$ interface and the arrival at the sample surface can be clearly identified. This allows acquisition of the time of flight $t = 185\,\mathrm{ps}$ in the SiO_2 layer which yields, in combination with the earlier calculated sound velocity, the thickness $d = tv = (1072 \pm 26)\,\mathrm{nm}$ of the SiO_2 layer. Here, the agreement with the nominal thickness of $d = 1140\,\mathrm{nm}$ measured with ellipsometry is excellent.

At this point it is of interest, that the only a priori knowledge used here for the data evaluation is the index of refraction of the SiO_2 layer, a quantity that is readily available by means of e.g. ellipsometry. Thus it is possible to obtain the longitudinal sound velocity and the layer thickness simultaneously in one measurement.

It must be pointed out that the features visible in Figure 5.7 (b), i.e. the pulses at 185 ps and 368 ps, are already present in Figure 5.7 (a), but are hardly distinguishable due to the superposition of the $LiNbO_3$ signal. Here, at 368 ps an acoustic pulse echo after one roundtrip through the SiO_2 becomes visible. To be more precise, the weaker Brillouin oscillation in the SiO_2 can now be observed in the time span from 185 ps to 368 ps.

The decrease in amplitude is mainly due to the decrease in the acoustic pulse amplitude caused by a partial transmission of the acoustic pulse into the $LiNbO_3$ layer.

For SiO_2 it is not possible to obtain any information about the acoustic damping from the FFT data due to the relatively small thickness of the SiO_2 layer. Fits to the experimental data do not reveal a significant decrease in the amplitude. However, the $LiNbO_3$ layer is thick enough to obtain information on the damping. A full width at half

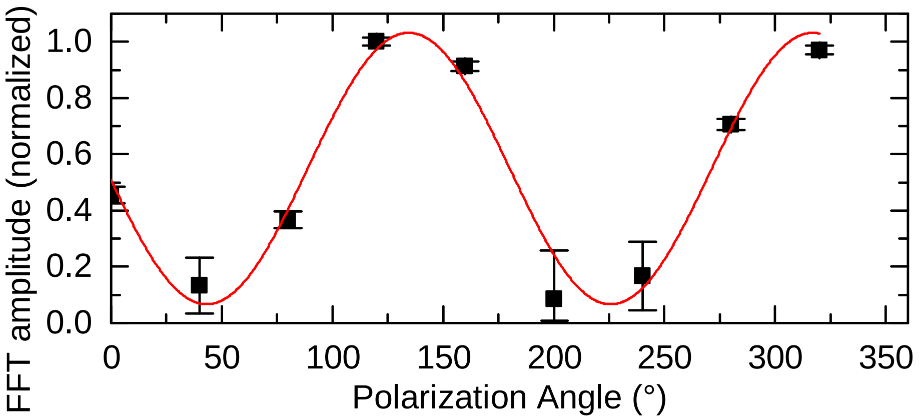

Figure 5.8.: Peak amplitude value of the response of the $LiNbO_3$ layer plotted as a function of the polarization angle of the incident pulse. The red solid line shows a fit through the experimental data points (black squares), which exhibits a sinusoidal behaviour with π periodicity. The error is estimated by the mean average of the noise floor together with the standard deviation.

maximum of (1.56 ± 0.20) GHz is obtained from a Lorentzian fit of the corresponding FFT peak. This value is consistent with a damping time of (217 ± 20) ps in the time domain obtained by a damped sinusoidal fit. This results in an acoustic absorption coefficient of $\alpha_1 = 4.4 \cdot 10^3\,\mathrm{cm}^{-1}$. Compared to the acoustic absorption obtained from the data presented in Lejman et al. [Lej16] for the Z-cut $LiNbO_3$ crystal, which is close to the orientation of the here investigated crystal, a considerable decrease in the acoustic absorption is also readily apparent in the time domain measurements. A value of $\alpha_2 = 2.42 \cdot 10^3\,\mathrm{cm}^{-1}$ can be extracted from the data. The distinct difference may be caused by different film/crystal qualities as well as the fact that the used strain pulse is only quasi-longitudinal.

A more detailed look at the probe polarization dependence of the $LiNbO_3$ signal is shown in Figure 5.8. The polarization of the probe laser pulse was systematically varied using a half-wave plate. Figure 5.8 shows the maximum of the amplitude of the FFT resulting from the $LiNbO_3$ substrate plotted versus the rotation angle of the probe laser pulse polarization.

The peak of the amplitude shows a sinusoidal behaviour with π periodicity fitted as a solid line through the data points similar to the findings and theoretical considerations in Lejman et al. [Lej16]. This can be seen by looking at the Brillouin intensities, which are given by

$$dI_{o-o} \propto r_o(1 - r_o^2)p_{21}\sin^2(\theta)E_i^2 \tag{5.5}$$

$$dI_{e-e} \propto r_e(1 - r_e^2)p_{31}\cos^2(\theta)E_i^2 \tag{5.6}$$

$$dI_{e/o-o/e} \propto r_{o/e}(1 - r_{o/e}^2)p_{41}\sin(2\theta)E_i^2 \tag{5.7}$$

with the reflectivity coefficients r_o and r_e, the photoelastic coefficients p_{ij} and the electric field E.
Here, it is important to note that only the detection sensitivity is influenced. The acoustic pulse still propagates inside the $LiNbO_3$ layer of the sample.
As described in detail in [Lej16] and summarized briefly above, the polarization dependent elimination of the signal of $LiNbO_3$ can be explained by the mode conversion process induced by the uniaxial birefringent ferroelectric material. Dependent on the $LiNbO_3$ orientation, probing at normal incidence and in backscattering geometry, up to three different Brillouin frequencies can be detected, for ordinary and extraordinary refractive indices as well as a combination of both.

This raises the question why only a single Brillouin frequency is observed in this $SiO_2/LiNbO_3$ sample. In fact, the expected shift for the two polarizations is around 1.4 GHz and thus close to the resolution limit of the system used. The shift can be calculated since the ratio of the Brillouin frequencies is in agreement with the ratio of the refractive indices [Lej16]. At 820 nm the ratio is $f_0/f_e = n_0/n_e = 1.037$. However, a closer look reveals that indeed a small shift of approximately 0.4 GHz of the Brillouin frequency is observed for orthogonal polarizations as depicted in the inset in Figure 5.7 (d). Nevertheless, with the current system configuration it is not possible to resolve two or three individual modes. This information would indeed be highly desirable to obtain, as the mode occurrence yields information about the $LiNbO_3$ crystal orientation.
Although the exact crystal orientation cannot be deduced, due to the previously discussed limitations, it is possible to conclude from the pump-probe measurements themselves that the investigated $LiNbO_3$ layer does not exhibit a Z-cut orientation (001) where the optical axis is perpendicular to the sample surface because no polarization dependence is expected in this case. Additionally it is unlikely that the sample shows a X- (100) or Y-cut (010) orientation (information on the crystal orientation can be found in [Cor]): A comparison of the modulation depth in Figure 5.8 to the results obtained in Lejman et al. [Lej16], as well as the observed sound velocities, hint to an orientation not identical but close to the Z-axis, which was indeed corroborated by X-ray measurements.

Furthermore, it is possible to obtain the acoustic reflection coefficient r between the SiO_2 and the $LiNbO_3$ layer by comparison of the Brillouin amplitudes in Figure 5.7 (b) before and after the first discontinuity. An experimental value of $r = 0.35$ is obtained. The amplitudes of the experimental data are shown in Figure 5.9. Using the earlier

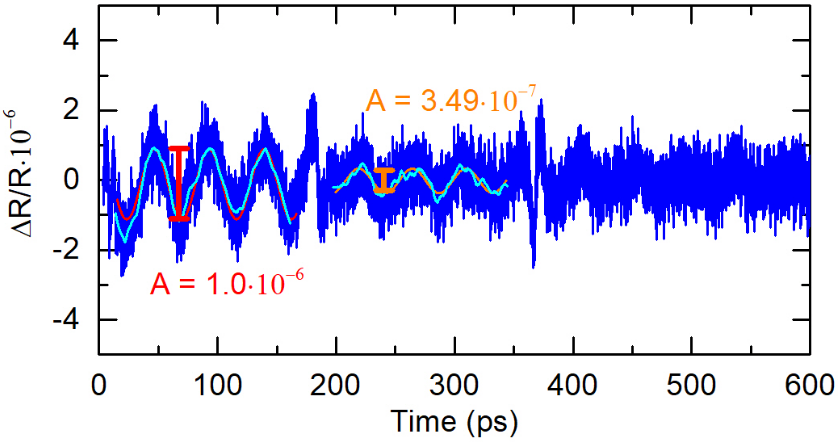

Figure 5.9.: Time-resolved reflectivity change, which was already shown in Figure 5.7 (b). Here, the fit of the amplitudes of the oscillations before and after the strain reaches the interface is indicated.

determined sound velocities of SiO_2 and $LiNbO_3$, the reflection coefficient for an assumed perfect interface can be calculated to be $r = (Z_{\text{LiNbO}} - Z_{\text{Si}})/(Z_{\text{LiNbO}} + Z_{\text{Si}})$. For the orientation of the crystal of $(\bar{1}14)$ used here with the acoustic impedance $Z = \rho \cdot v$, the reflection coefficient can be calculated to be $r = 0.37$. The densities $\rho_{SiO_2} = 2.65\,\text{g/cm}^3$, $\rho_{LiNbO_3} = 4.64\,\text{g/cm}^3$, the sound velocities $v_{SiO_2} = 5800\,\text{m}\,\text{s}^{-1}$ and $v_{LiNbO_3} = 7090\,\text{m}\,\text{s}^{-1}$ were used. All material parameters used in this thesis are listed in Appendix B.

This finding indicates a very good interface adhesion between the respective layers. The small deviation from the reflection coefficient obtained experimentally from the amplitudes can be explained by the measurement inaccuracy. Additionally it is possible that an interdiffusion at the SiO_2/$LiNbO_3$ interface appears that can enhance the acoustic transmission. Indeed, such an interface has been observed in similar layer systems after annealing due to diffusion [Nag95].

5.3. Conclusion

In this chapter, time-resolved photoacoustic metrology was applied to non-invasively characterize two layer systems: the first system with silicon dioxide on a silicon substrate and the second system with silicon dioxide on a lithium niobate substrate.

For the first system with SiO_2/Si, it is possible to obtain the sound velocities for SiO_2 and Si together with the film thickness of SiO_2 utilizing the measured Brillouin frequencies and the time of flight of the excited acoustic pulse.

For the $SiO_2/LiNbO_3$ system, the polarization dependent detection in $LiNbO_3$, due to birefringence, is utilized to infer information about the sound velocities and film thicknesses. Additionally, in this configuration information about the $LiNbO_3$ crystal orientation and the layer interface can be extracted.

It was shown that the possibility to minimize the $LiNbO_3$ signal contribution profiting from the birefringence by proper choice of the detection pulse polarization can be utilized to uncover the signal of SiO_2 and to obtain more information about the layer structure than usually possible in similar approaches.

This approach is not limited to the layer materials discussed here but can in general increase the feasibility of picosecond ultrasonic measurements in samples where birefringence is present.

CHAPTER 6

Determination of the Glass Transition in Polymethyl Methacrylate Thin Films through High-Frequency Phonons

Polymer thin films, with thicknesses ranging from a few hundreds of nanometers down to several monolayers, have been investigated extensively during the last decade, due to their importance in a wide variety of industrial applications. They are used, e.g., in nanodevices, nanotechnology, communication [Alc05, Aki11, Nap13], sensors [Löt97, Amj16], and optical coatings [Che07]. However, the dependency of the polymer glass transition on specific material properties is still subject of controversial discussions. In particular, the role of intrinsic properties, e.g. the chain length or tacticity and extrinsic effects as film thickness, confinement or film deposition procedure are still under discussion [Alc05, Eva13]. Variations of the exact preparation conditions cause a change in the behaviour of the thin film and different experimental methods achieve different results of the glass transition temperature [Alc05]. For example, the sample preparation can change the transition temperature in the polymers as it causes non-equilibrium metastable states resulting in yet unexplained properties [Rae10]. A change in the glass transition temperature can also be caused by the mechanical boundary conditions, i.e. supported or freestanding thin films show different behaviours. However, both a reduction and an increase of the glass transition temperature have been observed for the same conditions compared to bulk material [For01, Alc05]. The presence of solvents, non-equilibrium chain configurations, and potentially large stresses inside the polymer films have been identified as possible reasons for these contradictory observations [Bäu12].

A wide range of experimental techniques has been developed to determine the glass transition temperature of thin polymer films. In particular ellipsometry, which was one of the first techniques applied to thin films due to its high sensitivity in the detection of the film thickness, was used for detecting the dependence of the glass transition temperature on the thickness of polymer films [Bea93, Ked94, For01, Alc05]. Another technique that has been widely used to study polymer thin films is Brillouin scattering [Fri69, For98, Che07]. Details about several further methods can be found, e.g., in [For01, Alc05, Eva13] and a review on techniques for the investigation of thin polymer films over a broad frequency range is given in [Hec17].

Picosecond ultrasonics is well-suited to study the elastic properties of thin film systems [Ant06, Aki11, Sch14, Vol16] as also demonstrated in Chapter 5. Polymer thin films can be investigated in the submicron range down to a few monolayers [Tas92, Het16]. However, not much work has focused on the possibility of determining the glass transition in polymer films yet. Only recently, the viscoelastic properties and the glass transition of a glass-forming liquid have been investigated by time-resolved Brillouin scattering [Kli15] and the frequency dependent acoustic damping properties of different polymer types have been studied by a picosecond acoustics based pulse-echo method [Mor96]. In the following, the observations of closed-pipe organ modes in supported polymer films, where the acoustic impedance of the thin film is much lower than the impedance of the substrate [Kan90, Mor96, Aki11], are utilized in order to study the temperature dependent acoustic eigenmode behaviour of thin Poly(methyl methacrylate) (PMMA) films ($<500\,\mathrm{nm}$) and to determine the respective glass transition temperature. The method used belongs to the so-called pseudo-thermodynamic measurements, because the glass transition temperature is obtained through a change in the slope of a property of the film in relation to the temperature [Alc05]. The utilized property is the eigenmode frequency of the thin film [Alc05]. This approach is complementary to the already mentioned techniques and gives access to GHz frequencies and demonstrated film thicknesses down to 32 nm. PMMA was chosen for the measurements as its properties are well known [Ked94, Gro02].

The acoustic phonon spectra of PMMA films with varying thicknesses from $d = 458\,\mathrm{nm}$ down to $d = 32\,\mathrm{nm}$ are investigated and presented in the following. First, two sample configurations for the opto-acoustic transducer are analyzed and the reproducibility of the measurements is tested. The eigenmode spectra for the full range of thicknesses at room temperature are investigated and discussed. All appearing frequency modes can be assigned to the corresponding mode number and the thickness determined by ellipsometry can be confirmed by the measured eigenmode spectra. The temperature dependence of the frequency modes of the thin films was determined for all samples by varying the temperature of the samples from 22 °C to 200 °C. A kink in the frequency shift can be observed, which is a direct indication of the undergoing glass transition in the sample. A quantitative evaluation of the temperature induced frequency shift allows to extract the temperature dependent change in the sound velocity below the glass transition temperature. A disentanglement of the two contributions to the frequency shift, the sound velocity change and the thickness change, is not trivial and will thus be discussed in detail. The glass transition temperature is obtained from the frequency spectra through the intersection of two linear fits on the frequency shift below and above the glass transition.

6.1. Sample Preparation

The investigated samples consist of three layers. A schematic of the sample structure is depicted in Figure 6.1. From top to bottom the layers are: a poly(methyl methacrylate) (PMMA) thin film, a chromium layer and a silicon substrate.
The thin Cr layer was thermally evaporated and utilized as opto-acoustic transducer to enhance the signal. The transducer configuration is discussed in the experimental results part in the following. In Chapter 5, additional information on opto-acoustic transducers is given.

For the PMMA layer 950PMMA A Resists (purchased from MicroChem) dissolved in anisole and PMMA P9405P-MMA (purchased from Polymer Source, Inc.), dissolved in toluene was used. Several thicknesses of the PMMA layers were achieved by varying the concentrations of PMMA in the used solvent before applying the solution with a spincoater on the substrate. Afterwards, the samples were annealed for 30 min at 170 °C.

The thicknesses of the PMMA layers were determined by using the picosecond ultrasonics setup as discussed later on. The values were compared to measurements with ellipsometry. PMMA layer thicknesses from $d = 458\,\mathrm{nm}$ down to $d = 32\,\mathrm{nm}$ were obtained.

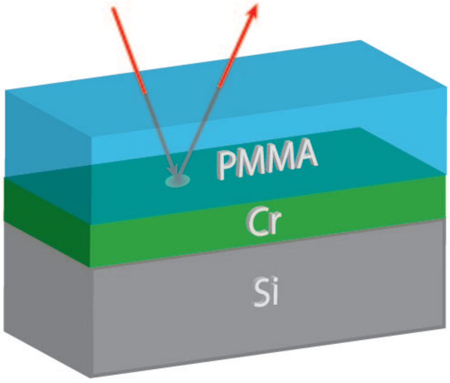

Figure 6.1.: Schematic of the sample structure. The three layers from top to bottom are PMMA, Cr and Si.

All investigated samples are listed in Table 6.1. Details will be discussed in the experimental section, in particular the considerable deviation between the ellipsometry and picosecond acoustic results for sample X2.

Sample	Thickness (nm) experimental		Thickness (nm) ellipsometry
	Position 1	Position 2	
M3	458		440
X1	350	364	342
D1	313		310
X2	233	293	257
X3	122	117	115
M2	75		74
D2	55		64
X5	36		43
X6	32		25

Table 6.1.: Thicknesses of PMMA layers obtained with the pump-probe setup (for up to two different positions on the sample) and by ellipsometry.

6.2. Theoretical Considerations

The material composition used, where the acoustic impedance of the thin film is much lower than the impedance of the adjacent layer, is expected to exhibit closed-pipe organ-like modes [Aki11]. For a thin layer, a quantization of the eigenmodes perpendicular to the film plane appears that corresponds to an oscillation of the entire film when the layer is strongly acoustically decoupled from the substrate. In Chapter 2.3.3, the eigenmodes of a thin film on a half-infinite substrate were derived. The expected frequency modes were calculated to be

$$f = (2n-1)\frac{v}{4d} \tag{6.1}$$

with the mode number $n = 1, 2, 3...$, the longitudinal sound velocity of PMMA at room temperature $v = 2750\,\mathrm{m\,s^{-1}}$ [Car03] and the layer thickness d. Both, sound velocity and thickness, depend on the temperature.

Temperature Dependent Thickness Changes

Upon changing the temperature by a temperature step ΔT of a layer with the thickness d_0 at room temperature, the layer will undergo a thermal-induced thickness change with

$$\Delta d = d_0 \cdot \alpha \cdot \Delta T \tag{6.2}$$

Typical values for the thermal expansion coefficient α for PMMA below and above the glass transition temperature have been measured by Furutani et al. [Fur96]:

$$\alpha_1 = 2.6 \cdot 10^{-4}\,\mathrm{K^{-1}} \text{ for } T < \mathrm{T_g} \text{ and}$$

$$\alpha_2 = 5.7 \cdot 10^{-4}\,\mathrm{K}^{-1} \text{ for } T > \mathrm{T_g}.$$

It is important to note that these values strongly depend on the exact film composition and thus can only serve for a qualitative comparison and as a reference for the measured data.

Temperature Dependent Changes of Sound Velocity

Similar to the thermal expansion coefficients discussed above, the sound velocity also exhibits two different temperature dependencies below and above the glass transition temperature. Again, these values can only provide an estimate of the expected change of the sound velocity due to strong differences between PMMA film behaviours. Values for the dependence of the sound velocity on the temperature were measured by Friedman et al. by Brillouin scattering [Fri69]:

$$\beta_1 = -\partial v/\partial T = 3.2\,\mathrm{m\,s^{-1}\,°C^{-1}} \text{ for } T < \mathrm{T_g} \text{ and}$$
$$\beta_2 = -\partial v/\partial T = 7.3\,\mathrm{m\,s^{-1}\,°C^{-1}} \text{ for } T > \mathrm{T_g}$$

Hence, the frequency depends on both the variations of the thickness $\Delta d(\Delta T)$ and on the variations of the sound velocity $\partial v/\partial T$.

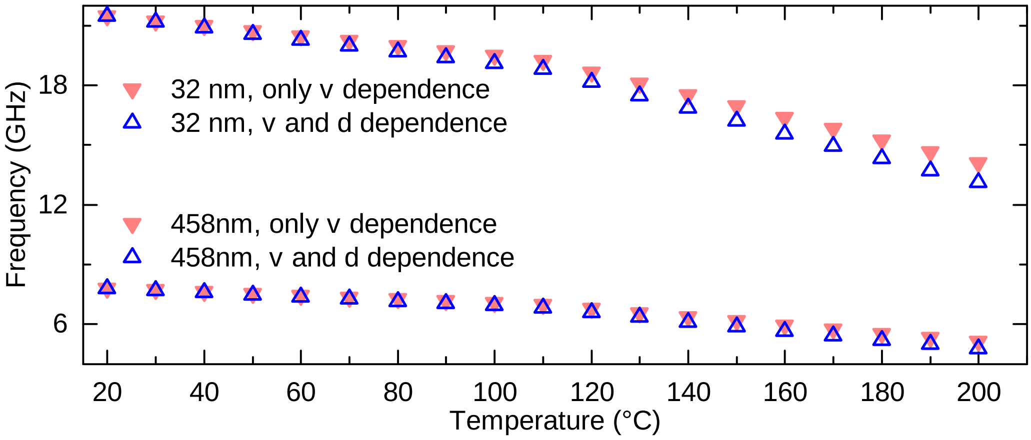

Figure 6.2.: Calculated change of the frequency modes due to a change of both sound velocity and thickness (in blue) and only of the sound velocity (red) as a function of the temperature. The calculations are for a PMMA layer thickness at room temperature of $d = 460\,\mathrm{nm}$ and $d = 32\,\mathrm{nm}$ and a sound velocity of $v = 2750\,\mathrm{m\,s^{-1}}$. The depicted modes are the calculated modes for the lowest experimentally-observable modes of the experimentally-obtained data. For $d = 32\,\mathrm{nm}$ it is $n = 1$, for $d = 458\,\mathrm{nm}$ it is $n = 5$.

Calculations of the change of the frequency of the layer's eigenmodes due to a change of the sound velocity and the thickness are presented in Figure 6.2. The frequencies were calculated for two PMMA layer thicknesses of $d = 458\,\mathrm{nm}$ and of $d = 32\,\mathrm{nm}$. A glass transition temperature of $T_g = 110\,°C$ was assumed [Fri69]. The markers in light red in Figure 6.2 show the influence on the frequency change of only the sound velocity dependence f_v, the blue markers show the influence of both the sound velocity and the thickness change on the frequency f_{all}. As the sound velocity decreases while the thickness increases, the frequency will decrease as well. Hence, the two effects increase the change of frequency and do not counteract each other.

Absolute and Relative Deviations between f_v and f_{all}
In the following, the respective influence of the two temperature dependent contributions, i.e. thickness and sound velocity, to the obtained frequency shifts will be discussed in more detail. In particular, the possibility to disentangle these contributions and thus the potential determination of the two coefficients α and β will be of interest.
The absolute value of the difference of the calculated frequencies, taking only the change of sound velocity or both contributions into account, depends on the thickness of the sample. The ratio K of the frequency change with only the influence of the sound velocity change f_v and the frequency with both sound velocity change and thickness change f_{all} yields

$$K = f_v/f_{all} = \frac{(2n-1)v(T)}{d_0} / \frac{(2n-1)v(T)}{d_0(1+\alpha\Delta T)} = 1 + \alpha\Delta T \tag{6.3}$$

The maximum ΔT which can be achieved in this measurement is about $\Delta T = 100\,\mathrm{K}$ below and above T_g. Hence, the maximum thickness change can be calculated to be $\alpha\Delta T = 0.081$, at 200 °C. Accordingly, a maximum difference of 8% at 200 °C is obtained. The influence is thus larger in absolute values for thicker layers and higher order modes. In Figure 6.2, the influence of thickness and sound velocity changes on the calculated frequency can be seen. The absolute difference is given by

$$f_v - f_{all} = \frac{(2n-1)v(T)}{d_0} - \frac{(2n-1)v(T)}{d_0(1+\alpha\Delta T)} \tag{6.4}$$

For the layer thickness of $d = 458\,\mathrm{nm}$ and for the layer of $d = 32\,\mathrm{nm}$, at 100 °C a difference of 0.15 GHz and 0.4 GHz, and at 200 °C a difference of 0.46 GHz and 1 GHz is obtained, respectively. Below the glass transition temperature, which is around 100 °C, the

the difference of the obtained frequencies is less than the resolution of the experimental setup, which is around 1 GHz. Above the glass transition temperature and for higher harmonics, the influence of the thickness change starts to become more important and a careful analysis is important.

Slope of Frequency Shift $\Delta f_n(T)$

As only the sound velocity change is considered to have a noticeable influence below $\mathrm{T_g}$ for the investigated samples, the slope of the frequency shift can be used to determine β_1. The ratio of the slope of the frequencies of two subsequent modes is given by

$$\frac{\Delta f_{n+1}}{\Delta f_n} = \frac{(2\,[n+1]-1)}{(2n-1)} \tag{6.5}$$

The slope of the frequency shift depends on the mode number. This yields for example for the second and first mode $\Delta f_2/\Delta f_1 = 3$. It can be used to calculate β_1 for $T <\mathrm{T_g}$

$$\beta_1 = 4d_0\Delta f_n/(2n-1) \tag{6.6}$$

6.3. Experimental Results

6.3.1. Sample Configuration with Opto-Acoustic Transducer

Similar to the $SiO_2/LiNbO_3$ sample in Chapter 5, an opto-acoustic metal transducer is used in this configuration to generate an acoustic pulse. The transducer is needed, as PMMA is almost transparent at around 800 nm [Mus13]. In the previous chapter, the transducer was placed on top of the sample. This approach was conducted here as well for an initial attempt to obtain information on the acoustic dynamics in the PMMA film. In Figure 6.3 (a), the time-resolved reflectivity change is shown. The fast change in the first picoseconds is, as before, due to the fast electronic response in the Cr layer. The rapid thermal expansion gives rise to an acoustic strain pulse, propagating into the PMMA layer. The detected signal shows no clear sign of acoustic eigenmodes of the PMMA layer or a reflected pulse echo. Only the oscillation of the Cr layer is visible during the first few picoseconds.

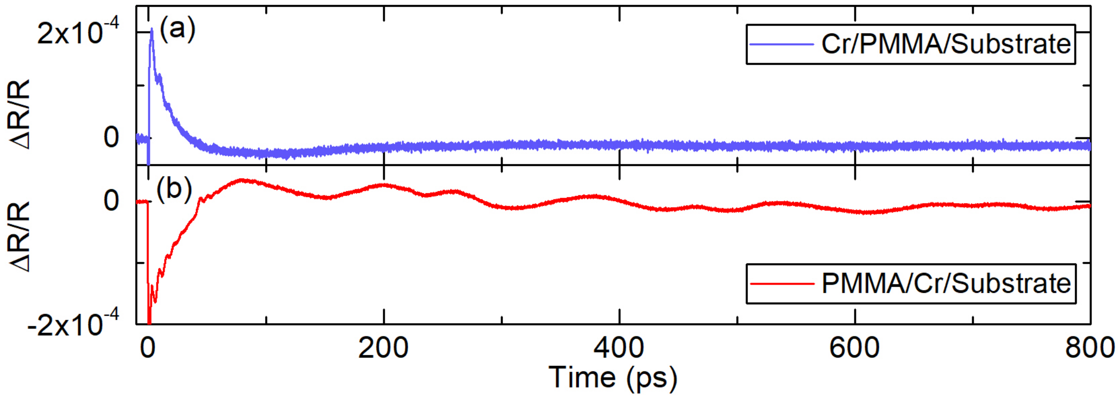

Figure 6.3.: Time-resolved reflectivity change for two different configurations of the opto-acoustic metal transducer. (a) Cr is on top of the sample. (b) Cr is between PMMA and substrate. The PMMA thickness is about $d = 313$ nm, the thickness of the Cr layer is $d = 18$ nm.

In the previous chapter, the main interest was focused on the interface of the layers. Here, in contrast, only the layer itself is of interest. Therefore, the Cr layer is placed in between the PMMA layer and the Si substrate [Wri92]. This configuration allows to excite the acoustic eigenmodes of the PMMA layer, as can be seen in the time-resolved reflectivity change presented in Figure 6.3 (b).

The incident laser pulse is almost completely transmitted through the PMMA layer and excites a strain pulse in the Cr layer. Information on the generation processes of acoustic phonons in metals can be found in Chapter 2.4. The strain pulse travels into the PMMA layer. In the first few tens of picoseconds, the oscillation of the Cr layer can be seen again. This first part of the transient is later on removed, as only the response of the PMMA layer is of interest. An extraction of the acoustic eigenmodes of the PMMA layer is possible.

For the opto-acoustic transducer, two different thicknesses of 18 nm and 60 nm were used. For the 18 nm thin film, an excitation of its eigenmodes is expected. In the thick layer, more light is reflected and less transmitted. However, no noticeable change of the acoustic response was observed in the signals for the two different thicknesses of the transducer. Figure 6.4 shows the calculated static reflectivity of a PMMA layer as a function of its thickness at a wavelength of $\lambda = 820$ nm. The blue markers show the respective thicknesses of the investigated samples.

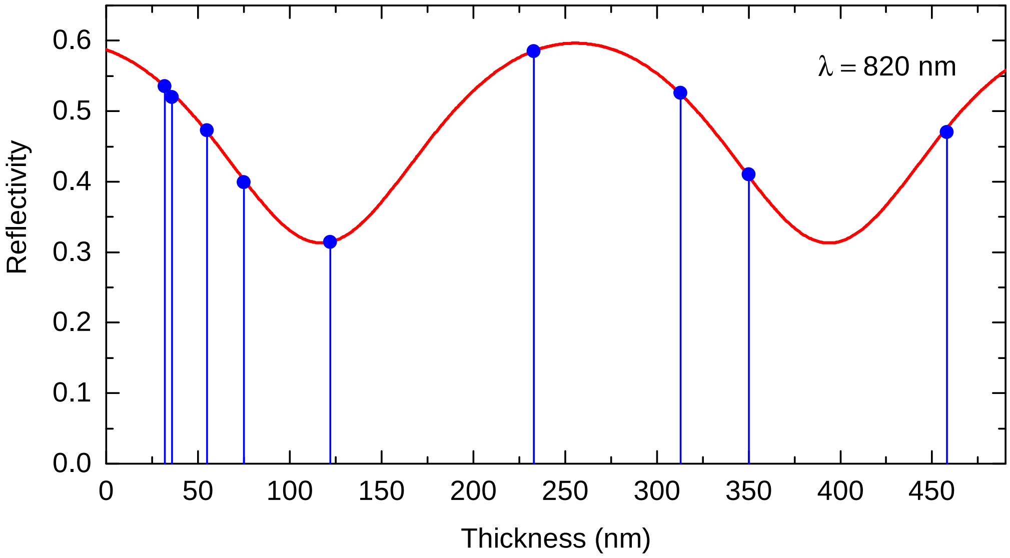

Figure 6.4.: Static reflectivity of PMMA samples as a function of the layer thickness. The blue markers show the thicknesses of the investigated samples. The reflectivity is calculated for a wavelength of λ=820 nm.

Reproducibility

Another important point that needs to be considered is the repeatability of the measurements. Thus, the same position was measured several times, with one measurement starting right after the other, and a measurement time of approximately 5 minutes. The variation of the eigenmodes is less than 0.3 GHz, which lies within the measurement error. The differences are negligible, which shows the excellent reproducibility of this approach. In the case of the temperature measurements, the frequency shift is reproducible in both directions of temperature change: The obtained results do not depend on whether the sample was heated from 21°C to 200°C or cooled from 200°C to 21°C.

6.3.2. Thickness-Dependent Mode Spectra at Room Temperature

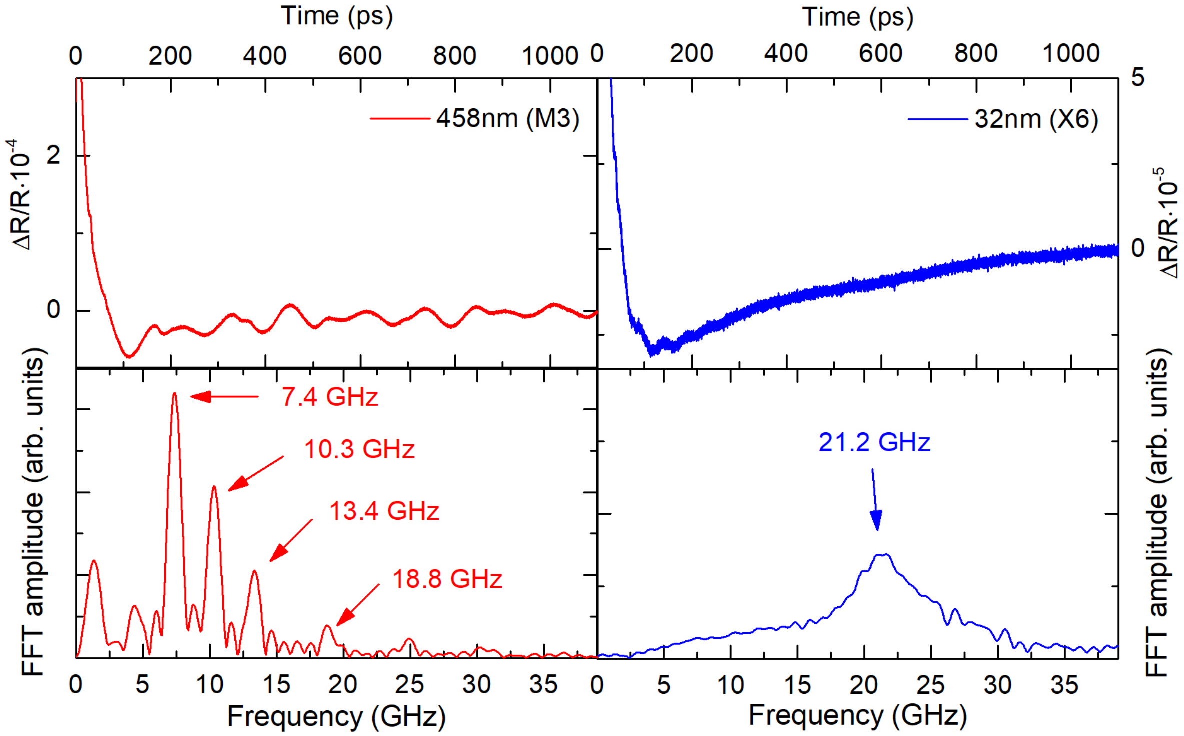

Figure 6.5.: Time-resolved reflectivity change and respective FFT for two different PMMA layer thicknesses. The thickest investigated layer with $d = 458\,\mathrm{nm}$, shown in red, and the thinnest with $d = 32\,\mathrm{nm}$, shown in blue, on a layer of 60 nm Cr. The thicknesses specified in this Figure were obtained by pump-probe measurements.

In the following, the acoustic eigenmode spectra of films with different thicknesses are discussed. Figure 6.5 shows the time-resolved reflectivity changes and the respective FFTs for the two samples with the thickest and the thinnest investigated PMMA layers, respectively. The thicknesses were determined by the pump-probe measurements to be $d = 458\,\mathrm{nm}$ and $d = 32\,\mathrm{nm}$, as discussed in the following.

For the sample with the thick PMMA layer, depicted in red, a signal with a higher amplitude of the thickness oscillations could be obtained. Frequencies of 7.4 GHz, 10.3 GHz, 13.4 GHz, and 18.8 GHz can be observed. For the thin sample, depicted in blue, only one frequency at 21.2 GHz is observed.

For the thicker sample, a distance between the frequency modes of $\Delta f = 3.0\,\mathrm{GHz}$ could be extracted, but no distinct frequency can be observed below 7.4 GHz. The expected frequency modes of a thin film on a half-infinite substrate were given before in Equation (6.1). Equation (6.1) can be used to obtain the frequency difference between two consecutive modes $n+1$ and n:

$$\Delta f = (2\left[n+1\right]-1)\frac{v}{4d} - (2n-1)\frac{v}{4d} = \frac{v}{2d} \tag{6.7}$$

A sound velocity of $v = 2750\,\mathrm{m\,s^{-1}}$ is used [Car03]. Using Equation (6.7) with $\Delta f = 3.0\,\mathrm{GHz}$, for the PMMA layer a thickness of $d = 458\,\mathrm{nm}$ is obtained. This value agrees well with the thickness obtained from the ellipsometer of $d = 440\,\mathrm{nm}$. As expected, only uneven modes are observed in this closed pipe configuration. The fundamental mode would be at $f = v/(4d) = 1.5\,\mathrm{GHz}$, hence only from a mode number of $n = 5$ or higher, modes can be detected. Lower lying frequencies are difficult to resolve.
For the thin layer a thickness of $d = v/4f = 32\,\mathrm{nm}$ can be extracted. Here, the fundamental mode with $n = 1$ is assigned to the frequency mode. The assignment was done based on the thickness assumption from the ellipsometer measurements. The value obtained from ellipsometer measurements with $d = 25\,\mathrm{nm}$ is close to the experimentally determined value.

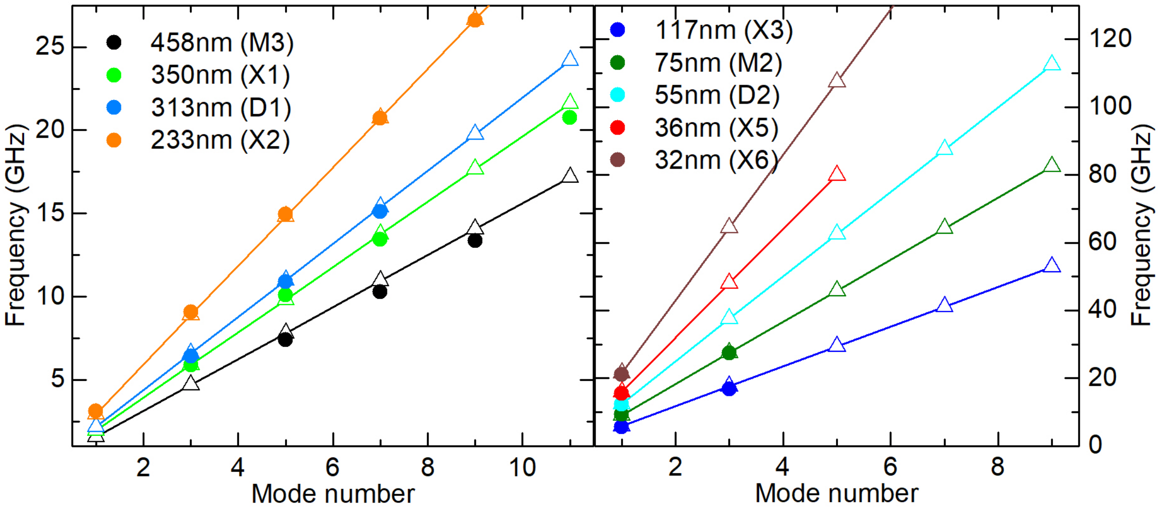

Figure 6.6.: Frequency peaks of all investigated samples, plotted against the mode numbers. The triangles show the calculated frequency peaks, connected by lines. The circles mark the positions of the experimentally-obtained modes.

Similarly, the thicknesses of all other samples are obtained. All results are in good agreement with the values extracted by ellipsometry. Both thicknesses obtained by pump-probe measurements and ellipsometry are given in Table 6.1. It is important to notice, that the ellipsometer is averaging the thickness of the sample over a much larger area than the pump-probe setup. The latter one has a beam diameter of approximately 2 µm. In contrast, the average spot size of the ellipsometer is around 2 mm. Differences of the thicknesses obtained from the two applied methods can hence be due to an inhomogeneous thickness throughout the sample. The inhomogeneity of the samples also becomes apparent in the two values of Position 1 and Position 2 in Table 6.1, where two different positions were measured on the same sample. The mean absolute deviation of the thickness of all measurements is 5.8 nm. The maximum absolute deviation is 30 nm.

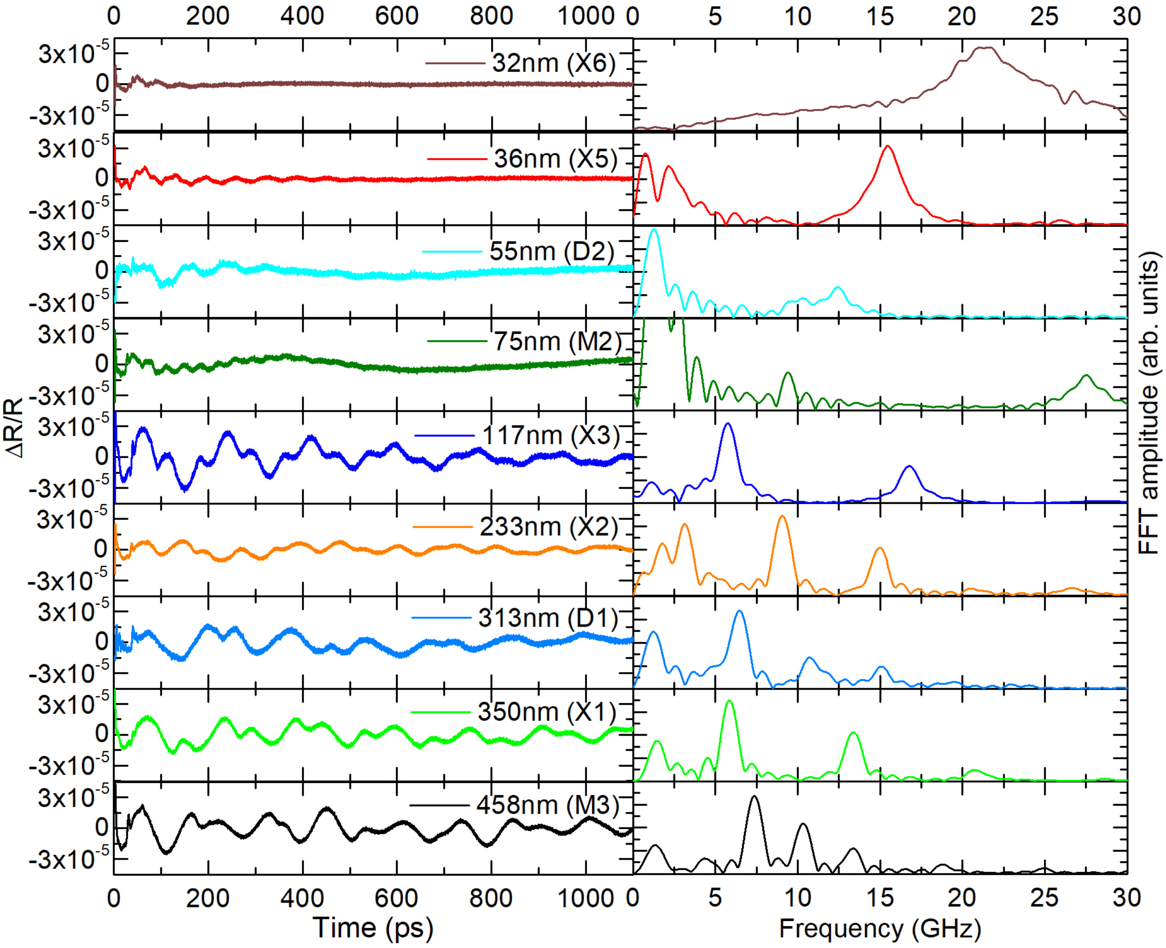

Figure 6.7.: Extracted time-resolved reflectivity change together with the respective FFTs of all investigated samples from a thickness of 32 nm up to 458 nm.

Figure 6.6 shows the extracted frequency peak positions of all investigated samples, plotted against the respective mode number. For the thickest sample, only modes from $n = 5$ on can be observed. The fundamental modes of the sample, which is at 1.5 GHz, can not be resolved here. Only frequencies higher than approximatly 3 GHz can be detected, as lower frequencies are lost during the removal of the background. For thicknesses below 233 nm, the fundamental mode can also be observed. The comparison of the experimentally-obtained modes to the calculated modes show that the correct mode number was assigned to the experimentally-observed modes. As expected, the frequency increases linearly with the mode number.

In Figure 6.7, the extracted time-resolved reflectivity change are shown along with the respective FFTs for all samples with a thickness of 32 nm up to 458 nm. The same colours are used for the samples as for the extracted frequency peaks in Figure 6.6. For thinner samples, the extracted time-resolved reflectivity change becomes less pronounced. Additionally, the damping of the oscillation increases. A thickness-dependent shift of the frequency modes can be observed.

6.3.3. Temperature Measurements

The eigenmode spectra, discussed in the previous section, show that the eigenmode frequencies can be well resolved using the presented approach. Thus, further experiments were carried out in order to test if the temperature dependent shift of the modes as well as the glass transition can be observed. Temperature measurements were performed in a motorized XY heating/freezing system (MDS 600 - Linkam Scientific Instruments). The temperature was varied from 22°C up to 200°C.

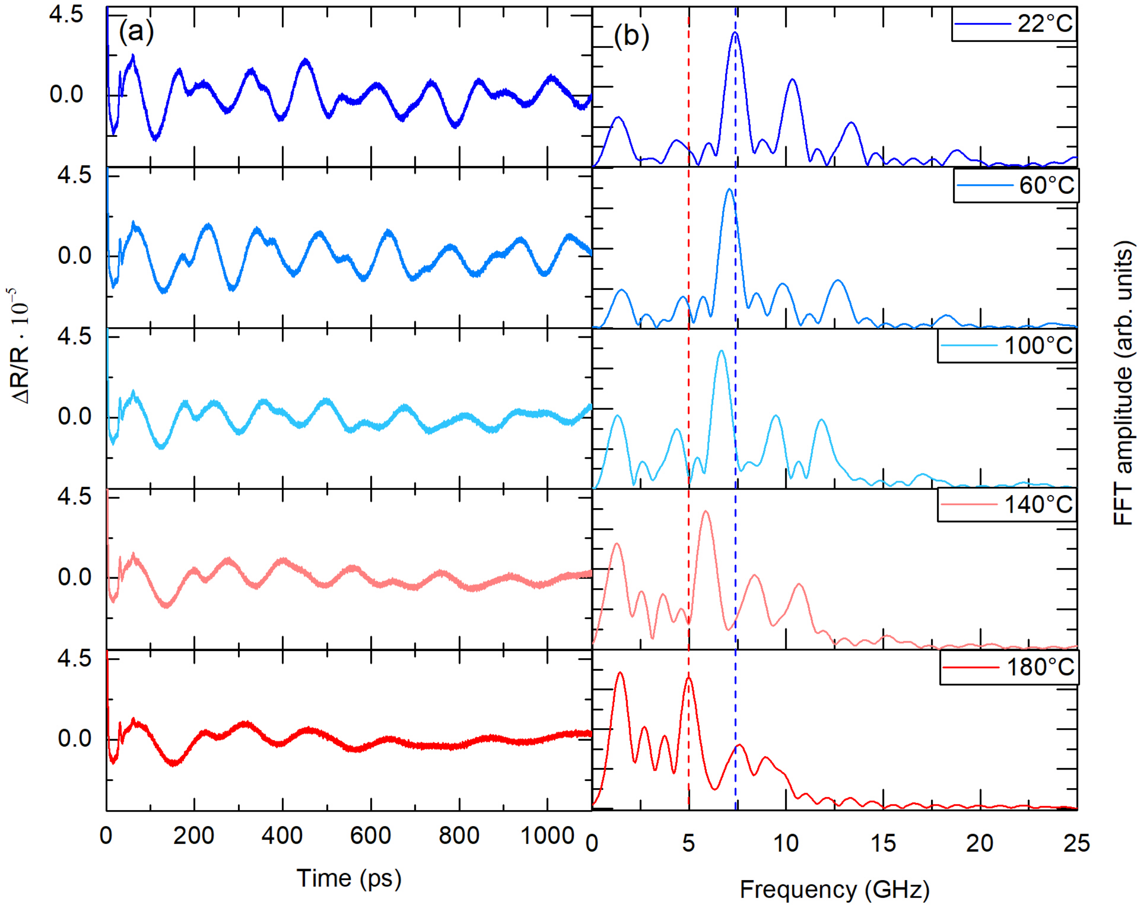

Figure 6.8.: Temperature dependence of the extracted time-resolved reflectivity change and respective FFT modes for $d = 458$ nm (M3). The dotted blue and red lines indicate the positions of the first appearing uneven modes at 22°C and 180°, respectively. A clear shift is visible.

The results for the investigated sample with the highest thickness $d = 458\,\mathrm{nm}$ (M3) are shown in Figure 6.8. The change with the temperature can be seen for the extracted time-resolved reflectivity change in (a) and for the respective FFT spectra in (b). The amplitude of the reflectivity change decreases with increasing temperature. The dotted blue and red lines in the FFT spectra serve as a guide to the eye and indicate the positions of the first appearing uneven modes at 22°C and 180°, respectively. The frequency modes shift to smaller frequencies with increasing temperature. For the lowest appearing frequency mode a shift of 2.5 GHz can be observed.

The peak frequency values can be extracted for each mode and are shown in Figure 6.9 for the thickest sample (M3) with $d = 458\,\mathrm{nm}$. In Figure 6.9 (a), the frequency peaks for n =5, 7, and 9 are plotted against the temperature. The experimentally-obtained results (blue) are compared to calculated values (red). A glass transition of T_g=110 °C was assumed for the calculations, which already yields a good agreement. For all frequency modes a change in the slope can be noticed, indicating the glass transition. The glass transition temperature appears on a slightly lower temperature than the estimated one for the calculation. A more thorough analysis of the glass transition temperature will be conducted in the following.

Figure 6.9 (b) shows the peak frequencies plotted against the mode number. Calculated and experimentally-obtained modes at 22 °C match well. A linear fit was plotted through

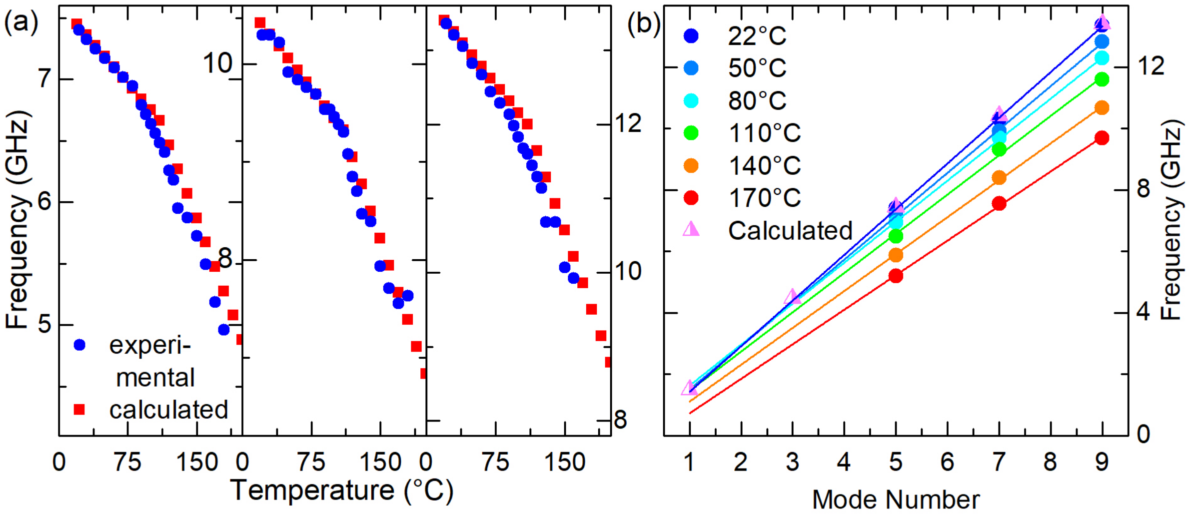

Figure 6.9.: Sample with PMMA layer thickness of $d = 458\,\mathrm{nm}$ (M3) (a) the frequencies of the first three appearing modes with n =5, 7, and 9 plotted against the temperature. Blue markers: experimentally-obtained modes, red markers: calculated modes. A glass transition temperature of T_g=110 °C was assumed. (b) Peak frequencies plotted against the mode number for temperatures from 22 °C to 180 °C. The eigenmodes were calculated for a temperature of 22 °C.

the data points. Again, it can be verified that the correct mode number has been assigned. Additionally, the change in the slopes of the modes for the respective temperature corresponds to the change in the slopes in Figure 6.9 (a). A clear difference can be seen for the change below 110 °C where each temperature step has a smaller influence on the change of the slope than above 110 °C.

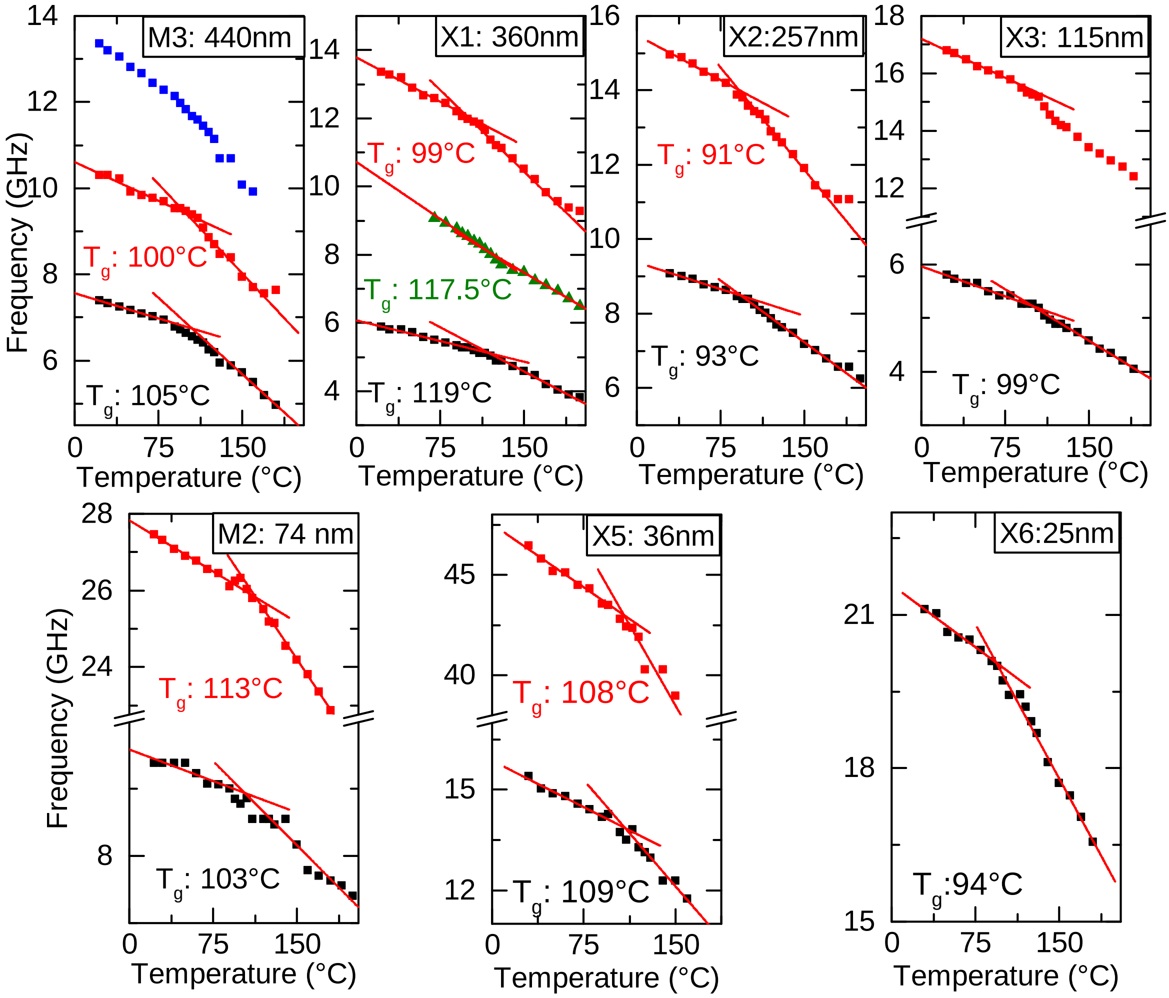

Figure 6.10.: Extracted frequency peaks for all samples. Black, red and blue squares: first, second and third appearing uneven frequency mode, respectively. Green triangles: even mode with $n = 4$. Linear fits are plotted through the two different slopes for each mode. The glass transition temperature is extracted at the intersection of the two linear fits and the value is indicated.

For all investigated samples, the frequency peak values are plotted against the temperature in Figure 6.10. The black, red and blue squares show the first, second and third appearing uneven mode, respectively. For the sample with a thickness of $d = 360\,\text{nm}$ (X1), unexpectedly an even frequency mode appears for $n = 4$, shown in green. The even mode does not appear for all temperatures but only for a temperature of $T > 60$°C. In contrast to the other modes, the even mode's slope does not become steeper above the glass transition temperature. At the moment, a conclusive explanation remains elusive. A possible explanation is, that at the interface to the Cr layer, the PMMA is heated strongly and the generated temperature gradient causes changes of the layer's behaviour.

Following a well-established simple approach [For01], the glass transition temperature can be extracted for each sample by two linear fits through the frequency peaks of each eigenmode. The temperatures are extracted at the intersection of the two fits and are indicated in Figure 6.10.

Before the thickness dependent behaviour of the transition temperature is discussed, the possibility to deduce the thermal expansion coefficient α and the temperature dependent sound velocity coefficient β will be explored. Here, the important question arises of how big the uncertainties currently are and where they originate from.
The error of the measurements is quite large. Sample X2 is the sample with the largest deviation. From the data of sample X2, the most extreme values that can be achieved for the glass transition temperature by varying the linear fits are $\mathrm{T_g}= 73\,$°C and $\mathrm{T_g}= 93\,$°C. The maximum error of the measured $\mathrm{T_g}$ can therefore be estimated to be ±10 °C.
In Table 6.2, the slopes of the fits below $\mathrm{T_g}$ of Figure 6.10 are listed. Δf_n and Δf_{n+1} are the slopes of the first and second appearing modes, respectively. From Equation (6.5) it is known, that the ratio of two consecutive modes is given by $\Delta f_{n+1}/\Delta f_n = (2\,[n+1]-1)/(2n-1)$. Therefore, for X5 to X2 a ratio of $\Delta f_2/\Delta f_1 = 3$, while for X1 $\frac{5}{3} = 1.7$ and for M3 $\frac{7}{5} = 1.4$ should be achieved. The ratios are in a good agreement to the expected values, with an exception for the sample X2, which deviated by approximately a factor of 2.

Thickness (nm)	Δf_n (m/s); n	Δf_{n+1} (m/s); n	Ratio $\Delta f_{n+1}/\Delta f_n$	β_1 (m/(s°C))
458 (M3)	-0.0078; 5	-0.012; 7	1.54	2.74 ± 0.70
359 (X1)	-0.0081; 3	-0.017; 5	2.14	3.88 ± 0.96
233 (X2)	-0.0096; 1	-0.016; 3	1.68	9.86 ± 2.05
117 (X3)	-0.0075; 1	-0.018; 3	2.4	3.45 ± 0.92
75 (M2)	-0.0063; 1	-0.018; 3	2.83	1.87 ± 0.59
36 (X5)	-0.019; 1	-0.042; 3	2.27	2.66 ± 0.29

Table 6.2.: The slopes for the frequency shift below $\mathrm{T_g}$ with the indicated mode number are given together with their ratio and the extracted β_1 value for the indicated thicknesses.

Equation (6.6) can be used to calculate β_1 for the different samples with $\beta_1 = 4d_0\Delta f_n/(2n-1)$. This is possible because, as discussed before, for $T < T_\mathrm{g}$, the influence of the thickness change of the layer is negligible.

The estimated value for the dependence of the sound velocity on the temperature, which was measured by Friedman et al. [Fri69], is $\beta_1 = 3.2\,\mathrm{m\,s^{-1}\,{}^{\circ}C^{-1}}$. All results yield reasonable values within the respective error range. The only exception is given again by sample X2, which shows a deviation from the literature value of β_1 by a factor of 3. Without X2, the average value that is achieved experimentally is $\beta_1 = (2.92 \pm 0.60)\,\mathrm{m\,s^{-1}\,{}^{\circ}C^{-1}}$. For α_2 and β_2, the extraction above the glass transition is more complicated. As discussed in the theoretical considerations of this chapter, a more careful extraction is also necessary for thin films or higher frequency modes as well. In this case, the influence of α_2 cannot be neglected anymore because the frequency shift consists of contributions of both α_2 and β_2. At the moment it is not possible to access these two values.

The glass transition temperatures, which were extracted from Figure 6.10 for the first and second appearing modes, are plotted against their PMMA layer thicknesses in Figure 6.11. However, no dependency of the glass transition temperature on the layer thickness can be observed. This can be due to the fact that there are still several sources of errors, which must be reduced to a achieve clear results.

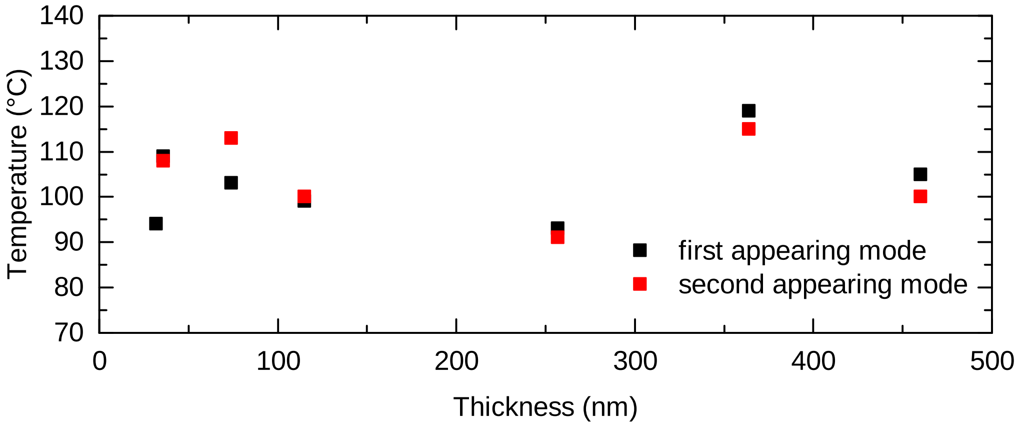

Figure 6.11.: Experimentally obtained glass transition temperatures plotted against the respective PMMA layer thicknesses for the first and second appearing uneven modes.

Several factors cause errors, as will be explained in the following. First of all, the sample fabrication poses a critical point. A number of publications show that the sample preparation has a large influence on the mechanisms in the polymers and changes the transition temperature [Alc05, Rae10]. For the elimination of measurement errors caused by the sample itself, the sample fabrication needs to be improved. The resulting homogeneous samples need to be characterized in detail in terms of their thickness prior to the realization of the measurements.

Another important point, which needs to be considered, is that the geometry of the pump-probe measurement is problematic. The employed configuration, where the sample is both pumped and probed from the front side, exhibits disadvantages. The PMMA and the Cr layers are heated from the pump pulse and the actual temperature of the layer differs from the one indicated by the heating chamber. Additionally, there is a temperature gradient in the sample. For further measurements, another configuration can be chosen to yield more reliable results. A possibility is to pump the sample from the back side and probe it from the front side of the polymer, as was demonstrated by Akimov et al. in [Aki11]. This geometry enables the elimination of influences of heating effects in the sample. No local heating effects due to the laser will influence the results. The temperature profile will not take the form of a Gaussian curve anymore, but the temperature will be the same everywhere as indicated from the heating chamber. It is not possible to pump the sample from the back side and probe it from the front side with the currently utilized ASOPS system. An amelioration of the setup would be reasonable for further investigation of these types of polymer samples.

Furthermore, for the determination of the glass transition temperature, an initial estimate of the temperature needs to be made for the selection of the two regions for the linear fits. This estimate has an impact on the results.

6.4. Conclusion

In this chapter, PMMA layers with layer thicknesses varying from $d = 32\,\mathrm{nm}$ to $d = 458\,\mathrm{nm}$ were investigated by picosecond ultrasonics. An opto-acoustic Cr transducer was placed underneath the PMMA layer to excite acoustic eigenmodes. Two Cr transducer thicknesses of $d = 18\,\mathrm{nm}$ and $d = 60\,\mathrm{nm}$ were compared in respect to their excitation effectiveness, but no significant difference in the obtained measurements could be detected. The PMMA layer thicknesses, obtained by ellipsometry, were confirmed by the pump-probe measurements. The peak frequencies were extracted from the measurements and could be assigned to their respective mode number. Calculations of the eigenmodes of a thin film on a half-infinite substrate supported the experimentally-obtained values. With decreasing PMMA layer thickness, the amplitude of the extracted time-resolved reflectivity change decreased as well, while the damping of the oscillation increases.

The temperature was varied from 22 °C to 200 °C and a shift of the frequency modes was observed. The frequency peaks of the eigenmodes were extracted and the shift of the respective modes were compared to calculations, which agreed well. The distinct change of the slope of the frequency at a temperature around 100 °C was assigned to the glass transition. For all samples, two linear fits were plotted through the two different slopes of the frequency below and above the glass transition temperature. The change of the frequency was explained by a change of both the sound velocity and the thickness of the PMMA layer with the temperature. Below the glass transition, the influence of the thickness change on the investigated samples was found to be quite small and hence was neglected. Through this assumption, the sound velocity coefficient β_1 could be extracted from the slope of the frequency shift. The obtained values of $\beta_1 = (2.92 \pm 0.60)\,\mathrm{m\,s^{-1}\,{}^{\circ}C^{-1}}$ agreed well with a literature value of $\beta_1 = 3.2\,\mathrm{m\,s^{-1}\,{}^{\circ}C^{-1}}$.

It was possible to extract the glass transition temperature $\mathrm{T_g}$ of PMMA for the different PMMA thicknesses from the intersection of the two linear fits through the measurement of the frequency dependence on the temperature. No dependency of the glass transition temperature on the layer thickness could be found. Further improvements are necessary to exclude several factors, which are influencing the results. There are several possibilities for the optimization of the measurements, such as a change of the measurement geometry to pump the sample from the back side and probe from the front side as in [Aki11]. This would avoid the influence of heating and enable homogeneous excitation of the PMMA layer only through the pulse. The sample quality must be improved, as the samples are still quite inhomogeneous.

CHAPTER 7

Summary and Outlook

BEFORE I CAME HERE I WAS CONFUSED ABOUT THIS SUBJECT. HAVING LISTENED TO YOUR LECTURE I AM STILL CONFUSED. BUT ON A HIGHER LEVEL.
- *Enrico Fermi*

The presented thesis deals with the optical generation and control of coherent acoustic phonons in different material systems. Asynchronous optical sampling (ASOPS), a time-resolved pump-probe spectroscopy technique, is used to elucidate the mechanical properties of several material systems. This is achieved through monitoring the reflectivity changes caused by the dynamics of coherent acoustic phonons in the range of up to a few hundred GHz. A femtosecond laser pump pulse generates coherent acoustic phonons in a sample. A second time delayed probe pulse detects the reflectivity changes of the sample, caused by the acoustic phonons. Time-resolved measurements of the phonon dynamics are achieved. The results of the individual investigated material systems are discussed at the end of each chapter. A summary of the main results and their impact on the field of phononics will be given in the following.

Rolled-up GaAs/InGaAs multilayer tubes A detailed experimental and theoretical study of the coherent acoustic phonon modes in planar and rolled-up InGaAs/GaAs multilayer systems with thicknesses of the layers in the nanometer range and diameters of the tubes in the micrometer range was presented. Bilayers of different materials, inherently strained through a lattice mismatch, can be rolled up to form radial superlattices. These multilayer tubes need to be defect-free and homogeneous. Therefore, it is particularly interesting to characterize the multilayer tubes non-invasively.
The first part of this chapter deals with the investigation of planar multilayers, grown by molecular beam epitaxy, and rolled-up multilayer tubes. For the planar multilayers, the experimentally-obtained acoustic modes exhibit properties of a superlattice. The Rytov model is used to calculate the dispersion relation and, hence, the expected appearing

frequency modes, which agree well with the experimentally-observed modes.

In contrast, the rolled-up superlattice tubes show intriguing differences compared to the planar structures. The Rytov model no longer accounts for the description of the acoustic eigenmodes. The differences are attributed to the imperfect adhesion between individual tube windings. A transfer matrix method is utilized, including a massless spring model accounting for the imperfect adhesion between the layers. This method yields good agreement between experiment and calculations for up to five windings. Areas with sufficient mechanical coupling between all windings can be distinguished by their acoustic mode spectrum from areas, where individual windings are only partially in contact. This allows the spatially resolved characterization of individual tubes with micrometer spatial resolution. Areas with varying interface adhesion are identified. An unambiguous assignment of the phonon modes to a specific number of coupled windings is, however, not possible, due to the complex mode spectra. The multilayer structures are found to be inhomogeneous. Further variations of the samples in the form of half-windings and pressed superlattices are investigated. The eigenmodes are found not to change considerably compared to those of the rolled-up samples. Despite the applied pressure on the samples, the individual windings are still only weakly or partially coupled.

The presented findings represent an important step towards the characterization of the mechanical interface adhesion in nanoscaled systems. The investigated microtubes in particular are a well-suited system to study the mechanical coupling in multilayer systems with increasing complexity depending on the number of windings. The results are also of general interest for nanoscaled systems on the basis of multilayer structures and possible applications can be found in nanotechnology, where the structural homogeneity is crucial for reliable applications.

Silicon dioxide on silicon and lithium niobate layer systems A thin layer of silicon dioxide (SiO_2) on two different substrates, silicon (Si) and lithium niobate ($LiNbO_3$), was investigated non-invasively. It is possible to obtain the sound velocities of the respective layers through the measured Brillouin oscillations. For the system of silicon dioxide on silicon, a sound velocity of $v = 6207\,\mathrm{m\,s^{-1}}$ for SiO_2 and of $v = 8412\,\mathrm{m\,s^{-1}}$ for Si is detected. The film thickness of SiO_2 with $d = 1143\,\mathrm{nm}$ is yielded through the round trip time of the pulse in the SiO_2 layer. The round trip time is extracted by a discontinuity in the extracted oscillations. For the second system, in $LiNbO_3$, a sound velocity of $v = 7090\,\mathrm{m\,s^{-1}}$ is obtained. The sound velocity and the thickness of the SiO_2 layer yields $v = 5797\,\mathrm{m\,s^{-1}}$ and $d = 1072\,\mathrm{nm}$. Both the sound velocity and the thickness of the SiO_2 layer can be measured simultaneously in one measurement. The only a priori knowledge used for the data evaluation is the index of refraction of the SiO_2 layer. All experimentally-obtained values are in good agreement with the literature values.

For the $LiNbO_3$ layer, a damping time of 217 ps is obtained. An acoustic absorption coefficient of $\alpha_1 = 4.4 \cdot 10^3\,\mathrm{cm^{-1}}$ can be extracted, which is by a factor of 2 larger than the value extracted from similar data in literature. The difference between the two values is explained by different crystal qualities and the only quasi-longitudinal strain pulse.

It is shown that the possibility to minimize the $LiNbO_3$ signal contribution can be utilized to uncover the signal of SiO_2. The minimization is achieved through profiting from the birefringence, and choosing an appropriate polarization for the detection pulse. Furthermore, the birefringence and the accompanying change in the detection sensitivity of coherent acoustic phonons is utilized in the $LiNbO_3$ layer to infer information about the $LiNbO_3$ crystal orientation and the quality of the layer interface. More information about the $LiNbO_3$ orientation and the layer interface is obtained than commonly possible in similar approaches. Additionally, the acoustic reflection coefficient r between SiO_2 and $LiNbO_3$ is obtained. The value of $r = 0.35$ is compared to the expected calculated value of $r = 0.37$, which indicates very good interface adhesion.

The presented procedure is not limited to the materials discussed herein, but can similarly be applied to a variety of complex layer systems based on e.g. birefringent polymers [Web00], nanocomposites [RE08], or indium tin oxide based devices [Har08]. Newly emerging materials, e.g. nanowire-based assemblies [Mus06, Kün01], exhibit strong birefringence and could be studied from a fundamental point of view. In general, the presented approach increases the feasibility of picosecond ultrasonic measurements in samples where birefringence is present. The obtained properties contain crucial information for the fabrication of surface-acoustic-wave filters for communication technology.

Poly(methylmethacrylate) thin films PMMA layers with a varying layer thickness ranging from $d = 458\,\text{nm}$ down to $d = 32\,\text{nm}$ are investigated using picosecond ultrasonics. A chromium layer is utilized as an opto-acoustic transducer between the PMMA layer and the silicon substrate to enhance the phononic signal. Two chromium thicknesses of $d = 18\,\text{nm}$ and $d = 60\,\text{nm}$ are used, but no significant difference in the acoustic signal of the obtained measurements can be detected.

The PMMA layer thicknesses obtained by ellipsometry for the different samples are confirmed by the pump-probe measurements. The peak frequencies are extracted and can be assigned to their respective mode number. Calculations of the eigenmodes support the experimentally-obtained values.

Temperature measurements between 22 °C and 200 °C were performed. A shift of the frequency modes towards lower frequencies is observed for rising temperatures. The change of the frequency is assigned to a change of both the sound velocity and the thickness of the PMMA layer with temperature. For the peak frequencies as a function of the temperature, a distinct change of the slope of the frequency at around 100 °C is detected. The kink in the frequency shift is a direct indication of the undergoing glass transition in the PMMA layer. A quantitative evaluation of the temperature-induced frequency shift allows extraction of the temperature-dependent change of the sound velocity below the glass transition temperature with a value of $\beta_1 = -\partial v/\partial T = (2.92 \pm 0.60)\,\text{m}\,\text{s}^{-1}\,{}^{\circ}\text{C}^{-1}$.

It is possible to obtain the glass transition temperature T_g of PMMA for the different thicknesses from the frequency spectra through the intersection of two extrapolated linear fits of the frequency shift. No dependency of the glass transition temperature on the PMMA layer thicknesses is found.

Further improvements are necessary to exclude several factors, which influence the results. Several possibilities for the optimization of the measurements were suggested, e.g., an improvement of the sample quality. Additionally, a change of the measurement geometry to pump the sample from the back side and probe from the front side as in [Aki11], to exclude the influence of heating of the PMMA layer, was proposed.

The presented approach for the investigation of the glass transition temperature is complementary to other therefore applied techniques, and gives access to the glass transition temperature through GHz frequencies.

CHAPTER 8

Zusammenfassung

Die vorliegende Doktorarbeit befasst sich mit der optischen Anregung und Kontrolle kohärenter akustischer Phononen in verschiedenen Materialsystemen. Asynchrones optisches Abtasten (ASOPS), eine zeitaufgelöste Anrege-Abfrage Spektroskopiemethode, wird verwendet, um die mechanischen Eigenschaften diverser Materialsysteme zu untersuchen. Dies wird durch Messung der Reflektivitätsänderung erreicht, die durch die Dynamiken der kohärenten akustischen Phononen, im Bereich bis zu einigen hundert GHz, ausgelöst wurde. Kohärente akustische Phononen werden durch einen auf das Substrat auftreffenden Femtosekunden-Laserpuls erzeugt. Ein zweiter, zeitverzögerter Abfragepuls detektiert die Reflektivitätsanderungen, die durch die akustischen Phononen generiert wurden. Zeitaufgelöste Messungen der Phononendynamiken können erzielt werden. Die Ergebnisse der untersuchten Materialsysteme wurden am Ende des jeweiligen Kapitels zusammengefasst. Eine Zusammenfassung der Hauptergebnisse und ihre Auswirkungen auf den Bereich der Phononik wird im Folgenden gegeben.

Aufgerollte GaAs/InGaAs Mehrfachschicht-Rollen Es wurde eine ausführliche experimentelle und theoretische Studie zu kohärenten akustischen Phononen in ebenen und aufgerollten GaAs/InGaAs Mehrfachschichtsystemen präsentiert, mit Dicken der Schichten im Nanometer- und Durchmesser der Rollen im Mikrometerbereich. Doppelschichten, bestehend aus zwei unterschiedlichen Materialien, die durch eine Gitterfehlanpassung inhärent verspannt sind, können aufgerollt werden zu radialen Übergittern. Diese Mehrfachschicht-Rollen müssen defektfrei und homogen sein. Daher ist von besonderem Interesse, die Mehrfachschicht-Rollen nicht-invasiv zu charakterisieren.

Der erste Teil dieses Kapitels befasst sich mit der Untersuchung von ebenen Mehrfachschichten, die durch Molekularstrahlepitaxie gewachsen wurden, und aufgerollten Mehrfachschicht-Rollen. Die experimentell erzielten akustischen Moden der ebenen Mehrfachschichten weisen die Eigenschaften eines Übergitters auf. Das Rytov Modell wird verwendet um die Dispersionsrelation und die dadurch zu erwartenden auftretenden Frequenzmoden zu berechnen. Die berechneten Moden stimmen gut mit den experimentellen

Moden überein.
Im Gegensatz dazu zeigen die aufgerollten Übergitter verblüffende Unterschiede verglichen mit den ebenen Strukturen. Das Rytov Modell kann nicht mehr für die Beschreibung der akustischen Eigenmoden verwendet werden. Die Unterschiede werden einer nicht perfekten Haftung zwischen den einzelnen Schichten der Rolle zugeschrieben. Eine Transfermatrixmethode wird verwendet inklusive eines masselosen Federmodells, das die nicht perfekte Adhäsion zwischen den Schichten beschreibt. Diese Methode erzielt eine gute Übereinstimmung mit den experimentellen Ergebnissen für bis zu fünf Windungen. Bereiche mit einer guten mechanischen Kopplung zwischen allen einzelnen Windungen können aufgrund ihres akustischen Modenspektrums von Bereichen unterschieden werden, in denen einzelne Windungen nur teilweise in Kontakt sind. Dies erlaubt die räumlich aufgelöste Charakterisierung von einzelnen Rollen mit einer räumlichen Auflösung im Mikrometerbereich. Bereiche unterschiedlicher Grenzflächenadhäsion können identifiziert werden. Eine eindeutige Zuordnung der Phononmoden zu einer spezifischen Anzahl von gekoppelten Windungen ist aufgrund komplexer Modenspektren jedoch nicht immer möglich. Es wurde gezeigt, dass die Mehschichtsysteme inhomogen sind. Weitere Variationen der Proben in Form von Spiralen und gepressten Übergittern wurden untersucht. Die Eigenmoden weisen keine erheblichen Unterschiede auf, verglichen mit denen der aufgerollten Proben. Trotz des angewendeten Drucks auf die gepressten Proben sind die einzelnen Windungen immer noch nur schwach oder teilweise gekoppelt.
Die vorgestellten Ergebnisse stellen einen wichtigen Schritt in Richtung der Charakterisierung mechanischer Grenzflächen in Nano-Systemen dar. Insbesondere die untersuchten Mehrfachschicht-Rollen bieten sich als äusserst passendes System an, um die mechanische Kopplung in Mehrfachschicht-Systemen mit steigender Komplexität in Abhängigkeit von der Windungszahl zu untersuchen. Die Ergebnisse sind ebenfalls von allgemeinem Interesse für Nano-Systeme basierend auf Mehrfachschicht-Systemen. Mögliche Anwendungen können in der Nanotechnologie gefunden werden, wo eine strukturelle Homogenität ausschlaggebend ist für eine zuverlässige Anwendung.

Siliziumdioxid auf Silizium und Lithiumniobat Schichtsysteme Ein dünner Film von Siliziumdioxid (SiO_2) auf zwei verschiedenen Substraten, bestehend aus Silizium (Si) und Lithiumniobat ($LiNbO_3$), wurde nicht-invasiv untersucht. Die Schallgeschwindigkeiten der jeweiligen Schichten können durch Brillouin Oszillationen gemessen werden. Für das erste System, bestehend aus SiO_2 auf Si, wurde eine Schallgeschwindigkeit von $v = 6207\,\mathrm{m\,s^{-1}}$ für SiO_2 und von $v = 8412\,\mathrm{m\,s^{-1}}$ für Si erzielt. Für die Schichtdicke von SiO_2 konnte ein Wert von $d = 1143\,\mathrm{nm}$ gemessen werden durch die Umlaufszeit des Pulses in der SiO_2 Schicht. Die Umlaufszeit konnte durch eine Diskontinuität in der extrahierten Oszillation bestimmt werden. In dem zweiten System wurde für $LiNbO_3$ eine Schallgeschwindigkeit von $v = 7090\,\mathrm{m\,s^{-1}}$ gemessen. Für die Schallgeschwindigkeit und Dicke der SiO_2 Schicht wurden jeweils $v = 5797\,\mathrm{m\,s^{-1}}$ und $d = 1072\,\mathrm{nm}$ erzielt.

Schallgeschwindigkeit und Dicke der SiO_2 Schicht können simultan in einer Messung bestimmt werden. Dafür wird als einziges Vorwissen für die Datenauswertung der Brechungsindex der SiO_2 Schicht benötigt. Alle experimentell erzielten Werte sind in guter Übereinstimmung mit den Literaturwerten.

Für $LiNbO_3$ wurde eine Dämpfungszeit von $(217 \pm 20)\,\mathrm{ps}$ gemessen. Der akustische Absorptionskoeffizient kann daraus mit einem Wert von $\alpha_1 = 4.4 \cdot 10^3\,\mathrm{cm}^{-1}$ extrahiert werden. Dieser ist um einen Faktor von 2 größer als Literaturwerte vergleichbarer Proben. Der Unterschied zwischen den beiden Werten wird durch unterschiedliche Kristallqualitäten und den nur quasi-longitudinalen Verspannungspuls erklärt.

Es wird gezeigt, dass es möglich ist, das Signal des SiO_2 freizulegen, indem der Beitrag des $LiNbO_3$ Signals minimiert wird. Die Minderung wird dadurch erreicht, dass die Doppelbrechung durch geeignete Wahl der Polarisierung des Abfragepulses genutzt wird. Des Weiteren wird die Doppelbrechung und die mit einherlaufende Änderung der Detektionssensitivität der kohärenten akustischen Phononen im $LiNbO_3$ verwendet, um Informationen zu der $LiNbO_3$ Kristallorientierung und der Qualität der Grenzflächen zu erhalten. Es können mehr Informationen zu der $LiNbO_3$ Kristallorientierung und der Grenzflächen erhalten werden, als es normalerweise mit ähnlichen Vorgehensweisen möglich ist. Der akustische Reflektionskoeffizient r zwischen SiO_2 und $LiNbO_3$ wurde gemessen. Der erzielte Wert von $r = 0.35$ wurde mit dem berechneten Wert von $r = 0.37$ verglichen und lässt auf eine sehr gute Grenzflächenadhäsion schliessen.

Die vorgestellte Vorgehensweise ist nicht nur auf die hier diskutierten Materialien limitiert. Auf gleiche Weise können auch eine Vielzahl weiterer komplexer Schichtsysteme, zum Beispiel basierend auf doppelbrechenden Polymeren [Web00], Nanokompositen [RE08] oder Indium Tin Oxide basierten Bauteilen [Har08], damit untersucht werden. Neu auftauchende Materialien, wie beispielsweise Nanodraht-basierte Bauteile [Mus06, Kün01] weisen starke Doppelbrechung auf und könnten von einem fundamentalen Standpunkt aus untersucht werden. Im Allgemeinen erhöht die vorgestellte Herangehensweise die Durchführbarkeit von Pikosekunden-Ultraschall Messungen in Proben, in denen Doppelbrechung vorhanden ist. Die gemessenen Eigenschaften enthalten wichtige Informationen für die Herstellung von akustischen Oberflächenwellen-Filtern für die Kommunikationstechnologie.

Poly(methylmethacrylate) Dünnfilme PMMA-Schichten mit verschiedenen Schichtdicken im Bereich von $d = 458\,\mathrm{nm}$ bis zu $d = 32\,\mathrm{nm}$ wurden mit Hilfe von Pikosekunden-Ultraschall untersucht. Zwischen der PMMA-Schicht und dem Silikonsubstrat wird eine Chromschicht als opto-akustischer Transducer verwendet, um das phononische Signal zu verstärken. Zwei unterschiedliche Chromschichtdicken von $d = 18\,\mathrm{nm}$ und $d = 60\,\mathrm{nm}$ wurden verwendet. Allerdings kann zwischen den beiden Dicken im Zuge der durchgeführten Messungen kein signifikanter Unterschied des akustischen Signals festgestellt werden.

Die durch Ellipsometrie bestimmten Schichtdicken der PMMA-Schichten wurden durch die Anrege-Abfrage Messungen bestätigt. Die Maxima der Frequenzen wurden extrahiert und können ihrer entsprechenden Modenzahl zugeordnet werden. Berechnungen der Eigenmoden unterstützen die experimentell erzielten Werte.

Temperaturmessungen wurden durchgeführt, bei denen die Temperatur zwischen 22 °C und 200 °C variiert wurde. Für ansteigende Temperaturen kann eine Verschiebung der Frequenzmoden in Richtung niedrigerer Frequenzen gemessen werden. Die Änderung der Frequenz wird einer temperaturbedingten Änderung sowohl der Schallgeschwindigkeit, als auch der Schichtdicke von PMMA zugeschrieben. Für die Maxima der Frequenzen wird in Abhängigkeit von der Temperatur eine deutliche Änderung der Steigung der Frequenz bei etwa 100 °C festgestellt. Die Änderung der Frequenzverschiebung ist ein direkter Indikator des vorgehenden Glassübergangs in der PMMA Schicht. Eine quantitative Auswertung der temperaturbedingten Frequenzverschiebung ermöglicht es, die temperaturabhängige Änderung der Schallgeschwindigkeit unterhalb der Glassübergangstemperatur zu extrahieren. Ein Wert von $\beta_1 = -(2.92 \pm 0.60)\,\mathrm{m\,s^{-1}\,°C^{-1}}$ wurde bestimmt. Durch den Schnittpunkt der extrapolierten linearen Fits der Frequenzänderung in den Frequenzspektren ist es möglich, die Glasübergangstemperatur $\mathrm{T_g}$ von PMMA für unterschiedliche Schichtdicken zu erhalten. Es kann keine Abhängigkeit zwischen Glasübergangstemperatur und PMMA Schichtdicke nachgewiesen werden.

Um verschiedene Faktoren auszuschließen, welche die Resultate beeinflussen, sind weitere Verbesserungen notwendig. Zur Optimierung der Messungen wurden mehrere Möglichkeiten vorgeschlagen, wie z.B. eine Verbesserung der Probenqualität. Um eine Beeinflussung der Messergebnisse durch Erhitzung der PMMA-Schichten auszuschließen, wird zusätzlich eine Veränderung des Messaufbaus vorgeschlagen. So sollten Anregung und Abfrage räumlich getrennt von Hinter- und Vorderseite der Probe aus durchgeführt werden wie in [Aki11] beschrieben.

APPENDIX A

Fabrication of Rolled-up Multilayer Structures

All rolled-up multilayer tube samples investigated in Chapter 4 were produced in the Institute for Integrative Nanosciences (IFW) in Dresden, Germany. The multilayer structures are produced in a top-down fabrication process.

A.1. Shape of Starting Window

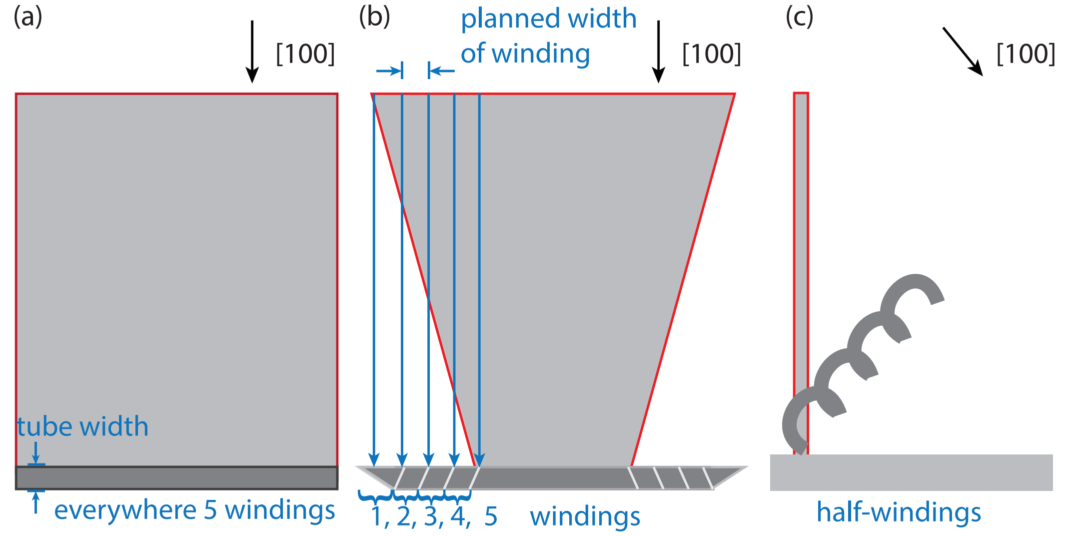

Figure A.1.: Shape of starting window for etching process, illustrated by red lines. The dark grey structures depict the structures resulting from the starting window. (a) A rectangular shape results into a multilayer tube with the same amount of windings at every part. (b) A triangular shape results into a multilayer tube with an increasing number of windings towards the center of the tube. (c) A small stripe with an angle to the [100] direction of the substrate will result into spirals.

After all layers are placed on the sample, a starting window needs to be defined by lithography. The exact shape of the starting window will influence the roll-up process and structures with varying shapes can be achieved as shown in Figure A.1 [Pri00, Bel06]. A rectangular shape will result in a regular rolled-up multilayer tube as can be seen in Figure A.1 (a). A triangular cut will result in a multilayer tube with a varying number of windings, depicted in Figure A.1 (b). The last possibility, which is used here, is a small rectangular stripe that rolls up under an angle to the [100] direction. It results into a helical structure – spirals are formed, as shown in Figure A.1 (c).

A.2. Protection Layer

The etching can also cause a roll up of all sides of the cut. For the prevention of undesirable side roll effects, a protection layer can be used. Therefore, several materials can be used. Here, Al_2O_3 and AlAs are utilized.

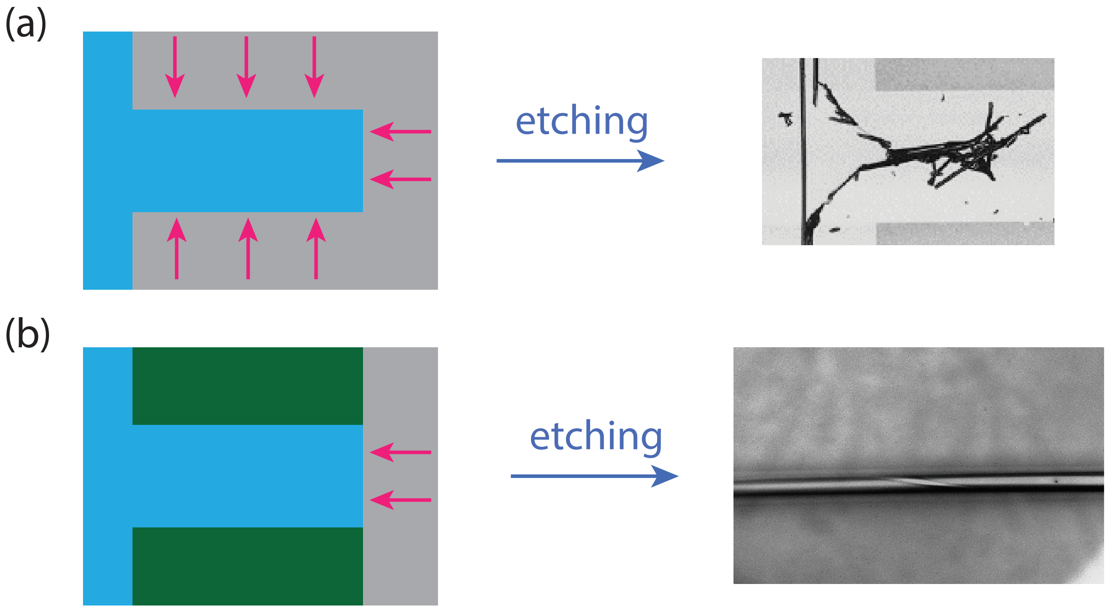

Figure A.2.: Influence of the protection layer during the etching process (a) Without a protection layer, the layer starts to roll up from every side and no proper multilayer tube is formed. The microscope image was taken from IFW Dresden. (b) With a protection layer, the layers roll-up from only one direction, resulting in a multilayer tube.

APPENDIX B

Optical Data of Materials

The material properties used in this thesis are summarized and listed below.

Chapter 4

	GaAs	**InGaAs**	**Al_2O_3**	**AlAs**
Refractive index n for $\lambda = 820\,\mathrm{nm}$	3.66	3.7	1.76	3.01
Speed of sound v_l (in m/s)	4730	4550	9900	5650
Band gap energy E_g (in eV)	1.42	1.14	3.2	2.2
Density ρ (in g/cm^3)	5.32	5.384	3.94	3.72

Chapter 5

	$LiNbO_3$	**SiO_2**	**Si**	**Al**
Refractive index n_o for $\lambda = 820\,\mathrm{nm}$	2.25	1.45	3.68	2.75
Refractive index n_e for $\lambda = 820\,\mathrm{nm}$	2.17			
Speed of sound v_l (in m/s)	7245	5800	8430	6320
Density ρ (in g/cm^3)	4.64	2.65	3.68	2.7

Chapter 6

	PMMA	**Cr**
Refractive index n for $\lambda = 820\,\mathrm{nm}$	1.48	3.16
Speed of sound v_l (in m/s)	2750	6650
Density ρ (in g/cm^3)	1.19	7.2

Bibliography

[Aki11] A. V. Akimov, E. S K Young, J. S. Sharp, V. Gusev, and A. J. Kent, *Coherent hypersonic closed-pipe organ like modes in supported polymer films*, Applied Physics Letters **99**, 8–11 (2011).

[Alc05] M. Alcoutlabi and G. B. McKenna, *Effects of confinement on material behaviour at the nanometre size scale*, Journal of Physics: Condensed Matter **17**, R461–R524 (2005).

[Amj16] M. Amjadi, K. Kyung, I. Park, and M. Sitti, *Stretchable, Skin-Mountable, and Wearable Strain Sensors and Their Potential Applications: A Review*, Advanced Functional Materials **26**, 1678–1698 (2016).

[Ang12] T. Angelova, N. Shtinkov, T. Ivanov, V. Donchev, A. Cantarero, C. Deneke, O. G. Schmidt, and A. Cros, *Optical and acoustic phonon modes in strained InGaAs/GaAs rolled up tubes*, Applied Physics Letters **100**, 201904 (2012).

[Ant06] G. A. Antonelli, B. Perrin, B. C. Daly, and D. G. Cahill, *Characterization of Mechanical and Thermal Properties Using Ultrafast Optical Metrology*, MRS Bulletin **31**, 607–613 (2006).

[Ash05] N. W. Ashcroft and N. D. Mermin, *Festkörperphysik*, Oldenbourg Wissenschaftsverlag GmbH, München, 2005.

[Aul73] B.A. Auld, *Acoustic Fields and Waves in Solids*, New York: Wiley, 1973.

[Bar98] A. Bartels, T. Dekorsy, H. Kurz, and K. Koehler, *Coherent control of acoustic phonons in semiconductor superlattices*, Applied Physics Letters **72**, 2844 (1998).

[Bar99] A. Bartels, T. Dekorsy, H. Kurz, and K. Köhler, *Coherent Zone-Folded Longitudinal Acoustic Phonons in Semiconductor Superlattices: Excitation and Detection*, Physical Review Letters **82**, 1044–1047 (1999).

[Bar06] A. Bartels, F. Hudert, C. Janke, T. Dekorsy, and K. Köhler, *Femtosecond time-resolved optical pump-probe spectroscopy at kilohertz-scan-rates over nanosecond-time-delays without mechanical delay line*, Applied Physics Letters **88**, 1–3 (2006).

[Bar07] A. Bartels, R. Cerna, C. Kistner, A. Thoma, F. Hudert, C. Janke, and T. Dekorsy, *Ultrafast time-domain spectroscopy based on high-speed asynchronous optical sampling.*, The Review of scientific instruments **78**, 035107 (2007).

[Bar14] I. D. Barcelos, L. G. Moura, R. G. Lacerda, and A. Malachias, *Observation of strain-free rolled-up CVD graphene single layers: Toward unstrained heterostructures*, Nano Letters **14**, 3919–3924 (2014).

[Bäu12] O. Bäumchen, J. D. McGraw, J. A. Forrest, and K. Dalnoki-Veress, *Reduced Glass Transition Temperatures in Thin Polymer Films : Surface Effect or Artifact?*, Physical Review Letters **109**, 055701 (2012).

[Bea93] G. Beaucage, R. Composto, and R. S. Stein, *Ellipsometric Study of the Glass Transition and Thermal Expansion Coefficients of Thin Polymer Films*, Journal of Polymer Science Part B: Polymer Physics **31**, 319–326 (1993).

[Bea96] E. Beaurepaire, J. Merle, A. Daunois, and J. Bigot, *Ultrafast Spin Dynamics in Ferromagnetic Nickel*, Physical Review Letters **76**, 4250–4253 (1996).

[Bel06] D. J. Bell, L. Dong, B. J. Nelson, M. Golling, L. Zhang, and D. Grützmacher, *Fabrication and characterization of three-dimensional InGaAs/GaAs nanosprings*, Nano Letters **6**, 725–729 (2006).

[Ber06] A. Bernardi, a. R. Goni, M. I. Alonso, F. Alsina, H. Scheel, P. O. Vaccaro, and N. Saito, *Probing residual strain in InGaAs/GaAs micro-origami tubes by micro-Raman spectroscopy*, Journal of Applied Physics **99**, 063512 (2006).

[Bho06] S. Bhowmick and V. B. Shenoy, *Effect of strain on the thermal conductivity of solids*, Journal of Chemical Physics **125**, 164513 (2006).

[Bis12] K. Biswas, J. He, I. D. Blum, C. Wu, T. Hogan, D. N. Seidman, V. P. Dravid, and M. G. Kanatzidis, *High-performance bulk thermoelectrics with all-scale hierarchical architectures*, Nature **489**, 414 (2012).

[Bri17a] D. Brick, E. Emre, M. Grossmann, T. Dekorsy, and M. Hettich, *Picosecond Photoacoustic Metrology of SiO2 and LiNbO3 Layer Systems Used for High Frequency Surface-Acoustic-Wave Filters*, Applied Sciences **7**, 1–7 (2017).

[Bri17b] D. Brick, V. Engemaier, Y. Guo, M. Grossmann, G. Li, D. Grimm, O. G. Schmidt, M. Schubert, V.E. Gusev, M. Hettich, and T. Dekorsy, *Interface Adhesion and Structural Characterization of Rolled-up GaAs/InGaAs Multilayer Tubes by Coherent Phonon Spectroscopy*, Scientific Reports **7**, 1–8 (2017).

[Bru12] A. Bruchhausen, J. Lloyd-Hughes, M. Hettich, R. Gebs, M. Grossmann, O. Ristow, A. Bartels, M. Fischer, M. Beck, G. Scalari, J. Faist, A. Rudra, P. Gallo, E. Kapon, and T. Dekorsy, *Investigation of coherent acoustic phonons in terahertz quantum cascade laser structures using femtosecond pump-probe spectroscopy*, Journal of Applied Physics **112**, 033517 (2012).

[Car89] M. Cardona and G. Guentherodt, *Light Scattering in Solids V - Superlattices and Other Microstructures*, Springer-Verlag, 1989.

[Car03] J.E. Carlson, J. van Deventer, A. Scolan, and C. Carlander, *Frequency and temperature dependence of acoustic properties of polymers used in pulse-echo systems*, IEEE Symposium on Ultrasonics, 2003 **1**, 885–888 (2003).

[Che89] E. J. Chern and H. T. C. Nielsen, *Generalized formulas for reflected pulse response of multilayered structures*, Journal of Applied Mechanics **66**, 2833 (1989).

[Che07] W. Cheng, R. Sainidou, P. Burgardt, N. Stefanou, A. Kiyanova, M. Efremov, G. Fytas, and P. F. Nealey, *Elastic Properties and Glass Transition of Supported Polymer Thin Films*, Macromolecules **40**, 7283–7290 (2007).

[Che15] X. Chen, M. Ali, M. Conwaybo, Y. Yang, and T. Ren, *High performance lithium niobate surface acoustic wave transducers in the 4 – 12 GHz super high frequency range*, American Vacuum Society **401**, 06F401 (2015).

[Cle03] A. N. Cleland, *Foundations of Nanomechanics*, Springer-Verlag, Berlin Heidelberg New York, 2003.

[Cor] MTI Corporation, *http://www.mtixtl.com/linbo3.aspx.*

[Deh15] T. Dehoux, M. Abi Ghanem, O. F. Zouani, Y. Guillet, S. Dilhaire, and B. Audoin, *All-optical broadband ultrasonography of single cells*, Scientific Reports **5**, 1–5 (2015).

[Dem99] J. Demsar, B. Podobnik, V.V. Kabanov, and D. Mihailovic, *The superconducting gap, the pseudogap and pair fluctuations above Tc in overdoped YCaBaCuO from femtosecond time-domain spectroscopy.*, Physical Review E **82**, 4918–4921 (1999).

[Dem11] J. Demsar and T. Dekorsy, *Carrier Dynamics in bulk semiconductors and metals after ultrashort pulse excitation*, Optical Techniques for Solid-State Materials Characterization, CRC Press, 2011.

[Den02] C. Deneke, C. Müller, N. Y. Jin-Phillipp, and O. G. Schmidt, *Diameter scalability of rolled-up In (Ga) As / GaAs nanotubes*, Semiconductor science and technology **17**, 1278–1281 (2002).

[Den04] C. Deneke, N.-Y. Jin-Phillipp, I. Loa, and O. G. Schmidt, *Radial superlattices and single nanoreactors*, Applied Physics Letters **84**, 4475 (2004).

[Den06] C. Deneke, U. Zschieschang, H. Klauk, and O. G. Schmidt, *InGaAs/GaAs/alkanethiolate radial superlattices*, Applied Physics Letters **89**, 263110 (2006).

[Den07] C. Deneke, W. Sigle, U. Eigenthaler, P. A. Van Aken, G. Schuetz, and O. G. Schmidt, *Interfaces in semiconductor/metal radial superlattices*, Applied Physics Letters **90**, 1–4 (2007).

[Den08] C. Deneke, J. Schumann, R. Engelhard, J. Thomas, W. Sigle, U. Zschieschang, H. Klauk, A. Chuvilin, and O. G. Schmidt, *Fabrication of radial superlattices based on different hybrid materials*, Physica Status Solidi (C) Current Topics in Solid State Physics **5**, 2704–2708 (2008).

[Den09] C. Deneke, R. Songmuang, N. Y. Jin-Phillipp, and O. G. Schmidt, *The structure of hybrid radial superlattices*, Journal of Physics D: Applied Physics **42**, 103001 (2009).

[Dev15] A. Devos, *Colored ultrafast acoustics: From fundamentals to applications*, Ultrasonics **56**, 90–97 (2015).

[Dra01] B. Drafts, *Acoustic Wave Technology Sensors*, IEEE Transactions on Microwave Theory and Techniques **49**, 795–802 (2001).

[Dw93] M. W. C. Dharma-wardana, P. X. Zhang, and D. J. Lockwood, *Finite-size effects on superlattice acoustic phonons*, Physical Review B **48**, 960–964 (1993).

[Elz87] P. A. Elzinga, R. J. Kneisler, F. E. Lytle, Y. Jiang, G. B. King, and N. M. Laurendeau, *Pump/probe method for fast analysis of visible spectral signatures utilizing asynchronous optical sampling.*, Applied optics **26**, 4303–9 (1987).

[Eva13] C. M. Evans, H. Deng, W. F. Jager, and J. M. Torkelson, *Fragility is a Key Parameter in Determining the Magnitude of*, Macromolecules **46**, 6091–6103 (2013).

[For98] J. A. Forrest, K. Dalnoki-Veress, and J. R. Dutcher, *Brillouin light scattering studies of the mechanical properties of thin freely standing polystyrene films*, Physical Review E **58**, 6109–6114 (1998).

[For01] J. A. Forrest and K. Dalnoki-Veress, *The glass transition in thin polymer films*, Advances in Colloid and Interface Science **94**, 167–196 (2001).

[Fri69] E. A. Friedman, A.J. Ritger, and R.D. Andrews, *Brillouin Scattering Near the Glass Transition of Polymethyl Methacrylate*, Journal of Applied Physics **40**, 4243 (1969).

[Fuj84] J. G. Fujimoto, J. M. Liu, E. P. Ippen, and N. Bloembergen, *Femtosecond Laser Interaction with Metallic Tungsten and Nonequilibrium Electron and Lattice Temperatures*, Physical Review Letters **53**, 1837–1840 (1984).

[Fur96] H. Furutani, H. Fukumura, and H. Masuhara, *Photothermal Transient Expansion and Contraction Dynamics of Polymer Films by Nanosecond Interferometry*, The Journal of Physical Chemistry **100**, 6871–6875 (1996).

[Füs12] H. Füser, S. Eichstädt, K. Baaske, C. Elster, K. Kuhlmann, R. Judaschke, K. Pierz, and M. Bieler, *Optoelectronic time-domain characterization of a 100 GHz sampling oscilloscope*, Measurement Science and Technology **23**, 025201 (2012).

[Gao13] L. Gao, F. Lemarchand, and M. Lequime, *Refractive index determination of SiO 2 layer in the UV / Vis / NIR range : spectrophotometric reverse engineering on single and bi-layer designs*, J. Europ. Opt. Soc. Rap. Public **8**, 13010 (2013).

[Geb10a] R. Gebs, *Asynchrones optisches Abtasten mit hoher Messgeschwindigkeit , Auflösung und Empfindlichkeit*, Dissertation, University of Konstanz, 2010.

[Geb10b] R. Gebs, G. Klatt, C. Janke, T. Dekorsy, and A. Bartels, *High-speed asynchronous optical sampling with sub-50fs time resolution*, Optics express **18**, 5974–5983 (2010).

[Gre70] B. N. Grechushnikov, O. V. Kachalov, N. M. Kreines, and M. A. Talalaev, *Mandel'shtam-brillouin scattering in calcite*, Soviet Physics JETP **30**, 850–852 (1970).

[Gri12] D. Grimm, C. C. Bof Bufon, C. Deneke, P. Atkinson, D. J. Thurmer, F. Schäffel, S. Gorantla, A. Bachmatiuk, and O. G. Schmidt, *Rolled-up nanomembranes as compact 3D architectures for field effect transistors and fluidic sensing applications.*, Nano letters **13**, 213–8 (2012).

[Gri14] D. Grimm, R. B. Wilson, B. Teshome, S. Gorantla, M. H. Rümmeli, T. Bublat, E. Zallo, G. Li, D. G. Cahill, and O. G. Schmidt, *Thermal conductivity of mechanically joined semiconducting/metal nanomembrane superlattices*, Nano Letters **14**, 2387–2393 (2014).

[Gro02] Y. Grohens, L. Hamon, G. Reiter, A. Soldera, and Y. Holl, *Some relevant parameters affecting the glass transition of supported ultra-thin polymer films*, European Physical Journal E **8**, 217–224 (2002).

[Gro13] M. Grossmann, M. Klingele, P. Scheel, O. Ristow, M. Hettich, C. He, R. Waitz, M. Schubert, A. Bruchhausen, V. Gusev, E. Scheer, and T. Dekorsy, *Femtosecond spectroscopy of acoustic frequency combs in the 100-GHz frequency range in Al/Si membranes*, Physical Review B **88**, 205202 (2013).

[Gro17a] M. Grossmann, *Characterization of interface adhesion and acoustic attenuation in multilayer systems*, Dissertation, University of Konstanz, 2017.

[Gro17b] M. Grossmann, M. Schubert, C. He, D. Brick, E. Scheer, M. Hettich, V. Gusev, and T. Dekorsy, *Characterization of thin-film adhesion and phonon-lifetimes in Al/Si membranes by picosecond ultrasonics*, New Journal of Physics **19**, 053019 (2017).

[GS16] D. Garcia-Sanchez, S. Deleglise, J. L. Thomas, P. Atkinson, C. Lagoin, and B. Perrin, *Acoustic confinement in superlattice cavities*, Physical Review A - Atomic, Molecular, and Optical Physics **94**, 1–6 (2016).

[Gus93] V. E. Gusev and A. A. Karabutov, *Laser Optoacoustics_Vitaly Gusev.pdf*, American Institute of Physics, 1993.

[Gus95] V. E. Gusev and O. B. Wright, *Acoustic generation in crystalline silicon with femtosecond optical pulses*, Appl. Phys. Lett **66**, 1190–1192 (1995).

[Har08] K. D. Harris, A. C. van Popta, J. C. Sit, D. J. Broer, and M. J. Brett, *A Birefringent and Transparent Electrical Conductor*, Advanced Functional Materials **18**, 2147–2153 (2008).

[Hec17] T. Hecksher, D. H. Torchinsky, C. Klieber, J. A. Johnson, J. C. Dyre, and K. A. Nelson, *Toward broadband mechanical spectroscopy*, PNAS **114**, 8710–8715 (2017).

[Hei17] D. Heinecke, *A 10 GHZ laser system for metrology and time-domain spectroscopy*, Dissertation, University of Konstanz, 2017.

[Het13] M. Hettich, *Investigation of Multilayer Systems by Coherent Acoustic Phonon Spectroscopy*, Dissertation, University of Konstanz, 2013.

[Het16] M. Hettich, K. Jacob, O. Ristow, M. Schubert, A. Bruchhausen, V. Gusev, and T. Dekorsy, *Viscoelastic properties and efficient acoustic damping in confined polymer nano-layers at GHz frequencies*, Scientific Reports **6**, 33471 (2016).

[Hud09] F. Hudert, *Asynchrones optisches Abtasten - eine neue Methode fuer die Pikosekunden-ultraschallspektroskopie*, Dissertation, University of Konstanz, 2009.

[Ins] Ioffe Institute, *http://www.ioffe.ru/SVA/NSM/Semicond/Si/mechanic.html.*

[Joh74] P. B. Johnson and R. W. Christy, *Optical constants of transition metals: Ti, V, Cr, Mn, Fe, Co, Ni, and Pd*, Physical Review B **9**, 5056–5070 (1974).

[Kan90] G. S. Kanner, Z. Vardeny, and B. C. Hess, *Picosecond acoustics in polythiophene thin films*, Physical Review B **42**, 5403–5406 (1990).

[Ked94] J. L. Keddie, R. A. L. Jones, and R. A. Cory, *Interface and Surface Effects on the Glass-transition Temperature in Thin Polymer Films*, Faraday Discussions **98**, 219–230 (1994).

[Kla09] G. Klatt, R. Gebs, C. Janke, T. Dekorsy, and A. Bartels, *Rapid-scanning terahertz precision spectrometer with more than 6 THz spectral coverage*, Optics Express **17**, 22847–22854 (2009).

[Kli15] C. Klieber, V. E. Gusev, T. Pezeril, and K. A. Nelson, *Nonlinear Acoustics at GHz Frequencies in a Viscoelastic Fragile Glass Former*, Physical Review Letters **114**, 065701 (2015).

[Kor08] C. V. Korff Schmising, A. Harpoeth, N. Zhavoronkov, Z. Ansari, C. Aku-Leh, M. Woerner, T. Elsaesser, M. Bargheer, M. Schmidbauer, I. Vrejoiu, D. Hesse, and M. Alexe, *Ultrafast magnetostriction and phonon-mediated stress in a photoexcited ferromagnet*, Physical Review B - Condensed Matter and Materials Physics **78**, 1–4 (2008).

[Kra06] B. Krause, C. Mocuta, T. Metzger, C. Deneke, and O. Schmidt, *Local Structure of a Rolled-Up Single Crystal: An X-Ray Microdiffraction Study of Individual Semiconductor Nanotubes*, Physical Review Letters **96**, 165502 (2006).

[Kro30] R. de L. Kronig and W.G. Penney, *Quantum Mechanics of Electrons in Crystak Lattices*, Proceedings of the Royal Society of London **A130**, 499 (1930).

[Kün01] N. Künzner, D. Kovalev, J. Diener, E. Gross, V. Yu. Timoshenko, G. Polisski, and F. Koch, *Giant birefringence in anisotropically nanostructured silicon*, Optics Letters **26**, 1265–1267 (2001).

[Lam16] C. S. Lam, *A Review of the Timing and Filtering Technologies in Smartphones*, IEEE International Frequency Control Symposium (New Orleans, USA), 2016.

[Lej16] M. Lejman, G. Vaudel, I. C. Infante, I. Chaban, T. Pezeril, M. Edely, G. F. Nataf, M. Guennou, J. Kreisel, V. E. Gusev, B. Dkhil, and P. Ruello, *Ultrafast acousto-optic mode conversion in optically birefringent ferroelectrics*, Nature Communications **7**, 12345 (2016).

[Li09] F. Li and Z. Mi, *Optically pumped rolled-up InGaAs/GaAs quantum dot microtube lasers.*, Optics express **17**, 19933–9 (2009).

[Löt97] J. C. Lötters, W. Olthuis, P. H. Veltink, and P. Bergveld, *The mechanical properties of the rubber elastic polymer polydimethylsiloxane for sensor applications*, Journal of Micromechanics and Microengineering **7**, 145–147 (1997).

[Ma15] W. Ma, T. Miao, X. Zhang, M. Kohno, and Y. Takata, *Comprehensive Study of Thermal Transport and Coherent Acoustic-Phonon Wave Propagation in Thin Metal Film–Substrate by Applying Picosecond Laser Pump–Probe Method*, The Journal of Physical Chemistry C **119**, 5152–5159 (2015).

[Mal65] I. H. Malitson, *Interspecimen Comparison of the Refractive Index of Fused Silica*,†*, Journal of the Optical Society of America **55**, 1205 (1965).

[Man08] P. A. Mante, J. F. Robillard, and A. Devos, *Complete thin film mechanical characterization using picosecond ultrasonics and nanostructured transducers: Experimental demonstration on SiO2*, Applied Physics Letters **93**, 1–4 (2008).

[Mat02] O. Matsuda and O. B. Wright, *Reflection and transmission of light in multilayers perturbed by picosecond strain pulse propagation*, Journal of the Optical Society of America B **19**, 3028 (2002).

[Moa13] B. Moazzez, S. M. O'Brien, and E. F. Merschrod, *Improved Adhesion of Gold Thin Films Evaporated on Polymer Resin: Applications for Sensing Surfaces and MEMS*, Sensors **13**, 7021–7032 (2013).

[Mor96] C. J. Morath, G. Tas, T. C. D. Zhu, and H. J. Maris, *Phonon attenuation in glasses studied by picosecond ultrasonics*, Physica B: Condensed Matter **219-220**, 296–298 (1996).

[Mou07] D. Mounier, E. Morosov, P. Ruello, M. Edely, P. Babilotte, C. Mechri, J.-M. Breteau, and V. Gusev, *Application of transient femtosecond polarimetry / ellipsometry technique in picosecond laser ultrasonics*, Journal of Physics: Conference Series **92**, 012179 (2007).

[Mou08] D. Mounier, E. Morozov, P. Ruello, J. Breteau, P. Picart, and V. Gusev, *Detection of shear picosecond acoustic pulses by transient femtosecond polarimetry*, The European Physical Journal Special Topics **153**, 243–246 (2008).

[Mus06] O. L. Muskens, M. T. Borgström, E. P. A. M. Bakkers, and J. G. Rivas, *Giant optical birefringence in ensembles of semiconductor nanowires*, Applied Physics Letters **89**, 233117 (2006).

[Mus13] W. A. Musa, T. K. Hamad, and M. T. A. Nabi, *Thickness Effect on the Optical Constants of Poly Methyl Methacrylate (PMMA) Doped by Potassium Iodide*, Journal of Al-Nahrain University **16**, 119–123 (2013).

[Nag95] H. Nagata, H. Takahashi, H. Takai, and T. Kougo, *Impurity Evaluations of SiO2 Films Formed on LiNbO3 Substrates*, Japanese Journal of Applied Physics **34**, 606–609 (1995).

[Nap13] S. Napolitano, S. Capponi, and B. Vanroy, *Glassy dynamics of soft matter under 1D confinement: How irreversible adsorption affects molecular packing, mobility gradients and orientational polarization in thin films*, European Physical Journal E **36**, 1–37 (2013).

[Naz05] E. Nazaretski, R. D. Merithew, R. O. Pohl, and J. M. Parpia, *Measurement of the acoustic properties of amorphous silica above 4.5 mK*, Physical Review B **71**, 144201 (2005).

[Par12] J. S. Park, W. J. Maeng, H. S. Kim, and J. S. Park, *Review of recent developments in amorphous oxide semiconductor thin-film transistor devices*, Thin Solid Films **520**, 1679–1693 (2012).

[Pel16] S. Peli, E. Cavaliere, G. Benetti, M. Gandol, M. Chiodi, C. Cancellieri, C. Giannetti, G. Ferrini, L. Gavioli, and F. Ban, *Mechanical Properties of Ag Nanoparticle Thin Films Synthesized by Supersonic Cluster Beam Deposition*, The Journal of Physical Chemistry C **120**, 4673–4681 (2016).

[Pen11] T. Pensala, *Thin Film Bulk Acoustic Wave Devices*, Dissertation, Aalto University, 2011.

[Pez06] T. Pezeril, N. Chigarev, P. Ruello, S. Gougeon, D. Mounier, J. Breteau, P. Picart, and V. Gusev, *Laser acoustics with picosecond collimated shear strain beams in single crystals and polycrystalline materials*, Physical Review B **73**, 132301 (2006).

[Pra12] R. P. Prasankumar and A. J. Taylor (eds.), *Optical Techniques for Solid-State Materials Characterization*, CRC Press, 2012.

[Pri00] V. Ya. Prinz, V. A. Seleznev, A. K. Gutakovsky, A. V. Chehovskiy, V. V. Preobrazhenskii, M. A. Putyato, and T. A. Gavrilova, *Free-standing and overgrown InGaAs/GaAs nanotubes, nanohelices and their arrays*, Physica E: Low-dimensional Systems and Nanostructures **6**, 828–831 (2000).

[PW12] M. F. Pascual-Winter, A. Fainstein, B. Jusserand, B. Perrin, and A. Lemaître, *Spectral responses of phonon optical generation and detection in superlattices*, Physical Review B **85**, 235443 (2012).

[Rae10] A. Raegen, M. Chowdhury, C. Calers, A. Schmatulla, U. Steiner, and G. Reiter, *Aging of thin polymer films cast from a near-theta solvent*, Physical Review Letters **105**, 5–8 (2010).

[Rau08] S. Rausch, T. Binhammer, A. Harth, J. Kim, R. Ell, F. Kärtner, and U. Morgner, *Controlled waveforms on the single-cycle scale from a femtosecond oscillator*, Optics Express **16**, 9739 (2008).

[Rau11] H. K. Raut, V. A. Ganesh, A. S. Nair, and S. Ramakrishna, *Anti-reflective coatings: A critical, in-depth review*, Energy & Environmental Science **4**, 3779 (2011).

[RE08] J. A. Reyes-Esqueda, C. Torres-Torres, J. C. Cheang-Wong, A. Crespo-Sosa, L. Rodríguez-Fernández, C. Noguez, and A. Oliver, *Large optical birefringence by anisotropic silver nanocomposites*, Optics express **16**, 710–717 (2008).

[Ris16] O. Ristow, *High-Frequency Acoustic Phonons in Confined Geometries*, Dissertation, University of Konstanz, 2016.

[Rod12] R. D. Rodriguez, E. Sheremet, D. J. Thurmer, D. Lehmann, O. D. Gordan, F. Seidel, A. Milekhin, O. G. Schmidt, M. Hietschold, and D. R. Zahn, *Temperature-dependent Raman investigation of rolled up InGaAs/GaAs microtubes.*, Nanoscale research letters **7**, 594 (2012).

[Rog10] J. A. Rogers, T. Someya, and Y. Huang, *Materials and Mechanics for Stretchable Electronics*, Science **327**, 1603–1607 (2010).

[Ros99] J. L. Rose, *Ultrasonic Waves in Solid Media*, Cambridge University Press, 1999.

[Ros08] C. Rossignol, N. Chigarev, M. Ducousso, B. Audoin, G. Forget, F. Guillemot, M. C. Durrieu, C. Rossignol, N. Chigarev, M. Ducousso, B. Audoin, G. Forget, and F. Guillemot, *In Vitro picosecond ultrasonics in a single cell In Vitro picosecond ultrasonics in a single cell*, Applied Physics Letters **93**, 123901 (2008).

[Rue15] P. Ruello and V. E. Gusev, *Physical mechanisms of coherent acoustic phonons generation by ultrafast laser action*, Ultrasonics **56**, 21–35 (2015).

[Ruf98] T. Ruf, *Phonon Raman Scattering in Semiconductors, Quantum Wells and Superlattices*, Springer Tracts in Modern Physics, 1998.

[Rup02] C. C. W. Ruppel, L. Reindl, and R. Weigel, *SAW Devices and their Wireless Communication Applications*, IEEE microwave magazine **3**, 65–71 (2002).

[Ryt56] S. M. Rytov, *No Title*, Akust. Zh. **2**, 71 (1956).

[Sai03] T. Saito, O. Matsuda, and O. B. Wright, *Picosecond acoustic phonon pulse generation in nickel and chromium*, Physical Review B **67**, 205421 (2003).

[Sal07] B. E. A. Saleh and M. C. Teich, *Fundamentals of Photonics*, Wiley, 2007.

[San10] S. Sanna and W. G. Schmidt, *Lithium niobate X -cut, y -cut, and Z -cut surfaces from ab initio theory*, Physical Review B - Condensed Matter and Materials Physics **81**, 1–11 (2010).

[Sav10] N. Savage, *Acousto-optic devices*, product focus **4**, 2010 (2010).

[Sch01a] O. G. Schmidt and K. Eberl, *Thin solid films roll up into nanotubes*, Nature **410**, 2001 (2001).

[Sch01b] O. G. Schmidt, N. Schmarje, C. Deneke, C. Muandller, and N. Y. Jin-Phillipp, *Three-dimensional Nano-objects Evolving from a Two-Dimensional Layer Technology*, Advanced Materials **13**, 756–759 (2001).

[Sch12] S. Schwaiger, A. Rottler, and S. Mendach, *Rolled-up metamaterials*, Advances in OptoElectronics **2012**, 1–10 (2012).

[Sch14] M. Schubert, M. Grossmann, C. He, D. Brick, P. Scheel, O. Ristow, V. Gusev, and T. Dekorsy, *Generation and detection of gigahertz acoustic oscillations in thin membranes*, Ultrasonics **56**, 109–115 (2014).

[Set06] N. Setter, D. Damjanovic, L. Eng, G. Fox, S. Gevorgian, S. Hong, A. Kingon, H. Kohlstedt, N. Y. Park, G. B. Stephenson, I. Stolitchnov, A. K. Taganstev, D. V. Taylor, T. Yamada, and S. Streiffer, *Ferroelectric thin films: Review of materials, properties, and applications*, Journal of Applied Physics **100**, 051606 (2006).

[Son06] R. Songmuang, N. Y. Jin-Phillipp, S. Mendach, and O. G. Schmidt, *Single rolled-up SiGe/Si microtubes: Structure and thermal stability*, Applied Physics Letters **88**, 021913 (2006).

[Son07] R. Songmuang, A. Rastelli, S. Mendach, and O. G. Schmidt, *SiOx/Si radial superlattices and microtube optical ring resonators*, Applied Physics Letters **90**, 7–9 (2007).

[Spe91] D. E. Spence, P. N. Kean, and W. Sibbett, *60-fsec pulse generation from a self-mode-locked Ti:sapphire laser*, Optics Letters **16**, 42–44 (1991).

[Tad09] S. Tadigadapa and K. Mateti, *Piezoelectric MEMS sensors: state-of-the-art and perspectives*, Measurement Science and Technology **20**, 092001 (2009).

[Tam88] S. Tamura, D. C. Hurley, and J. P. Wolfe, *Acoustic-phonon propagation in superlattices*, Physical Review B **38**, 1427 (1988).

[Tas92] G Tas, R J Stoner, H J Maris, G W Rubloff, G S Oehrlein, and J M Halbout, *Noninvasive picosecond ultrasonic detection of ultrathin interfacial layers : CFx at the*

Al / Si interface Noninvasive picosecond ultrasonic CFx at the AVSi interface detection of ultrathin interfacial layers :, Applied Physics Letters **61**, 1787 (1992).

[Tas94] G. Tas and H. J. Maris, *Electron diffusion in metals studied by picosecond ultrasonics*, Physical Review B **49**, 15046–15054 (1994).

[Tas98] G. Tas, J. J. Loomis, H. J. Maris, A. A. Bailes, and L. E. Seiberling, *Picosecond ultrasonics study of the modification of interfacial bonding by ion implantation*, Applied Physics Letters **72**, 2235 (1998).

[Tho84] C. Thomsen, J. Strait, Z. Vardeny, H. J. Maris, J. Tauc, and J. J. Hauser, *Coherent phonon generation and detection by picosecond light pulses*, Physical Review Letters **53**, 989–992 (1984).

[Tho86] C. Thomsen, H. T. Grahn, H. J. Maris, and J. Tauc, *Surface generation and detection of photons by picosecond light pulses*, Physical Review **34**, 4129–4138 (1986).

[Tho87] C. Thomsen, H. J. Maris, and J. Tauc, *Picosecond Acoustics as a Non-Destructive Tool for the Characterization of Very Thin Films*, Thin Solid Films **154**, 217–223 (1987).

[Tri02a] M. Trigo, A. Bruchhausen, A. Fainstein, B. Jusserand, and V. Thierry-Mieg, *Confinement of Acoustical Vibrations in a Semiconductor Planar Phonon Cavity*, Physical Review Letters **89**, 227402 (2002).

[Tri02b] M. Trigo, A. Fainstein, B. Jusserand, and V. Thierry-Mieg, *Finite-size effects on acoustic phonons in GaAs/AlAs superlattices*, Physical Review B **66**, 1–7 (2002).

[Tse06] K. T. Tsen, *Non-equilibrium dynamics of semiconductors and nanostructures*, Taylor&Francis, 2006.

[Val07] F. Vallée, *Energy Exchange at Short Time Scales: Electron-Phonon Interactions in Metals and Metallic Nanostructures*, Microscale and Nanoscale Heat Transfer, Springer-Verlag, Berlin Heidelberg, 2007, pp. 309–332.

[Vol16] S. Volz, J. Ordonez-Miranda, A. Shchepetov, M. Prunnila, J. Ahopelto, T. Pezeril, G. Vaudel, V. Gusev, P. Ruello, E. M. Weig, M. Schubert, M. Hettich, M. Grossman, T. Dekorsy, F. Alzina, B. Graczykowski, E. Chavez-Angel, J. Sebastian Reparaz, M. R. Wagner, C. M. Sotomayor-Torres, S. Xiong, S. Neogi, and D. Donadio, *Nanophononics: state of the art and perspectives*, The European Physical Journal B **89**, 15 (2016).

[Web00] M. F. Weber, C. A. Stover, L. R. Gilbert, T. J. Nevitt, and A. J. Ouderkirk, *Giant Birefringent Optics in Multilayer Polymer Mirrors*, Science **287**, 2451–2457 (2000).

[Wri92] O. B. Wright, *Thickness and sound velocity measurement in thin transparent films with laser picosecond acoustics*, Journal of Applied Physics **71**, 1617–1629 (1992).

[Wri01] O. B. Wright, B. Perrin, O. Matsuda, and V. E. Gusev, *Ultrafast carrier diffusion in gallium arsenide probed with picosecond acoustic pulses*, Phys. Rev. B **64**, 81202 (2001).

[Wu96] X. L. Wu, G. G. Siu, M.. J Stokes, S. Tong, F. Yan, X. N. Liu, X. M. Bao, S. S. Jiang, X. K. Zhang, and D. Feng, *Observation of folded acoustic phonons in nanocrystalline silicon / amorphous silicon multilayers*, Applied Physics Letters **69**, 1855–1857 (1996).

[Wu07] S. Wu, P. Geiser, J. Jun, J. Karpinski, and R. Sobolewski, *All-optical generation and detection of coherent acoustic phonons in GaN single crystals*, Conference on Lasers and Electro-Optics, 2007, CLEO 2007, 1–8 (2007).

[Xi14] W. Xi, C. K. Schmidt, S. Sanchez, D. H. Gracias, R. E. Carazo-Salas, S. P. Jackson, and O. G. Schmidt, *Rolled-up functionalized nanomembranes as three-dimensional cavities for single cell studies*, Nano Letters **14**, 4197–4204 (2014).

[Xia04] H. Xia, X. Zeng, J. Wang, J. Zhang, J. Xu, Y. Zhang, and Q. Nie, *Optical absorption spectra of LiNbO3, Fe : LiNbO3, and Zn:Fe:LiNbO3 single crystals grown by Bridgman method*, Cryst. Res. Technol. **39**, 337–342 (2004).

[Zan09] T. Zander, C. Deneke, A. Malachias, C. Mickel, T. H. Metzger, and O. G. Schmidt, *Planar hybrid superlattices by compression of rolled-up nanomembranes*, Applied Physics Letters **94**, 2007–2010 (2009).

List of Publications

Within the framework of this doctoral research study there were contributions to the following publications and international conferences:

Publications in refereed Journals

8. D. Brick, E. Emre, M. Grossmann, M. Hettich, and T. Dekorsy "*Picosecond Photoacoustic Metrology of* SiO_2 *and* $LiNbO_3$ *Layer Systems used for High Frequency Filters in Mobile Phones*", Applied Sciences 7, 1-7 (2017).

7. D. Brick, Y. Guo, M. Grossmann, V. Engemaier, G. Li, D. Grimm, O. G. Schmidt, M. Schubert, V. E. Gusev, M. Hettich, and T. Dekorsy "*Interface Adhesion and Structural Characterization of Rolled-up* $GaAs/In_{0.2}Ga_{0.8}As$ *Multilayer Tubes by Coherent Phonon Spectroscopy*", Scientific Reports 7, 1-8 (2017).

6. C. He, O. Ristow, M. Grossmann, D. Brick, Y. Guo, M. Schubert, M. Hettich, V. Gusev, and T. Dekorsy "*Acoustic waves undetectable by transient reflectivity measurements*", Phys. Rev. B 95, 184302 (2017).

5. M. Grossmann, M. Schubert, C. He, D. Brick, E. Scheer, M. Hettich, V. Gusev, and T. Dekorsy "*Characterization of thin-film adhesion and phonon-lifetimes in Al/Si membranes by picosecond ultrasonics.*", New Journal of Physics (2017).

4. Y. Guo, D. Brick, M. Grossmann, M. Hettich, and T. Dekorsy, "*Acoustic beam splitting at low GHz frequencies in a defect-free phononic crystal*", Appl. Phys. Lett. 110, 031904 (2017).

3. C. He, M. Grossmann, D. Brick, M. Schubert, S. V. Novikov, C. T. Foxon, V. Gusev, A. J. Kent, and T. Dekorsy "*Study of confined coherent acoustic phonon modes in a free-standing cubic GaN membrane by femtosecond spectroscopy*", Appl. Phys. Lett. 107, 112105 (2015).

2. C. He, M. Daniel, M. Grossmann, O. Ristow, D. Brick, M. Schubert, M. Albrecht, and T. Dekorsy "*Dynamics of coherent acoustic phonons in thin films of CoSb3 and partially filled YbxCo4Sb12 skutterudites*", Phys. Rev. B 89, 174303 (2014).

1. M. Schubert, M. Grossmann, C. He, D. Brick, P. Scheel, O. Ristow, V. Gusev, and T. Dekorsy, "*Generation and detection of gigahertz acoustic oscillations in thin membranes*", Ultrasonics 56, 109-115 (2014).

Presentations on international conferences

6. (POSTER) D. Brick, V. Engemaier, Y. Guo, M. Grossmann, G. Li, D. Grimm, O.G. Schmidt, M. Schubert, V. Gusev, M. Hettich, and T. Dekorsy: "*Structural Characterization of Rolled-up GaAs/$In_{0.2}Ga_{0.8}As$ Multilayer Tubes by Coherent Phonon Spectroscopy*", SAWtrain Summer School "Physics and applications of GHz vibrations in semiconductors", Cargese, Corsica, France (11.-21. July 2017).

5. (POSTER) D. Brick, V. Engemaier, Y. Guo, M. Grossmann, G. Li, D. Grimm, O.G. Schmidt, M. Schubert, V. Gusev, M. Hettich, and T. Dekorsy: "*Structural Characterization of Rolled-up GaAs/$In_{0.2}Ga_{0.8}As$ Multilayer Tubes by Coherent Phonon Spectroscopy*", Trends in Nanoscience 2017, Kloster Irsee, Germany (27.-30. March 2017).

4. D. Brick, Y. Guo, M. Grossmann, V. Meier, G. Li, Y. Huo, D. Grimm, O. G. Schmidt, M. Hettich, and T. Dekorsy: "*Coherent Acoustic Phonons in Rolled-up GaAs/InGaAs Tubes: Transition from a Bilayer to a Superlattice*", 19th International Conference on Superlattices, Nanostructures and Nanodevices (ICSNN 2016), Hongkong, (25.-30. July 2016).

3. (POSTER) D. Brick, M. Schubert, M. Grossmann, C. He, V. Engemaier, G. Li, Y. Huo, D. Grimm, O. G. Schmidt, and T. Dekorsy "*Generation and Analysis of Coherent Acoustic Phonons in Rolled-up GaAs/InGaAs Superlattices*", Phonons, Nottingham, England (12.-17. July 2015).

2. (POSTER) D. Brick, M. Schubert, M. Grossmann, C. He, V. Meier, G. Li, Y. Huo, D. Grimm, O.G. Schmidt, and T. Dekorsy: "*Investigation of Acoustic Phonons in Rolled-up GaAs/InGaAs Superlattices*", Winter School "Son et lumiere 2015", Les Houches, France (16.-27. February 2015).

1. D. Brick, C. He, M. Grossmann, V. Meier, G. Li, Y. Huo, D. Grimm, O. G. Schmidt, M. Schubert, and T. Dekorsy: "*Asynchronous Optical Sampling of Rolled-up GaAs/InGaAs Superlattices*", DPG Fruehjahrstagung, Berlin, Germany (15.-20. March 2015).

Acknowledgement

Finally the dissertation is completed. Therefore I would like to take the opportunity to express my gratitude to several people who supported me in different ways along this challenging and sometimes frustrating road. I want to thank

First of all my advisor **Prof. Dr. Thomas Dekorsy** for giving me the opportunity to do research in his group, enabling several trips to interesting conferences, for the discussions and support,

Dr. Martin Schubert and **Dr. Mike Hettich**, for their help as postdocs in discussing results, evaluation of data and paper drafts and any problems concerning the research and **Prof. Dr. Vitali Gusev** for support with the theory,

Dr. Martin Großmann for all the funny moments, hours of talking, discussing, dancing, and the friendship in general,

Everyone that proofread smaller or larger parts of my thesis, especially **Dr. Nicki Tyler** and **Steph Haas**,

All my friends in Konstanz that made my time here special, in particular **Steffi Klima**, **Tobi Rybka**, **Michi Jawurek**, **Erkan Emre**, **Dr. Bernhard Mayer**, **Dr. Joni Fischer**, **Dr. Martin Stärk** and **Anja Beuter**,

All other members from (the former) **AG Dekorsy**, **Marcel Hofstetter** for the help with the measurements, and many members of other physics groups of the University of Konstanz for their companionship,

Matthias Hagner for support in the Nanolab and **Letizia Bruscaglioni** for the help with any administrative questions,

And last but not least **my family** for their understanding, moral support and love in times when the path towards obtaining the Ph.D. was exhausting and stressful,

Thanks for all the encouragement.